TECHNISCHE UNIVERSITÄT MÜNCHEN
Walter Schottky Institut
Lehrstuhl für Halbleitertechnologie

Electrically-Pumped GaSb-Based Vertical-Cavity Surface-Emitting Lasers

Shamsul Arafin

Vollständiger Abdruck der von der Fakultät für
Elektrotechnik und Informationstechnik der Technischen Universität München
zur Erlangung des akademischen Grades eines

Doktor-Ingenieurs (Dr.-Ing.)

genehmigten Dissertation.

Vorsitzender:	Univ.-Prof. Dr.-Ing. Dr. h.c. Alexander W. Koch
Prüfer der Dissertation:	1. Univ.-Prof. Dr.-Ing. Markus-Christian Amann
	2. Univ.-Prof. Dr. rer. nat. Franz Kreupl

Die Dissertation wurde am 20.10.2011 bei der Technischen Universität München
eingereicht und durch die Fakultät für Elektrotechnik und Informationstechnik
am 13.01.2012 angenommen.

Summary

Electrically-pumped (EP) vertical-cavity surface-emitting lasers (VCSELs) operating above 2 µm are currently attracting considerable attention for potential gas sensing applications by tunable diode laser absorption spectroscopy (TDLAS). There are strong absorption lines of numerous polluting gases in the wavelength range between 2.3 and 3.5 µm. Due to material limitations, InP-based devices will probably not reach more than 2.3 µm. In contrast, the GaSb-based material system allows covering the whole mid-infrared wavelength regime. As light sources, VCSELs are very attractive choices for these applications because VCSELs exhibit excellent lasing characteristics, such as true single-mode operation, high current tuning coefficient and cost-effective production.

This thesis focuses on the development of novel electrically-pumped (EP) continuous-wave (CW) operating GaSb-based application-suited VCSELs in the wavelength range between 2.3 µm and 2.6 µm. In particular, much emphasis has been laid on devices with record long emission wavelengths of 2.6 µm which exhibit single-mode operation with a reasonably wide mod-hop free tuning range. The design, fabrication and especially the characterization of such lasers are extensively discussed here. This thesis also presents some design principles for next generation high performance GaSb-VCSELs based on the device characterization results. The examination of the several individual components of the device and their successful implementation onto the device are also covered here.

The presented devices are operated upside-up in a top-emitting configuration with a bottom epitaxial and top outcoupling dielectric Bragg mirror. Lateral current confinement and index guiding in the device are accomplished by utilizing the buried tunnel junction (BTJ) concept. In addition, the BTJ concept allows the substitution of the p-type layers by n-type ones on top of the BTJ to obtain a low electrical resistance, and as a consequence, a reduced device heating which is one of the biggest concerns in very long wavelength VCSELs utilizing low bandgap materials.

Low resistive ohmic contacts to lattice-matched n-type InAsSb on n-GaSb substrates for such devices is extremely important. Using wet chemical treatment as a surface preparation in order to remove the native oxides and evaporating Ti/Pt/Au metals sequentially, specific contact resistivities as low as $5.6 \times 10^{-6}\,\Omega\,\mathrm{cm}^2$ without any annealing are obtained. The resistivity decreases to $3.7 \times 10^{-6}\,\Omega\,\mathrm{cm}^2$ after annealing at 350°C for 90 s. An n^+-InAsSb / p^+-GaSb tunnel junction for intra-device contacts with an extremely low contact-resistivity of $1.5 \times 10^{-6}\,\Omega\,\mathrm{cm}^2$ is also reported.

During the project work, worldwide first results on EP, continuous-wave operating single-mode GaSb-based VCSELs with a long emission wavelength of 2.5 µm were achieved. The device performance was enhanced in 2.6 µm VCSELs in terms of output power and maximum operating temperature. Owing to the excellent thermal heat management, these devices operate up to a heatsink temperature of 58°C with reasonable optical output power.

Devices exhibit single-mode emission over their entire operating range along with a reasonably good tuning behavior. The VCSEL emission wavelength has been extended up to 2.63 µm where single-mode operation is achieved from devices up to 9 µm aperture diameter. This is advantageous for many spectroscopic applications since higher optical output power can be obtained from large aperture devices, while maintaining single-mode operation. Finally the suitability and applicability of these presented lasers as a light source in photonic sensors has been confirmed by performing a TDLAS-based water vapor measurement.

For improved device performance in terms of better thermal management, the new concept, i.e. mounting VCSEL chip upside-down on integrated gold heatsink is introduced. A dielectric Bragg mirror on both sides of the cavity can be employed in such device structure. Thus the optical absorption loss and at the same time electrical series resistance in the device can be minimized by using lossless dielectric mirror instead of lossy n-doped epitaxial mirror. All the optimized technological processes required for the device fabrication by using such concept are also illustrated here.

The presented work on mid-infrared VCSELs would greatly expand the scope of spectroscopic applications like gas sensing by realizing compact, low-cost photonic sensors. The wavelength range from 2.5 µm to 2.63 µm accessed in this study is extremely important due to the presence of strong water vapor (H_2O), hydrogen-sulfide (H_2S), hydrogen-cyanide (HCN) and nitrous oxide (N_2O) absorption lines, enabling a sensor to detect these gases at a much higher sensitivity. In fact, emission wavelengths of these lasers are obtained at 2.605, 2.596 and 2.594 µm where the strongest water vapor absorption lines lie. Such application-suited VCSELs open the way especially for water measurements and isotopic ratio studies by realizing absorption spectrometers with significant sensitivity improvements.

Contents

Introduction

Recently, there has been an increasing interest in mid-infrared (MIR) diode lasers due to a wide range of emerging applications. For instance, these lasers are used in countermeasures against heat-seeking missiles in the military field [1], thermal imaging systems [2] chemical process monitoring [3], industrial process controlling [4], non-invasive medical diagnostics [2, 5] and free-space optical communication [6]. Some other potential applications newly served by these lasers are protein folding dynamic studies and facilitation of drug development, stand-off explosive detection, time-resolved IR spectroscopy, sub-diffraction-limited hyperspectral imaging (scanning near-field optical microscopy), and the detection of low-volume or transient analytes [7]. So, it is obvious that currently, the landscape of the mid-infrared (MIR) laser market has expanded tremendously in terms of commercial applicability, widespread adoption and extreme growth in overall market value.

In addition, in recent years, trace-gas sensing by tunable diode laser absorption spectroscopy (TDLAS) has also drawn lots of attention for security and environmental reasons [8]. Compared to conventionally used electro-chemical cells, TDLAS-based photonic sensors offers certain advantages for the study of absorption spectra of gaseous molecules by significantly increasing the gas detection sensitivity and selectivity [9] and by lowering the response time. Such photonic sensors can be additionally benefited in terms of the sensitivity when the absorption lines of these trace gases become strong. As a matter of fact, strong absorption lines of numerous trace gases like CO, H_2S, H_2O, HF, CH_4, CO_2 etc. lie in the spectral regime of 2 to 3.5 µm [10]. This is why currently significant progress has been made towards the development of MIR lasers especially in the aforementioned wavelength regime.

Several groups worldwide are currently actively involved in pursuing antimonide-based lasers between 2 and 3.5 µm. Unfortunately, TDLAS suitable InP-based lasers can access up to the wavelength of 2.3 µm which seems to be the wavelength limit for the InP material system [11]. Wavelengths higher than 2.3 µm are only accessible with the GaSb material system. This necessitates the novel (AlGaIn)(AsSb) material-system on GaSb substrates to realize application-suited light sources in the desired wavelength regime.

Principally suited light sources are edge-emitters, distributed feedback (DFB) lasers and vertical-cavity surface-emitting lasers (VCSELs). Spectroscopic experiments cannot be successfully performed using conventional edge-emitters due to their multimode behavior as well as mode-hopping which degrade the performance of the sensors. Despite of the single-longitudinal and transverse mode emission, DFB lasers suffer from their high manufacturing cost and low (electro-)thermal wavelength tunability. However, light sources with a single longitudinal and transverse mode emission, high (electro-)thermal wavelength tunability as well as a wide mode-hop free tuning range is desired in compact and low-cost TDLAS-based photonic sensors [12]. Since VCSELs fulfill all these requirements at a time, they can be considered as ideal laser sources for this gas sensing application.

Significant efforts have already been devoted to develop optically-pumped GaSb-based VCSELs as a first step into the MIR wavelength regime. However, optical pumping significantly increases the complexity and the cost of the overall system due to the use of an additional pump laser which itself requires much more electrical power. The realization of a compact and packaged sensing system seems to be difficult in this way. Such a circumstance necessitates the realization of electrically-pumped (EP) VCSELs preferably operating in the continuous-wave (CW) mode and at room temperature (RT).

The principal aim of this thesis is to realize electrically-pumped GaSb-based CW-operating VCSELs with an emission wavelength of above 2 µm. Utilizing buried tunnel junction (BTJ) concept, current and optical confinement is introduced in these devices. This work was performed together with Kaveh-Kashani Shirazi and Kristijonas Vizbaras who were involved in the epitaxial growth of antimonide semiconductor layers and VCSEL structures using molecular beam epitaxy (MBE). The primary focus of this dissertation has been the development of EP GaSb-based BTJ VCSELs emitting at a record long wavelength of 2.6 µm. This thesis extensively examines the design, fabrication, and characterization of such devices which exhibit single-mode emission with a wide mode-hop free tuning range, being suitable for gas sensing applications. As a part of the continuation of this work, a significant effort has been put into extending the VCSEL emission wavelength further, especially beyond 3 µm. Results and analysis of devices designed for this very long wavelength will be presented in this thesis as well.

This thesis is organized as follows:

- **Chapter 1** introduces the challenges and critical issues for the research and development in GaSb-based VCSELs. The progress on mid-infrared VCSELs research worldwide will also be described briefly.

- **Chapter 2** describes the theory and fundamentals of VCSELs.

- **Chapter 3** presents the GaSb-based VCSEL issues relating to optical, electrical and thermal design. The discussion starts by describing the active region design, cavity design and top and bottom Bragg mirror design. The electrical and optical characteristics of BTJ in devices under study is also described in detail. In addition, the electrical design and optimization of several device components is explained.

- **Chapter 4** discusses the fabrication process of top-emitting GaSb-based VCSELs. The special attention is paid to the fabrication process involved in VCSELs with upside-down concept.

- **Chapter 5** reports the analysis of VCSEL materials using several characterization procedures on the way towards the realization of GaSb-based BTJ VCSELs.

- **Chapter 6** illustrates results and the corresponding discussion of EP VCSELs at 2.6 µm. CW light output-current-voltage *(L-I-V)* and light-current relationships vs. temperature *(L-I-T)* for these devices are presented in addition to threshold and thermal analysis. This chapter examines the analysis and performance of non-working devices designed for VCSELs with an emission wavelength of 3.4 µm.

- **Chapter 7** is devoted to a discussion for several suggestions of future work that may improve the device performance. Also the future directions of this research along with device improvements expected to make further progress in GaSb-based VCSELs are discussed here.

1 Challenges and Development of GaSb-VCSELs

This chapter will describe the challenges or difficulties associated with producing high-performance Sb-based lasers, in particular, VCSELs. This will be followed by the discussion of dramatic recent technical progress of mid-IR VCSELs/V(External)CSELs emitting at wavelengths above 2 µm after the challenges have been overcome to a large extent. Also a short description on TDLAS-based gas detection principles will be provided in the last section.

1.1 Critical Issues

Ongoing research efforts to realize semiconductor lasers in the wavelength range above 2 µm have become a great concern at present. The principal goal is to achieve room temperature, CW operating single-mode semiconductor lasers. The realization of application-suited VCSELs in this wavelength regime utilizing antimonide material system could be one of the most sophisticated ways towards fulfilling the goal. However, one approaches several obstacles and difficulties in performing this task which are addressed below:

- Availability of high quality and low-cost native substrates is one of the most important requirements to bring significant improvements in the ongoing research of antimonide devices. But GaSb-substrate is still much more expensive than native substrates used in the matured wavelength range (850 nm $\leq \lambda \leq$ 2 µm), e.g. GaAs and InP which makes the research on GaSb-based devices very expensive.

- Many GaSb devices would greatly benefit from the availability of a semi-insulating substrate. For instance, in order to have an accurate knowledge on the doping concentration and mobility data of GaSb-based epilayers by Hall measurement, semi-insulating substrate is required. Due to lack of this type of substrate, such characterization of epilayers cannot be performed which influences in the VCSEL design as well as its performance analysis. One could think of growing GaSb-based epilayers on semi-insulating GaAs substrate to know these material data. However, the lattice mismatch (8%) and chemical incompatibility between GaSb and GaAs could influence the mobility and carrier concentration.

- Epi-ready GaSb substrates are highly desirable for growth. But native oxides on epi-ready GaSb substrates becomes a threat for the epitaxial growth of high quality. Recent studies using *in-situ* reflectance and *ex-situ* atomic force microscopy (AFM), combined with analysis of the chemistry and kinetics of native oxides in GaSb, have shown that thermal desorption of native oxides can lead to surface roughening [13]. This necessitates a surface treatment for substrates prior to growth.

- MBE growth of antimonides is more challenging than arsenides due to the fact that most epilayers involves mixed group V elements, i.e. As and Sb need to be used at the same time, e.g. InAsSb, AlAsSb, GaInAsSb which results in a non-reproducible

growth [14]. In other words, a small change in the group V flux ratios can lead to a large change in composition in the growing layers. Therefore, a time consuming and complex calibration for the group V incorporation factor has to be done in advance to get a stable and reproducible growth.

- One of the most crucial problems in GaSb material system is the presence of a large miscibility gap in the active region materials made of $Ga_{(1-x)}In_xAs_ySb_{(1-y)}$ alloys [15]. This becomes increasingly less stable as x approaches 0.5, limiting the variations in the compositions that can be realized.

- Unlike GaAs- and InP-based systems, very few reliable and secured material data of antimonide system is available in the literature. This really affects in designing complicated devices like VCSELs. For instance, wavelength dependent refractive index and absorption data are of great importance for a successful VCSEL device design which are still not well-known.

- Not only in epitaxial growth difficulties but also technological immaturity in antimonide material system have impeded to produce the significant improvement especially on the manufacturing process of devices. For instance, only few recipes of selective wet and dry chemical etching used in device processing are known.

- One of the primary challenges in antimonide laser development is the non-radiative Shockley-Read (SR) and Auger recombination mechanisms due to the involvement of materials with small bandgap, though S-R lifetimes in antimonide laser materials typically fall in the 1-200 ns range [16]. Experimental determinations of the Auger coefficient on bulk antimonides show that this increase is of exponential type with decreasing bandgap energy. Experimentally it has also been proven that the increase of the threshold current density with increasing emission wavelength in antimonide lasers can be attributed to the Auger recombination [17].

- In addition to non-radiative recombination processes mentioned above, a second fundamental issue limiting the antimonide laser performance is a rapid increase of the internal absorption loss. At present this probably represents the greatest obstacle to realize lasers operating in high temperature emitting beyond 3 µm [18]. In fact, most losses may be associated with free-carrier absorption (FCA) which is nothing but exciting an free electron in the conduction band or free holes in the valence band.

- Another limiting factor on the way towards the realization of high quality antimonide lasers is that the oxidation rate of GaSb is exponentially fast [19]. Precautions must be taken to limit the formation of the native oxides during the surface preparation, for instance, while forming a low resistive ohmic contact on this material system, it is very important to etch the oxides chemically at first and then the contact surface is treated so that negligible surface oxide subsequently forms prior to loading into the metalization chamber.

In spite of the numerous challenges discussed in the previous section, problems have been circumvented through extensive efforts and improvements in alternate possibilities. Finally, GaSb-based VCSELs have been successfully realized with a reasonable device performance.

1.2 Progress of GaSb-V(E)CSELs Research

An overview of the results for GaSb-based surface-emitting lasers using GaSb substrates already achieved by the scientific community is presented in Tab. 1.1. In most cases, optical pumping is adopted which significantly increases the complexity and the cost of the overall system due to the use of a pump laser as mentioned earlier.

Institute	Pump mechanisms	Laser type	Wavelength	Output power
Fraunhofer IAF, Freiburg	optically	external outcoupling mirror	1.9-2.8 µm	120 mW (CW at RT) @ 2.8 µm
Univ. Montpellier 2	optically	VCSEL with dielectric outcoupling mirror	2.0-2.7 µm (multimode)	35 mW (CW at 81 K)
Univ. Montpellier 2	electrically	VCSEL without current aperture	2.2-2.63 µm (multimode)	not known
Naval Research Lab and Hughes Research Lab	optically	VCSEL with dielectric DBR	2.9 µm	> 2 W (pulsed at 240 K)
Tech. Univ. München	electrically	VCSEL with current aperture	2.3-2.63 µm (single-mode)	< 0.8 mW (CW at RT)
Tampere Univ. Tech. and Tech. Univ. München	electrically	VECSEL with current aperture	2.34 µm (multimode)	1.5 mW (pulsed at 288 K)

Tab. 1.1: *Overview of the GaSb-based surface-emitting lasers on GaSb substrate realized up to now.*

A growing interest in semiconductor lasers emitting in the MIR wavelength regime has put antimonide lasers in the spotlight within the last decade. Meanwhile, CW-operating GaSb-based edge-emitters between 2 µm and 3.6 µm at RT have already been realized [20, 21]. Such lasers are often used in gas sensing systems when a high output power is required, for example, for open path systems or remote gas detection. Modern TDLAS-based gas sensing systems sometimes are equipped with distributed feedback (DFB) lasers which can be an alternative light source to VCSELs. Antimonide DFB lasers with emission wavelengths between 2 µm and 2.8 µm were successfully fabricated using the technology of lateral Bragg grating incorporated in the laser structure [22, 23]. Recently the emission wavelength of such type of lasers has been extended to 3.4 µm utilizing type-I quantum well epitaxial material with an active region constituted of a GaInAsSb/AlGaInAsSb [24]. The whole scenario of accessing the very long wavelength range by realizing different semiconductor lasers is depicted in Fig. 1.1.

The Research group at the Fraunhofer Institute (IAF), Freiburg, Germany, has focused on optically-pumped (OP) VECSELs which combine the wavelength versatility and efficiency of diode lasers with the capability of emitting high output power in a circular, nearly diffraction-limited beam. These are advantageous features of many potential applications, e.g. gas sensing, communications, and materials processing. This research group has already

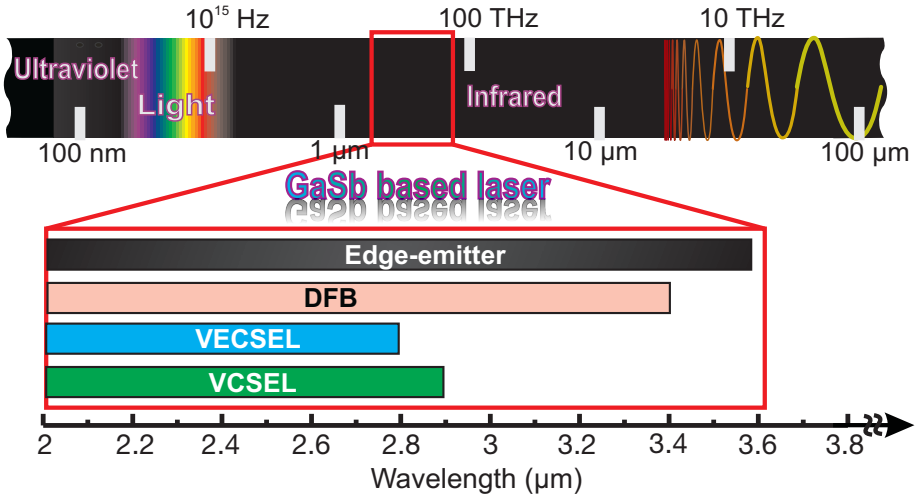

Fig. 1.1: *Optical spectrum and zoomed-in portion of the mid-infrared wavelength regime, illustrating the access of the wavelength range worldwide by different type of conventional semiconductor laser on GaSb substrate based on interband recombination of electron and hole.*

developed OP-VECSELs based on the (AlGaIn)(AsSb) material system for the wavelength range between 2.0 and 2.8 µm [25]. Recently, this group has demonstrated devices emitting at 2.8 µm with a CW output power of up to 120 mW at a submount temperature of 20°C, while under pulsed excitation, more than 500 mW peak output power were obtained. These results for a 2.8 µm emitting device show the potential for optically-pumped VECSELs to be significantly expanded toward 3 µm and beyond, while still obtaining acceptable device performance at room temperature.

Research collaborators from Tampere, Finland and WSI, Munich, Germany, have published results on electrically-pumped GaSb-VECSELs with a curved output coupler emitting at 2.34 µm [26]. Devices utilized BTJ as current aperture. The peak output power of such devices was limited to about 1.5 mW in pulsed operation at 15°C mount temperature. The power could be limited by thermal effects and it is likely that better results would be obtained by using more advanced thermal management techniques, such as diamond heat spreader element or flip-chip processing.

The University of Montpellier 2 Team fabricated several OP-VECSELs with dielectric Bragg mirror as an external optical cavity to demonstrate a CW single-mode emission operating between 2.3 µm and 2.7 µm [17]. For instance, devices at 2.3 µm exhibit CW single frequency operation above RT with an output power of more than 5 mW. The maximum temperature of operation was 350 K. In terms of output power, beam quality and laser linewidth, devices were well-adapted to spectroscopic applications.

Also EP, mesa-constricted VCSELs emitting between 2.2 µm and 2.63 µm were realized by the University of Montpellier 2 Team. The whole structure of these devices was grown monolithically in one run without any current aperture by MBE. RT and CW operation of such lasers emitting near 2.3 µm with a maximum temperature of operation 294 K was achieved [27]. A CW threshold current density as low as 1.1 kA/cm^2 was obtained at 284 K

for 60 µm diameter devices (20 µm diameter emitting area). The emission wavelength was extended to 2.63 µm which is the longest wavelength ever reported for any EP-VCSELs [28]. A quasi-CW (1 µs, 5%) operation was obtained at room temperature for 35 µm diameter devices with threshold current of 85 mA. But such devices without any current aperture exhibit multimode operation. Thus devices lose its usability in gas sensing applications since lasers with single-mode emission are required in gas sensing applications by tunable diode laser absorption spectroscopy (TDLAS) [29].

With a joint collaboration of Naval Research Laboratory, USA and Hughes Research Laboratory, USA the fabrication and operation of a VCSEL structure emitting in the 2-3 µm wavelength regime was reported. It was also the first work realized on a GaSb-substrate with Sb-based type-II active region. The primary results are on OP-VCSELs consisting of a semiconductor bottom mirror, 'W' quantum-well active region and dielectric top mirror emitting at 2.9 µm which operates up to 280 K in pulse mode [30]. Later these groups published results using the same structure operating in the CW regime up to 160 K and exhibiting multimode emission [31].

EP and CW-operating GaSb-based single-mode VCSELs emitting at 2.3-2.6 µm [32, 33] have also been demonstrated recently. The devices incorporate an epitaxial distributed Bragg reflector (DBR) as bottom mirror, grown on GaSb-substrate, a quantum well active region with quaternary GaInAsSb and a dielectric DBR as top mirror. For electrical and optical confinement, a buried tunnel junction is used. Devices exhibits CW emission with threshold currents of only several milliamperes. The lasers emit longitudinally as well as transversely in the single fundamental mode and are tunable over several nanometers. Therefore, they are very well suited for gas sensing applications by TDLAS and proven to be application-suited [12].

1.3 Gas Sensing: Principles and Operation

Nowadays most photonic sensors are developed utilizing TDLAS concept which is a technique for measuring the concentration of certain gas species using tunable diode lasers. The key advantage of TDLAS-based sensors is their long term stability and low cross sensitivity to other gas species. Apart from this obvious advantage, some other important benefits, such as high selectivity due to the small linewidth of the laser source, rapid response time and high sensitivity can be obtained from this powerful technique. Another important advantage offered by this technique is the possibility of developing a calibration-free-sensor which supersedes most traditional measurement techniques in gas analysis.

A gas molecule can be identified by its characteristic absorption spectra since each of the gas species has its unique spectral fingerprint. When the emission wavelength of a tunable diode laser is tuned across a characteristic absorption line of the absorbing medium or when the frequency (or wavelength) of the emitted light matches the rotational or vibrational frequency of the molecule, the signal intensity measured by the photodiode will decrease according to the Lambert-Beer law [34]:

$$\frac{I'}{I_0} = e^{-\int_0^L \alpha(\lambda,T,P,c)\,dL} \tag{1.1}$$

where I' is the measured light intensity at the photodiode, I_0 the emitted light intensity of

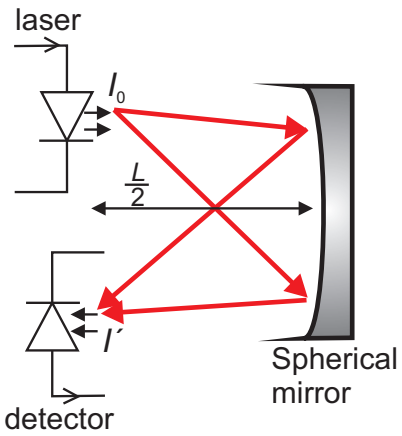

Fig. 1.2: *A schematic of a basic TDLAS setup.*

a light source, L (cm) the path length, and $\alpha(\lambda, T, P, c)$ (cm^{-1}) the absorption coefficient (depending on wavelength, temperature, pressure and concentration) of the absorbing gas. The absorption coefficient is a path-integrated value that will give an average measurement across the path length. Fig. 1.2 displays a basic TDLAS setup consisting of a tunable diode laser source with controllers for tuning, beam shaping optics, a gaseous absorbing region and a photodiode for detection. Light is focused on the detector using a spherical mirror which also extends the path length to L, where the distance between the laser and the spherical mirror is $L/2$.

Common experimental gas sensing methods in TDLAS involve the use of modulation spectroscopy which can take two forms: wavelength modulation spectroscopy (WMS) [35, 36] and frequency modulation spectroscopy (FMS) [37]. The underlying principles for these two methods are the same. But there is a basic difference between these two methods. In WMS, the modulation frequency is smaller than the half of the absorption linewidth (and certainly the laser linewidth) whereas in FMS, the modulation frequency is larger. In general, the signal corresponding to the output wavelength of the laser is modulated at a high frequency, while the DC component is tuned across the wavelength of interest. The signal received by the detector is then processed by a lock-in amplifier which simultaneously retrieves the first (1f) and second (2f) harmonics of the absorption profile by referencing the modulation frequency and its second multiple. WMS method has the advantages of efficient noise suppression, i.e. insusceptible to 1/f noise and removal of the laser amplitude modulation in the measured data. In addition to these advantages, WMS has several other benefits which make it desirable over direct absorption spectroscopy due to the low spectral background.

In most practical cases, TDLAS based sensor using such modulation techniques need a diode laser able to exhibit single-mode emission with a wide tuning range and preferably electrically-pumped operating in the CW mode and at room temperature (RT). Low-cost devices with low power consumption are also advantageous. Meeting well all these above-mentioned requirements, GaSb-based VCSELs at 2.3 µm using WMS have been utilized for

developing a sensor to detect carbon monoxide (CO) and methane (CH_4) gases simultaneously in ppm range [12].

2 Fundamentals of VCSELs

Vertical-cavity surface-emitting lasers (VCSELs) are the youngest members of semiconductor laser diode family. Many superior characteristics of VCSEL diodes result directly from the device structure. Discussion in this chapter aims to give a brief theoretical overview of the VCSEL fundamentals and theory as well as its inherent properties. Several parameters relating to device operation, design and characteristics will be introduced here which will be frequently used in the subsequent chapters.

2.1 Device Structure

A schematic cross-section of the GaSb-based VCSEL is illustrated in Fig. 2.1. Utilizing a twofold epitaxial growth process, the VCSEL structure was grown with a Varian Mod Gen II-MBE system equipped with solid sources and valved cracker cells for Arsenic and Antimony. The first epitaxial run starts with the growth of a bottom n-doped distributed Bragg reflector (DBR). Then, the active region is deposited consisting of quantum wells separated by barriers. The first epitaxial growth is finished by the heavily doped tunnel junction layers which define the active area of the device after structuring by conventional UV lithography and subsequent etching. Then, an n-doped current spreading layer and a highly doped contact layer are deposited in the second epitaxial run. The top dielectric DBR mirror is deposited as a last step of device manufacturing.

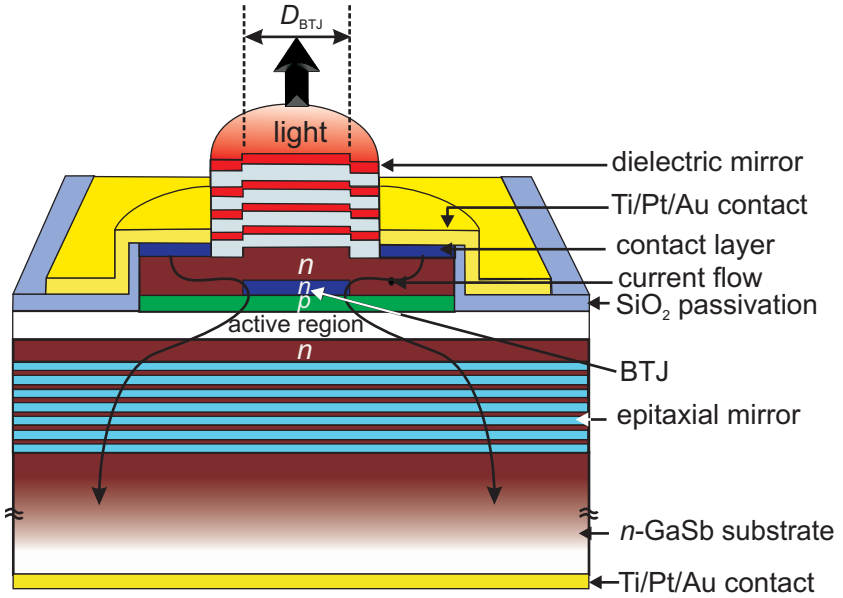

Fig. 2.1: *Schematic cross-sectional view of a buried tunnel junction (BTJ) top-emitting vertical-cavity surface-emitting laser. The direction of current flow is shown. D_{BTJ} is the device aperture diameter defined by the BTJ.*

2.2 Device Operation

The onset of the laser operation is best described by the oscillation condition, requiring that the optical field reproduces itself exactly in amplitude and phase after one cavity round trip. The general laser equation requiring optical gain g and constructive feedback in a resonator made of two mirrors with amplitude reflection coefficients r_1 and r_2 separated by length L is given as

$$r_1 r_2 e^{-2j\beta L} = 1 \tag{2.1}$$

where β is the complex propagation constant of the active material defined by

$$\beta = \frac{2\pi}{\lambda} n_{\mathrm{C}} + j\left(\frac{g_{\mathrm{m}} - \alpha_{\mathrm{i}}}{2}\right) \tag{2.2}$$

where λ is the vacuum wavelength, n_{C} the average refractive index of the cavity, $(g_{\mathrm{m}} - \alpha_{\mathrm{i}})$ the net mode gain which can be denoted by g_{net} and α_{i} the internal loss which includes all losses, e.g. optical absorption, diffraction etc.

Considering the imaginary part of the oscillation condition and taking into account the periodicity of the exponential function with respect to imaginary arguments gives the phase condition

$$m\lambda = 2n_{\mathrm{C}}L \tag{2.3}$$

where m is a positive integer. In devices under study, $m = 6$, i.e. the inner cavity is 3λ thick.
Taking the real part of Eqn. 2.1 into consideration, the amplitude condition can be written as

$$g_{\mathrm{net}} = \alpha_{\mathrm{m}} \tag{2.4}$$

where α_{m} is the mirror loss which can be defined from Eqn. 2.1 and using $L = L_{\mathrm{eff}}$ and $R_{\mathrm{oc}} = |r_1|^2$ and $R_{\mathrm{b}} = |r_2|^2$ for VCSEL

$$\alpha_{\mathrm{m}} = \frac{1}{2L_{\mathrm{eff}}} \ln\left(\frac{1}{R_{\mathrm{oc}} R_{\mathrm{b}}}\right) \tag{2.5}$$

with L_{eff} as the effective cavity length (introduced in Sect. 2.3) and R_{b} and R_{oc} as power reflectivities for the VCSEL bottom and top/outcoupling mirror, respectively.
Using $g_{\mathrm{net}} = g_{\mathrm{m}} - \alpha_{\mathrm{i}}$, Eqn. 2.4 becomes

$$g_{\mathrm{m}} = \alpha_{\mathrm{i}} + \alpha_{\mathrm{m}} = \alpha_{\mathrm{tot}} \tag{2.6}$$

where g_{m} is the mode gain needed to compensate the total loss in the laser resonator which can be expressed by the confinement factor Γ (introduced in Sect. 2.4) and the active region gain g_{a}. Therefore,

$$g_{\mathrm{m}} = \Gamma g_{\mathrm{a}} \tag{2.7}$$

2.3 Bragg Mirrors

By utilizing distributed Bragg reflectors (DBRs), the required VCSEL mirror with a high reflectivity can be realized. Since the VCSEL gain section in the longitudinal direction is

very short compared to edge-emitters, VCSEL needs DBRs with a reflectivity of more than 99% in order to compensate the internal and mirror loss. A Bragg mirror pair consists of at least two layers with two different refractive indices. Each layer is optically quarter wave thick. By repeating the layer sequence, constructive interference is achieved, which increase the total reflectivity of the structure.

The DBR is mainly characterized by the maximum attainable reflectivity, the phase and the stopband width. The total maximum reflectivity R of a Bragg stack composed of M pairs is given by [38]

$$R = \left(\frac{1 - \frac{n_\mathrm{s}}{n_\mathrm{a}} \left(\frac{n_\mathrm{l}}{n_\mathrm{h}} \right)^{2M}}{1 + \frac{n_\mathrm{l}^2}{n_\mathrm{a}\, n_\mathrm{s}} \left(\frac{n_\mathrm{l}}{n_\mathrm{h}} \right)^{2M}} \right)^2 \tag{2.8}$$

with refractive indices n_a and n_s of surrounding and substrate materials, respectively, and n_h and n_l of high and low index Bragg mirror materials, respectively.

An analytic expression for the spectral width of the high reflectivity stopband can be deduced as [38]

$$\Delta\lambda_\mathrm{DBR} = \frac{4}{\pi}\, \lambda_0\, \arcsin\left(\frac{n_\mathrm{h} - n_\mathrm{l}}{n_\mathrm{h} + n_\mathrm{l}} \right) \tag{2.9}$$

It is clear that the stopband width is proportional to the refractive index difference n_h - n_l which is termed as mirror contrast Δn.

The VCSEL resonator is formed by joining two DBRs together, where the distance L basically determines the resonance wavelength. Due to the distributed reflectivities, the optical standing wave penetrates into the mirrors, necessitating the definition of an effective cavity length L_eff as [39]

$$L_\mathrm{eff} = L + L_\mathrm{eff,oc} + L_\mathrm{eff,b} \tag{2.10}$$

being the sum of the inner resonator L and the penetration depths $L_\mathrm{eff,oc}$ and $L_\mathrm{eff,b}$ of the standing wave pattern into the top and bottom mirrors, respectively. The penetration depth can be calculated by [40]

$$L_\mathrm{eff,oc/b} = \frac{\lambda}{4\Delta n} \tanh\left(\frac{M}{2} \left[\frac{n_\mathrm{h}}{n_\mathrm{l}} - \frac{n_\mathrm{l}}{n_\mathrm{h}} \right] \right) \tag{2.11}$$

2.4 Longitudinal Confinement Factor

The confinement factor expresses the overlap between the gain regions and the electric field standing wave pattern within the cavity. For a three-dimensional structure, the confinement factor can be defined as [41]

$$\Gamma = \Gamma_x\, \Gamma_y\, \Gamma_z \tag{2.12}$$

where Γ_x and Γ_y are lateral confinement factors in x and y directions, respectively. Due to a large lateral dimension, $\Gamma_x = \Gamma_y \approx 1$. Unlike edge-emitting lasers, longitudinal confinement factor Γ_z is a critical design parameter in VCSELs. Considering the overlap of the standing

wave pattern of the electric field with the active region, the longitudinal confinement factor can be defined as [41]

$$\Gamma_z = \frac{\int_{d_{QW}} |E(z)|^2 dz}{\int_{L_{eff}} |E(z)|^2 dz} = \frac{N_{QW} L_{QW}}{L_{eff}} \Gamma_r \tag{2.13}$$

where $|E(z)|$ is the amplitude of the longitudinal standing wave field, d_{QW} the total thickness of the active layers with the odd number of quantum wells N_{QW} having the thickness L_{QW} each and L_{eff} the total cavity length, including the penetration depths into the DBRs. At this point, it is necessary to introduce relative confinement factor or gain enhancement factor Γ_r introduced in Eqn. 2.13 which is nothing but a longitudinal confinement factor with respect to the simple geometrical filling factor Γ_f [41]

$$\Gamma_r = \frac{\Gamma_z}{\Gamma_f} = \frac{\Gamma_z}{\left(\frac{N_{QW} L_{QW}}{L_{eff}}\right)} \tag{2.14}$$

For all further analysis, the material gain coefficient g of the QWs has to be modified to $\Gamma_r g$. In other words, the threshold gain in the laser resonator can be reduced by a factor of Γ_r by increasing the material gain with a factor of Γ_r.
Considering an active region made of a number of QWs N_{QW} with equal gain at each QW, located at positions $z_{il} \leq z \leq z_{ih}$, the relative confinement factor of the active region can be calculated as [39]

$$\Gamma_r^{act} = 1 + \frac{\lambda}{4\pi n_C} \frac{\sum_{i=1}^{N_{QW}} \sin\left(\frac{4\pi n_C z_{ih}}{\lambda}\right) - \sin\left(\frac{4\pi n_C z_{il}}{\lambda}\right)}{N_{QW} L_{QW}} \tag{2.15}$$

where n_C is the longitudinally field weighted average refractive index of the resonator which can be computed by [42]

$$n_C = \sqrt{\frac{\int_{-\infty}^{\infty} n^2(z)|E(z)|^2 dz}{|E(z)|^2}} \tag{2.16}$$

2.5 Lateral Confinement Factor

Transverse modes of circular-shaped VCSELs can be approximated by linearly polarized (LP_{lp}) modes [43]. The indices l and p are the azimuthal and radial transverse mode numbers, respectively. In a perfectly circular device, the sine and cosine solutions are degenerate and thus the two intensity distributions can arbitrarily be superimposed. Fig. 2.2 shows the intensity distributions of the five lowest transverse LP_{lp} modes in a VCSEL with a certain core diameter. In the following discussion, only these five LP modes will be considered for a multimode device though several other higher order modes will appear in the device simultaneously.

The effective gain experienced by a mode can be understood by the lateral confinement factor $\Gamma_{lateral}$. With increasing active diameter, the mode overlap with the central region

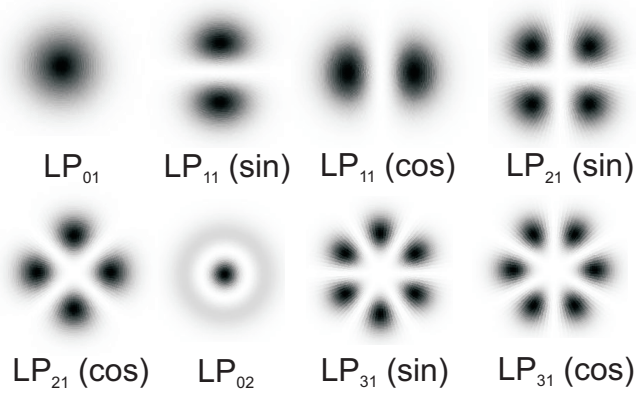

Fig. 2.2: *2D Intensity distribution of the five lowest LP-transverse modes in a VCSEL. Both cos and sin solutions of individual modes are displayed*

of a cavity increases and hence Γ_{lateral} does. When no selection mechanism is applied to select a certain transverse mode, the fundamental mode has the highest value of Γ_{lateral}. This parameter is determined by the fraction of the total optical power propagating in the region with BTJ [44]

$$\Gamma_{\text{lateral}} = \frac{P_{\text{C}}}{P_{\text{C}} + P_{\text{Cl}}} = \frac{\int_0^{\frac{D_{\text{BTJ}}}{2}} |E(r)|^2 r \mathrm{d}r}{\int_0^{\infty} |E(r)|^2 r \mathrm{d}r} \tag{2.17}$$

with $|E(r)|$ as the electric field strength in the transverse direction, P_{C} and P_{Cl} as the powers in the central region and peripheral region of the resonator, respectively. Fig. 2.3 illustrates Γ_{lateral} as a function of active diameter in a BTJ VCSEL at 2.3 µm for the five lowest transverse modes.

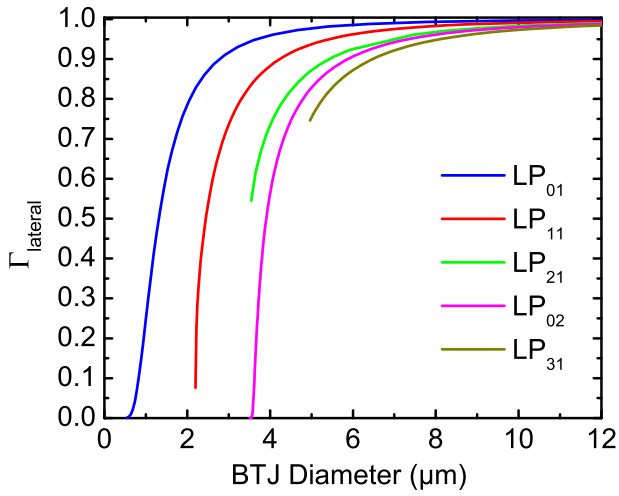

Fig. 2.3: *Dependence of the lateral confinement factor Γ_{lateral} on the BTJ diameter for VCSELs at 2.3 µm for the five lowest LP modes.*

2.6 Threshold Gain

Despite much shorter gain length in a VCSEL compared to edge-emitting laser (EEL), three following major effects play roles in VCSELs which contribute to make the threshold gain comparable with EEL:

1. Increased Γ_{lateral}
2. High reflectivity in the mirror
3. Gain enhancement factor due to standing wave

The increased Γ_{lateral} is due to the unique VCSEL geometry. The optical mode overlaps the gain region over a large portion of the waveguide in the lateral direction, rather than just a small fraction as in EEL. The non-transmissive DBR usually has a reflectivity of over 99.5% as already mentioned in Sect. 2.3. Finally, the standing wave effect in the active region is taken into account by Γ_{r} which allows to almost double the available amount of optical amplification.

2.7 Longitudinal Modes in VCSELs

One of the unique features of VCSELs is their inherent single longitudinal mode emission. This is just due to the short resonator length which is in the range of a few microns. Such behavior can be well understood by the longitudinal-mode spacing between the emission wavelength λ_0 and the adjacent mode. Mathematically this mode spacing $\Delta\lambda_{\text{l}}$ can be estimated as

$$\Delta\lambda_{\text{l}} \approx \frac{\lambda_0^2}{2L_{\text{eff}}n_{\text{C}}} \tag{2.18}$$

where n_{C} can be calculated by Eqn. 2.16.
For instance, with $L_{\text{eff}} \approx 3\,\mu\text{m}$ and $n_{\text{C}} \approx 3.6$ in 2.3 µm VCSELs, $\Delta\lambda_{\text{l}}$ amounts to approximately 245 nm which is larger than the bottom epitaxial mirror stopband width and even being larger than the spectral gain bandwidth of the QW material. Hence, a single longitudinal mode is excited in a VCSEL with a short resonator length. Though multiple longitudinal modes might lase if the cavity is made too long [45] which is not the case in the present work.

2.8 Transverse Modes in VCSELs

Excitation of multiple transverse modes is a common phenomenon in VCSELs even of its single longitudinal-mode emission. This is just because of a relatively large optical cavity in the transverse direction as well as the strong waveguiding in VCSELs. Pure longitudinal and transverse single-mode emission is highly desirable for most of the potential applications.

- **Transverse mode spacing**
  The transverse mode spacing between fundamental mode and first higher order mode is an important parameter in VCSELs by which the amount of optical waveguiding can be estimated and based on that analysis, single fundamental mode operation can be

optimized [46]. The transverse mode spacing in VCSELs is affected by the aperture diameter, emission wavelength and the index guiding. Compared to GaAs-based VCSELs, GaSb-based BTJ VCSELs for a certain aperture diameter possess larger transverse mode spacing. Therefore, single-mode operation even in large-aperture GaSb-VCSELs can be easily confirmed from common spectra measurements. The large mode spacing in these devices is just because of the longer emission wavelength and the higher index step caused by the BTJ. The mode spacing $\Delta\lambda_{\mathrm{t}}$ between modes LP_{lp} and LP_{l*p*} is [47]

$$\Delta\lambda_{\mathrm{t}} = \mid \lambda_{lp} - \lambda_{l*p*} \mid \tag{2.19}$$

$$= \mid 2(p^* - p) + (l^* - l) \mid \frac{\lambda^3}{2\pi^2 w_0^2 n_{\mathrm{C}}^2} \tag{2.20}$$

where λ is the emission wavelength and w_0 the spot radius which is given by [48]

$$w_0 = \frac{D_{\mathrm{BTJ}}}{2\sqrt{\ln(V)}} \tag{2.21}$$

where V is the normalized frequency parameter introduced in Sect. 2.9. Eqn. 2.21 is valid for step refractive index profile produced in the cavity with tunnel junction. It is not surprising that the combinations of l and p representing LP modes resulting in $\Delta\lambda_{\mathrm{t}} = 0$ in Eqn. 2.20. It means that those modes (e.g. LP_{21} and LP_{02}) are frequency degenerated since they have the identical $(2p+l)$ values where for any type of mode profile, $(2p+l)$ is the mode group number [43]. But in reality, a lack of isotropy in the material or a geometric asymmetry could introduce a lifting of the frequency degeneracy in these modes and give a non-zero $\Delta\lambda_{\mathrm{t}}$ value. According to Eqn. 2.20, the mode spacing between two adjacent modes is equal and can be written as follows [47]

$$\begin{aligned}\Delta\lambda_{\mathrm{t}} &= \lambda_{01} - \lambda_{11} = \lambda_{11} - \lambda_{21} \\ &= \frac{\lambda^3}{2\pi^2 w_0^2 n_{\mathrm{C}}^2} = \frac{2\lambda^3 \ln(V)}{\pi^2 D_{\mathrm{BTJ}}^2 n_{\mathrm{C}}^2} \\ &= \frac{2\lambda^3 \ln\left(\dfrac{\pi D_{\mathrm{BTJ}}}{\lambda}\sqrt{n_{\mathrm{C}}^2 - n_{\mathrm{Cl}}^2}\right)}{\pi^2 D_{\mathrm{BTJ}}^2 n_{\mathrm{C}}^2}\end{aligned} \tag{2.22}$$

It is seen that the mode spacing is proportional to the emission wavelength and the index guiding and inversely proportional to the BTJ diameter of the device. Eqn. 2.22 might be used to estimate the effective refractive index difference n_{C} - n_{Cl} from the measured mode spacing and known data of n_{C}, λ and D_{BTJ} of a device.

As expected, the transverse mode spacing $\Delta\lambda_{\mathrm{t}}$ decreases with increasing the device aperture diameter as illustrated in Fig. 2.4. It should be noted that $\Delta\lambda_{\mathrm{t}}$ scales with inverse device aperture diameter squared, whereas longitudinal mode spacing $\Delta\lambda_{\mathrm{l}}$ does with the inverse resonator length.

- **Far-fields**
  When propagating LP_{01} mode distribution, the spot size w_{z} at a distance z along the beam from the beam waist for a beam of wavelength λ is given by [49]

$$w_z^2 = w_0^2\left(1 + \frac{z^2}{z_{\mathrm{R}}^2}\right) \tag{2.23}$$

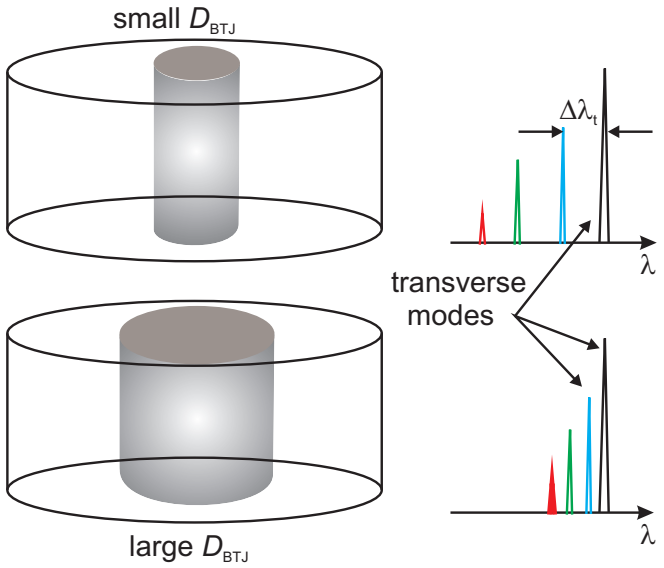

Fig. 2.4: *Schematic representation of multimode VCSELs with different size of aperture diameter and the associated spectra to illustrate the transverse mode spacing.*

with the Rayleigh distance z_R of the beam in air, for which

$$z_R = \frac{\pi w_0^2}{\lambda} \tag{2.24}$$

In the far-field approximation, $z \gg z_R$ and using Eqn. 2.24, w_z can be written as

$$w_z = \frac{z\lambda}{\pi w_0} \tag{2.25}$$

This allows us to specify a formula for the full-width at half-maximum (FWHM) angle

$$\Theta_{FWHM} = 2\sqrt{\ln 2}\,\tan^{-1}\left(\frac{\lambda}{\pi w_0}\right) \tag{2.26}$$

Replacing w_0 by simply $D_{BTJ}/2$

$$\Theta_{FWHM} \approx 2\sqrt{\ln 2}\,\tan^{-1}\left(\frac{2\lambda}{\pi D_{BTJ}}\right) \tag{2.27}$$

The approximation of Eqn. 2.27 is only valid when $D_{BTJ} = D_{BTJ,eff}$, where $D_{BTJ,eff}$ is the effective BTJ aperture diameter. But, usually $D_{BTJ} < D_{BTJ,eff}$ since the lateral current spreading between the BTJ defined current aperture and the active region as well as the lateral carrier diffusion in the active region lead to a broadening of the effectively pumped area in the active region. This will be discussed in Chap. 6

2.9 Single-Mode Operation

It is known that VCSEL can be approximated as a cylindrical step-index optical fiber. Knowing the core and cladding refractive indices, it is possible to apply waveguide analysis to find the mode cutoff. By normalizing the BTJ diameter with respect to the free space wavelength of operation λ, the mode cutoff is determined by a normalized frequency parameter V which can be represented by the following relation [43]

$$V = \frac{\pi D_{\mathrm{BTJ}}}{\lambda}\sqrt{n_{\mathrm{C}}^2 - n_{\mathrm{Cl}}^2} \tag{2.28}$$

where V parameter could equally well be referred to as the normalized core diameter.

Now, the phase parameter or the normalized effective refractive index B is introduced to evaluate the single-mode condition. This parameter provides insight into the actual mode distribution via the effective refractive index n_{eff}. In other words, the effective refractive index seen by each transverse mode can be expressed by the phase parameter which is defined by [44]

$$B = \frac{n_{\mathrm{eff}}^2 - n_{\mathrm{Cl}}^2}{n_{\mathrm{C}}^2 - n_{\mathrm{Cl}}^2} \tag{2.29}$$

Therefore, the single-mode condition is simply represented by

$$V < 2.405 \tag{2.30}$$

where no optical loss is assumed.

By using this single-mode condition, for instance, 2.3 µm VCSELs with $D_{\mathrm{BTJ}} \geq 2.3\,\mu\mathrm{m}$ (shown in Fig. 2.5 by plotting B against BTJ diameter) are supposed to support multiple transverse modes.

But, experimentally the devices with larger apertures (compared to the values estimated by Eqn. 2.28 and 2.30) emit in a single fundamental mode with a reasonable side-mode suppression ratio (SMSR) i.e. > 25 dB. Therefore, these devices are 'single-mode lasers' as well. As a matter of fact, single-mode lasers may have a laser cavity that supports multiple modes but only the fundamental mode lases. The reason behind this is mode-selective loss in the cavity. In other words, the losses for all excited modes are not same in the cavity of a device, i.e. the loss of higher order modes in single-mode lasers with multimode cavities is too high for gain to compensate and thus lasing to occur.

2.10 Laser Parameters

Now the device performance related parameters or the so-called characteristic laser parameters will be presented by means of basic equations or required formulas. Most of these parameters relating to the device steady-state operation are the primary source of information on overall device performance.

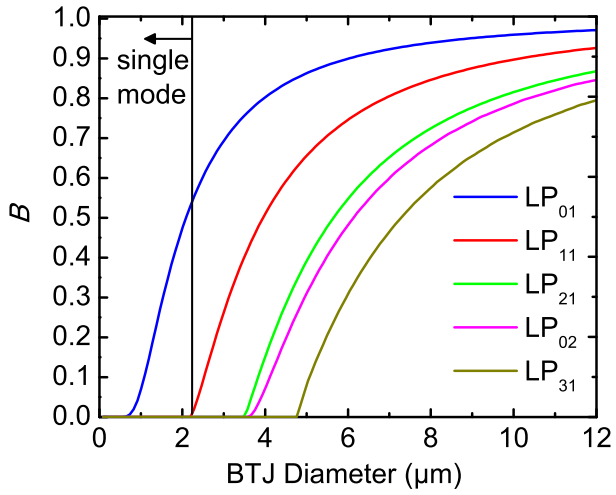

Fig. 2.5: *Dependence of the phase parameter B on the BTJ diameter of VCSELs at 2.3 μm for the five lowest LP modes.*

Generation of output power is the primary concern in a laser. Above threshold, the total optical power of a VCSEL P_{opt} can be defined by

$$P_{\mathrm{opt}} = \eta_{\mathrm{i}} \frac{\mathrm{h}\nu}{e} \frac{\alpha_{\mathrm{m}}}{\alpha_{\mathrm{tot}}} (I - I_{\mathrm{th}}) \tag{2.31}$$

where η_{i} is the internal quantum efficiency which tells the fraction of injected carriers that reach the active region and recombine radiatively.
Next we consider the differential quantum efficiency η_{d} indicating the fraction of injected carriers which, converted into photons above laser threshold, appears as light output. In other words, it measures the differential rate of emitted photons divided by the differential rate of injected electrons or electron-hole pairs which can be easily determined from the slope of the laser output characteristics. Differentiating P_{opt} in Eqn. 2.31 with respect to the applied current, η_{d} can be calculated by

$$\eta_{\mathrm{d}} = \frac{e}{\mathrm{h}\nu} \frac{\mathrm{d}P_{\mathrm{opt}}}{\mathrm{d}I} \tag{2.32}$$

$$= \eta_{\mathrm{i}} \frac{\alpha_{\mathrm{m}}}{\alpha_{\mathrm{tot}}} \tag{2.33}$$

Eqn. 2.33 can now be written as

$$\frac{1}{\eta_{\mathrm{d}}} = \frac{\alpha_{\mathrm{i}}}{\eta_{\mathrm{i}}} \cdot \frac{1}{\alpha_{\mathrm{m}}} + \frac{1}{\eta_{\mathrm{i}}} \tag{2.34}$$

with α_{i} as the internal loss of VCSELs. Experimentally α_{i} and η_{i} can be determined by plotting inverse η_{d} against inverse α_{m}. The y-axis intercept defines η_{i} and with the slope of the graph, α_{i} can be calculated.

Empirical gain coefficient (g_0) of the active region material and transparency current density J_{tr} are two important laser parameters for the multi-quantum well (MQW) laser. The QW

gain and current density can be related by a semi-logarithmic function [50]

$$g_{\mathrm{th}} = g_0 \ln\left(\frac{\eta_{\mathrm{i}} J_{\mathrm{th}}}{N_{\mathrm{QW}} J_{\mathrm{tr}}}\right) \tag{2.35}$$

where g_{th} is the threshold gain to reach at threshold and J_{th} the threshold current density of VCSELs.

2.11 Round-Trip Gain and Loss

It is very important to be familiar with round-trip gain or loss used in analyzing VCSELs. To understand this mechanism, one has to consider the optical traveling wave and standing wave within the cavity. Considering a traveling wave at first, the light passes through the gain medium and being amplified. Then the high reflective mirror reflects a significant of the light power which is amplified again after passing through the gain medium. The power bounces off the second mirror and hence the process repeats. While the light power bounces back and forth in the cavity, there are several effects that contribute to its loss of power including material absorption loss, diffraction loss, transmission through the mirrors, etc. Lasing takes places when the round trip optical gain equals the losses.

Considering the traveling wave, the gain and loss add exponentially per pass within the cavity as given by

$$P' = P_0 \exp(g\, d_{\mathrm{QW}}) = P_0 \exp(g\, N_{\mathrm{QW}} L_{\mathrm{QW}}) \tag{2.36}$$

$$P'' = P_0 \exp(-\alpha_{\mathrm{t}} L_{\mathrm{eff,oc}} - \alpha_{\mathrm{b}} L_{\mathrm{eff,b}} - \alpha_{\mathrm{cl}}(L - d_{\mathrm{QW}}) - \alpha_{\mathrm{a}} d_{\mathrm{QW}}) \tag{2.37}$$

where P' or P'' is the final power, P_0 the initial power, α_{t} the absorption loss in the top dielectric mirror, α_{b} the absorption loss in the bottom epitaxial mirror, α_{a} the active region loss and α_{cl} the loss in the cladding material. For simplification, it is logical to make an approximation for the addition of the gain or loss linearly since the thickness of the gain medium through which the optical mode passes is very thin. In other words, gd_{QW}, the single pass gain through a QW region is usually less than 1% which allows to be considered $\exp(gd_{\mathrm{QW}}) \approx 1 + gd_{\mathrm{QW}}$. So, in case of VCSELs, it is correct to use the linear version of the gain-equals-loss condition instead of the exponential one used in edge-emitters. Therefore, for threshold, the following simple formula can be used

$$G' = L' + T_{\mathrm{b}} + T_{\mathrm{oc}} \tag{2.38}$$

where G' is the total round-trip gain and L' the round-trip loss includes absorption and diffraction loss in the resonator. T_{b} and T_{oc} are the transmission losses through bottom and top outcoupling mirror, respectively. In addition, for further simplification, the internal cavity loss α_{i} can be introduced by assuming the loss uniformly distributed in all layers within the cavity. Eqn. 2.38 becomes for round trip gain and loss,

$$g(2N_{\mathrm{QW}} L_{\mathrm{QW}}) = \alpha_{\mathrm{i}}(2L_{\mathrm{eff}}) + T_{\mathrm{b}} + T_{\mathrm{oc}} \tag{2.39}$$

Eqn. 2.39 is still not complete since only the traveling wave is considered into the discussion so far. However, in case of VCSELs, a standing wave is formed in the cavity and the power

of the standing wave peak becomes almost doubled. Since the standing wave peak is placed at the gain medium, the material gain becomes twice as high as in the traveling wave case. Introducing the standing wave factor, i.e. relative confinement factor in the gain term, Eqn. 2.39 can be modified to

$$\Gamma_r g(2N_{QW}L_{QW}) = \alpha_i(2L_{eff}) + T_b + T_{oc} \tag{2.40}$$

Again, recall Eqn. 2.7,

$$\begin{aligned} g_m &= \alpha_i + \frac{1}{2L_{eff}} \ln\left(\frac{1}{R_b R_{oc}}\right) \\ \Longrightarrow \Gamma_z g &= \alpha_i + \frac{1}{2L_{eff}} \left[\ln\left(\frac{1}{1-T_b}\right) + \ln\left(\frac{1}{1-T_{oc}}\right)\right] \end{aligned}$$

Using Eqn. 2.13 and $\ln\left(\frac{1}{1-T_b}\right) \approx T_b$ and $\ln\left(\frac{1}{1-T_{oc}}\right) \approx T_{oc}$, Eqn. 2.40 can be reobtained.

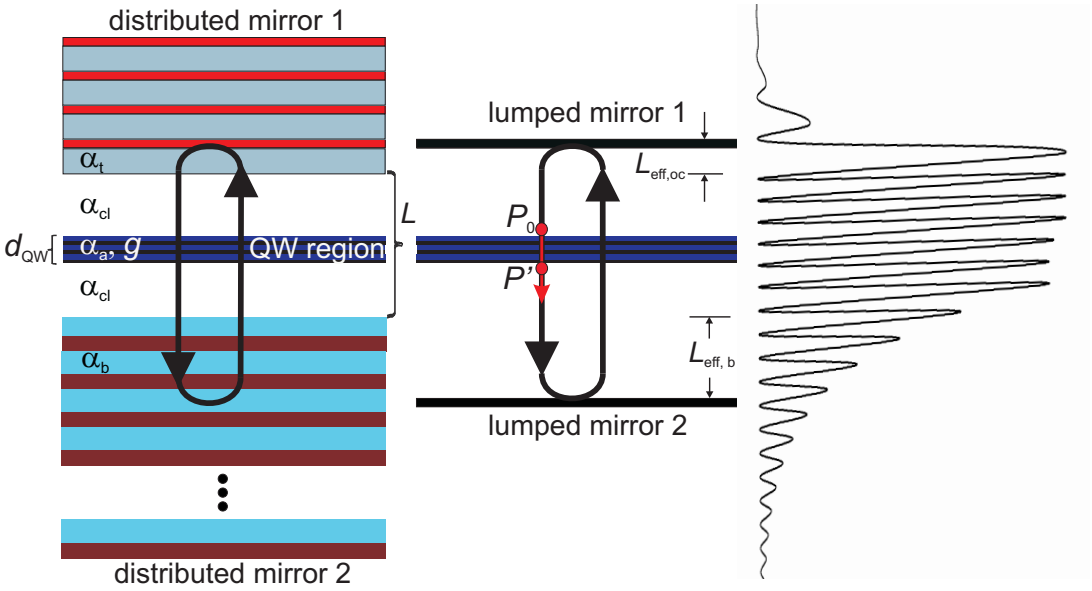

Fig. 2.6: *Simple schematic of VCSEL structure and even more simplified version by replacing the distributed mirror with lumped mirror along with standing wave pattern.*

2.12 Relative Intensity Noise

The commonly used figure of merit for VCSEL excess noise is the relative intensity noise (RIN) which limits the best sensitivity that can be achieved with absorption spectroscopy, defined as [50]

$$\mathrm{RIN} \equiv \frac{\langle \Delta P \rangle^2}{P_0^2} \tag{2.41}$$

where $\langle \Delta P \rangle$ is the time average of laser optical power fluctuation and P_0 is its average power. The RIN is often described as in decibels, or $10\log_{10}(\mathrm{RIN})$ and measured in dB/Hz.

$$\Delta P = \sqrt{\mathrm{RIN}_{\mathrm{dB}}}\, P_0 \tag{2.42}$$

The RF-analyzer sees a noise component with electrical power of

$$P_{\text{noise}} = I_{\text{noise}}^2 \, R_{50\,\Omega} = \frac{V_{\text{noise}}^2}{R_{50\,\Omega}} \tag{2.43}$$

where P_{noise} is the power of noise observed at the RF-analyzer, $R_{50\Omega}$ is the terminal resistance of the RF-analyzer ($50\,\Omega$). The square of voltage generated by the optical noise can be expressed in the form

$$V_{\text{noise}}^2 = (\Delta P \,.R\,.G)^2 \tag{2.44}$$

where R is the responsivity of the photodetector (PD), and G the transimpedance gain of the PD amplifier. This can be rewritten as

$$V_{\text{noise}}^2 = \text{RIN}\,.(P_0\,.R\,.G)^2 \tag{2.45}$$

Previously RIN was given in dB units, therefore we write here

$$V_{\text{noise}}^2 = 10^{\left(\frac{\text{RIN}_{\text{dB}}}{10}\right)}(P_0\,.R\,.G)^2 \tag{2.46}$$

Now we can write

$$P_{\text{noise}} = \frac{10^{\left(\frac{\text{RIN}_{\text{dB}}}{10}\right)}(P_0\,.R\,.G)^2}{R_{50\,\Omega}} \tag{2.47}$$

and

$$\frac{P_{\text{noise}} R_{50\,\Omega}}{(P_0\,.R\,.G)^2} = 10^{\left(\frac{\text{RIN}_{\text{dB}}}{10}\right)} \tag{2.48}$$

From here, an expression for RIN can be obtained as

$$\text{RIN}_{\text{dB}} = 10\log\left(\frac{P_{\text{noise}} R_{50\,\Omega}}{(P_0\,.R\,.G)^2}\right) \tag{2.49}$$

Since the power levels are expressed in dBm units at the RF-analyzer, it is necessary to convert to SI-units for the calculations

$$P = 10^{\left(\frac{P_{\text{dBm}}}{10}\right)} \times 0.001 \;\; (\text{W}) \tag{2.50}$$

Although there have been many studies on the RIN of VCSELs, they are focused on high frequency regions, driven by high-speed applications such as telecommunication and optical interconnection. But for VCSELs under study, RIN characteristics in the low frequency region is relevant to TDLAS-based gas sensing applications using WMS technique where lasers are subjected to a small sinusoidal modulation of the injection current in addition to a bias current. In general, VCSEL should have low intensity noise in the frequency regime of a few kHz which is essential for achieving high sensitivity in TDLAS-based photonic sensors. Usually VCSELs are operated well above threshold to obtain low RIN.

3 Design Issues for GaSb-VCSELs

3.1 Optical Design

For a successful Sb-based VCSELs design, one primarily requires a good optical design. This includes a good quality active region with low carrier leakage and low non-radiative recombination, an optimum number of QWs employed in the active region, realization of high reflectivity and low lossy mirror, cavity design with an optimum thickness, round trip gain and loss estimation and a reduced optical waveguiding for a single-mode operation. The careful control and then the successful implementation of these issues into the device will lead to a better device performance.

3.1.1 Active Region Design for 2.6 µm VCSELs

The active layer structure used in Sb-based VCSELs consists of QW active region embedded in an GaSb cladding. The active region has seven compressively strained 10 nm thick QWs with lattice-matched 8 nm thick GaSb barriers. The outer parts of the QWs are surrounded by 30 nm thick undoped GaSb barriers followed by the 60 nm thick doped AlGaAsSb separate confinement layers. The reason of using separate confinement layer is to prevent the carrier leakage from the active region. The important parameters of the active region employed in the presented devices is listed in Tab. 3.1.

QW material	$In_{0.43}Ga_{0.57}As_{0.15}Sb_{0.85}$
Barrier material	GaSb
QW thickness	10 nm
Barrier thickness	8 nm
QW compressive-strain (relaxed)	1.5%
Calculated QW bandgap	446 meV≡2780 nm
Conduction band offset* ΔE_c^{QW}	212 meV
Valence band offset* ΔE_{hh}^{QW}	48 meV

Tab. 3.1: *The parameters of the QW active region.*
** indicates that these values are calculated from the first quantized state.*

As known theoretically, by increasing the In-content in lattice-matched GaInAsSb up to around 60% the QW bandgap can be decreased to reach longer wavelengths. In devices under study, the In-content amounts to 43%. On the other hand, the QW strain can be controlled by the As-content. In fact, compressive strain is employed in QWs to suppress the Auger recombination process, which results in increase of the modal gain and reduction of threshold current density [51]. In addition, higher compressive strain in the active region increases the valence-band offset results in a good hole confinement [52].

The band diagram of the active region is displayed in Fig. 3.1. Due to a moderately large band offset in the conduction band, electrons remain very well-confined in QWs and impor-

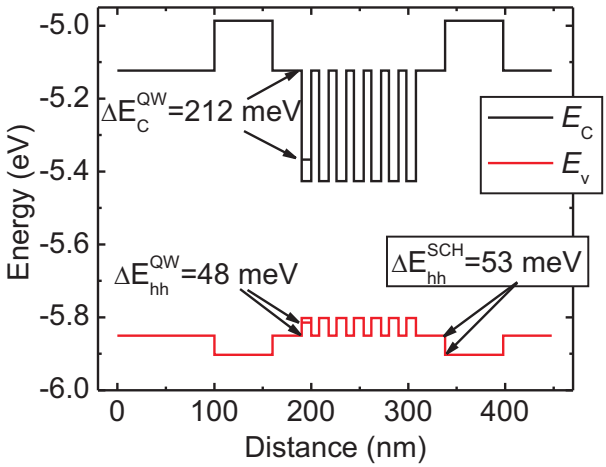

Fig. 3.1: *Band diagram of the active region, consisting of quaternary InGaAsSb embedded in GaSb barriers, employed in 2.6 µm VCSELs.*

tantly all QWs are homogeneously filled with electrons. In contrary, $\Delta E_{\mathrm{hh}}^{\mathrm{QW}}$ value is just less than twice of the thermal energy at room temperature ($k_{\mathrm{B}}T$). Therefore, hole leakage by thermionic emission could reduce the internal quantum efficiency η_{i} of the device. And the valence band offset $\Delta E_{\mathrm{hh}}^{\mathrm{SCH}}$ at the separate confinement layer $Al_{0.15}GaAsSb$ is approximately twice as low as $k_{\mathrm{B}}T$. Nevertheless, GaSb has been chosen as a barrier material in QW active region since GaSb barrier has:

- Lower $\Delta E_{\mathrm{c}}^{\mathrm{QW}}$ than AlGaAsSb barriers results in homogeneous band filling with carrier
- Sufficient hole confinement
- Promising results from edge emitting lasers with GaSb-barriers (see Chap. 5)
- Lower thermal resistance than AlGaAsSb barriers.

Fig. 3.2 shows a room-temperature photoluminescence (PL) spectrum of the active region discussed already. The measurement shows a PL peak of 2545 nm with a full-width half-maximum (FWHM) of 46 meV. This is an indication that the active region is of type-I and that the growth quality is good. The sharper peak and the smaller FWHM are characteristics of a higher gain active region.

Number of QWs

After choosing the active region material, it becomes necessary to pay attention to determine the number of QWs. The reduction of gain with increasing temperature presents a challenge in minimizing number of QWs. Utilizing too few QWs in VCSEL may result in an insufficient gain to sustain lasing at high temperature. In contrary, too many QWs will introduce excess optical losses in the cavity when all the wells are not homogeneously filled with carriers, leading to a poor device performance. In addition, a larger number of QWs may increase the intraband absorption losses in the cavity. Nevertheless, as a rule of thumb, the higher number of QWs is better when the material gain is not exactly known.

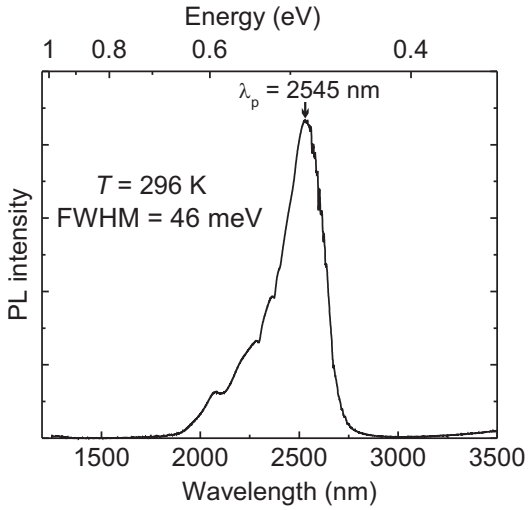

Fig. 3.2: *Room-temperature photoluminescence spectrum of the active region used in 2.6 µm VCSELs.*

As a rough estimation, we can calculate the optimum number of QWs, being suitable for VCSELs. In order to quantify the number, we first present calculations for Γ_r^{act}. Such calculations are displayed in Fig. 3.3 a) by varying the number of QWs. As can be seen here, too many QWs will reduce the value of Γ_r^{act} from 2 to 1.65 for 10 QWs. Obviously, the reduction of Γ_r^{act} for a higher number of QWs will severely limit the advantage of increased material gain.

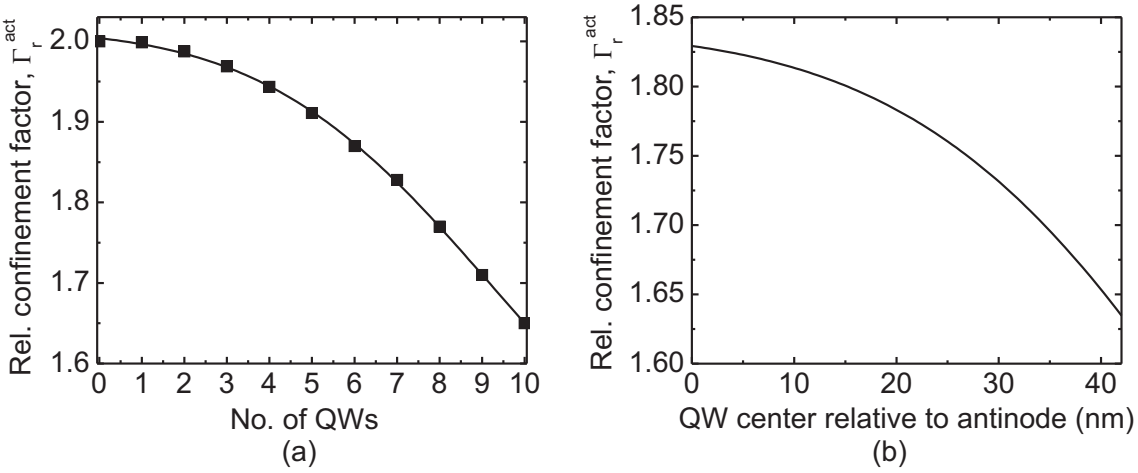

Fig. 3.3: *a) The relative confinement factor Γ_r^{act} as a function of number of quantum wells. Calculations are based on 10 nm QWs and 8 nm barriers used for 2.6 µm VCSELs and QWs are centered at an intensity maximum of the standing wave. b) The dependence of Γ_r^{act} on the displacement of QW center position with respect to the field antinode. Calculations are done for 7 QWs separated by barriers with the same thicknesses.*

Fig. 3.3 b) illustrates the variation of Γ_r^{act} with the displacement of QW center position relative to field antinode for 7 QWs. This case has to be considered as well in GaSb-based

VCSELs. Since GaSb-VCSELs requires twofold epitaxial growth and the total growth thickness of the epitaxial layers is approximately 14 µm for e.g. 2.6 µm VCSELs, the growth thickness inaccuracy comes into play. Furthermore, some inaccuracy on the material refractive indices and the device fabrication itself could misalign the QW center position with respect to the field antinode. For instance, the misalignment of 40 nm for the active region with 7 QWs will reduce the value of Γ_r^{act} from 1.83 to 1.64 as illustrated in Fig. 3.3 b). Thus the material average gain is reduced.

Let's assume, the active region into the field maximum, i.e. $\Gamma_r^{act} = 2$, threshold gain $g_{th} = 1000\,cm^{-1}$, total top and bottom mirror loss $\alpha_m = 0.3\% + 0.2\% = 0.5\%$, the effective cavity length $L_{eff} = 3.4\,\mu m$, and total internal loss $\alpha_i = 25\ cm^{-1} \times 3.4.10^{-4}\ cm = 0.85\%$. Eqn. 2.40 can be used to calculate the optimum number of QWs where round trip gain/loss is taken into account. Considering each quantum well thickness, $L_{QW} = 10\,nm$ yields N_{QW}^{opt} is equal to 6. So, for practical purposes, 7 QWs are used in the active region of 2.6 µm VCSEL structure.

3.1.2 High Reflectivity Mirror Design

One of the key issues in realizing low-threshold VCSELs is the design of mirrors with high-reflectivity on both sides of the gain region. In fact, the high reflective mirror should provide a reflectivity greater than 99% in order to keep losses low enough for the devices to reach threshold. Bragg mirror could be one of the choices in this case. Apart from Bragg mirror, one could also think of hybrid mirror [53]. Another high reflectivity mirror is high contrast grating (HCG) mirror where the gratings are made up of a subwavelength grating structure [54]. Note that, HCG mirror works with the principle of destructive interferences of modes within the structure. In GaSb-based BTJ VCSELs, only Bragg mirror is utilized on both sides of the active region so far.

In general, one should consider the following three issues for the mirror material while realizing a high-reflectivity Bragg mirror:

- refractive index contrast between the mirror materials with low and high refractive index should be as high as possible
- materials should have low absorption loss at the lasing wavelength
- materials' thermal conductivity should be as high as possible

These three issues can be fulfilled either by epitaxial or dielectric material.

3.1.2.1 GaSb/AlAsSb Bragg Mirror

Epitaxial mirror is realized with epitaxially-grown semiconductor alloys lattice-matched to a given substrate. For the (AlGaIn)(AsSb) material system, the index contrast between lattice-matched $AlAs_{0.08}Sb$ and GaSb is ≈ 0.6 at 2.6 µm which allows to provide a reflectivity of approximately 99.8% with only 24 layer pairs. The required number of layer pairs should be as low as possible in order to have a low number of defects and reproducible MBE growth of DBR.

Since the current will flow through the bottom epitaxial mirror in presented devices, the mirror materials are n-doped with Te-dopant which limit the maximum achievable reflectivity due to free-carrier absorption in doped layers. Not only optical absorption loss but also electrical and thermal issues should be considered while doing the epitaxial Bragg mirror design. Details of all design issues are extensively discussed in [55, 56].

3.1.2.2 *a*-Si Vs. *a*-Ge as Dielectric Mirror Material

Dielectric mirrors are key components in a number of optoelectronic devices, e.g. vertical-cavity surface-emitting lasers (VCSELs), low-threshold edge-emitting lasers, subwavelength ultrabroadband mirrors and modulators which require very high reflectivity ($R > 95\%$) with low optical losses. In fact, this type of mirrors, such as, distributed Bragg reflectors (DBRs) or Bragg mirrors are composed of stacking alternating thin layers of two different dielectric materials with high and low refractive index.

Among materials with low refractive indices, SiO_2 is a good choice since it provides almost negligible absorption and at the same time it has a refractive index of around 1.45 in the mid-infrared wavelength regime. Among conceivable materials with high refractive indices, *a*-Si and *a*-Ge are potential ones against SiO_2. When *a*-Si against SiO_2 is used in dielectric mirrors above 2 µm, one can obtain approximately $\Delta n \sim$2.0, since the refractive index of *a*-Si is about 3.5 for a photon energy of 0.57 eV. An even higher index contrast, $\Delta n \sim$ 2.9 can be achieved by using *a*-Ge against SiO_2 in this wavelength regime, because *a*-Ge shows a very high refractive index of approximately 4.4 below 0.6 eV. But when the optical absorption losses of these materials above 2 µm are considered, then *a*-Si is proved to be better. As a matter of fact, *a*-Ge introduces a larger insertion loss than *a*-Si that limits its use in devices based on transmission.

The optical characteristics of e-beam evaporated and non-hydrogenated *a*-Si and *a*-Ge are determined in the mid-infrared (MIR) wavelength regime. Then the comparison between these two materials for their use as dielectric mirrors is presented here. As a part of the investigation, these materials are at first evaporated by e-beam on quartz glasses and then reflection, transmission and photothermal deflection spectroscopy (PDS) measurements were carried out. Finally, the values of the refractive index and the absorption coefficient are extracted from these measurement data. Details of this analysis are presented in Chap. 5.

In order to check the measured absorption and refractive index value in the energy range of 0.24-0.8 eV, two test structures were prepared by evaporating 3 pairs *a*-Si/SiO_2 and in another one *a*-Ge/SiO_2 on top of GaSb-substrate. Fig. 3.4 shows the schematic view of each structure and the corresponding measured and simulated reflection spectra, where air is the incident medium. The reflection spectra were measured with a Bruker Vertex 70 FTIR spectrometer using extended InGaAs and LN-cooled InSb detectors. Despite of the strong optical losses of *a*-Ge but large index contrast of *a*-Ge/SiO_2, the calculated peak reflectivity of a 3 pair *a*-Ge/SiO_2 at $\lambda = 2.6$ µm is 99.2%, which is slightly lower than a 3 pair *a*-Si/SiO_2 DBR. Two parameters determine the reflectivity of a given mirror; these are transmission and absorptive losses. Transmission loss is often considered an more important parameter for the outcoupling mirror rather than reflectivity. When the

transmission through the mirror is considered at this equal reflectivity with 3 layer pairs, *a*-Si concedes 0.5% transmission loss, whereas *a*-Ge does 0.13%, hinting that *a*-Ge is governed by absorption loss which reduces the transmission loss.

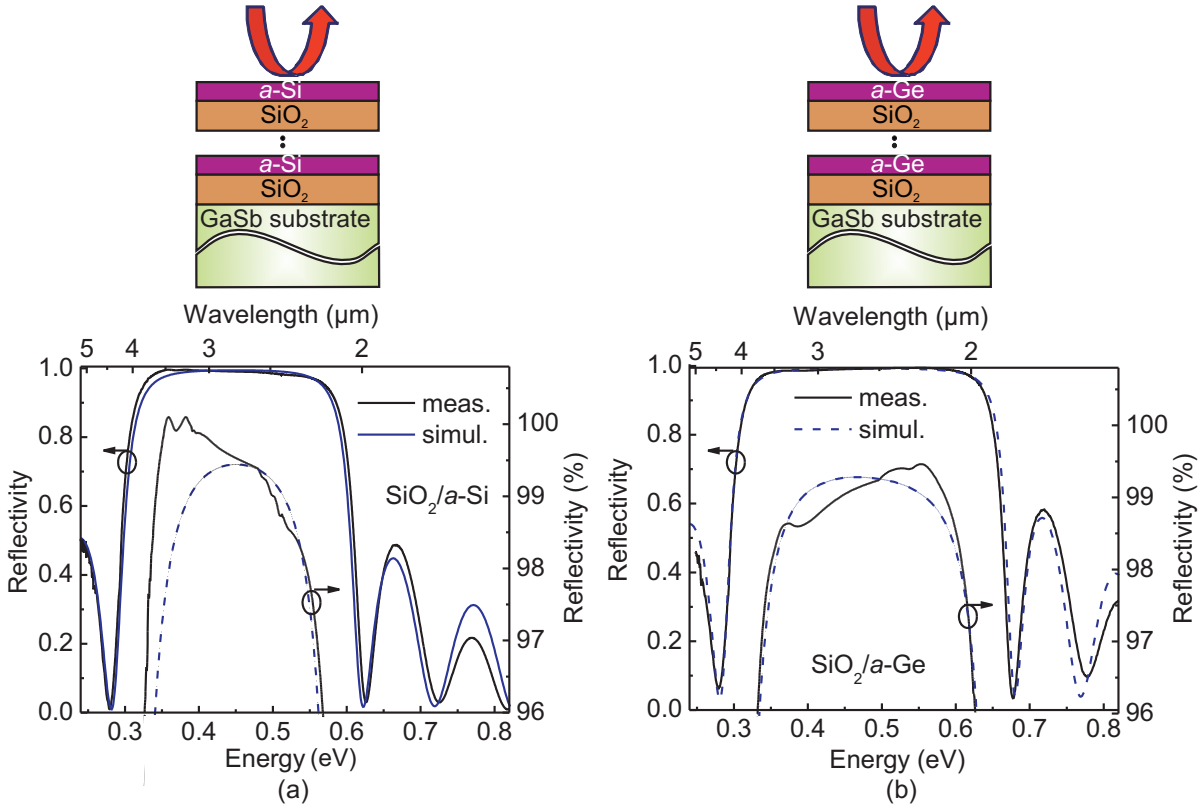

Fig. 3.4: *Reflectivity spectra of a 3 pair a) a-Si/SiO_2-DBR and b) a-Ge/SiO_2-DBR designed for maximum reflectivity at 2.6 µm. The simulation (dashed line) fits well to the measurement (solid line), hinting that the measured n and α values of these materials are accurate. The deviations close to the maximum are measurement artifacts and result from the combination of two curves measured with two different detectors. Note that test structures used for these measurements are shown above as well.*

Experimentally it has been found out that the value of absorption coefficient α for *a*-Ge above 2 µm remains more than one order of magnitude higher than *a*-Si. For example, at a wavelength of 2.7 µm, *a*-Ge exhibits $\alpha_{Ge} = 380\ cm^{-1}$ whereas $\alpha_{Si} = 28\ cm^{-1}$ in case of *a*-Si. Including absorption losses, the reflectivities of *a*-Si/SiO_2 and *a*-Ge/SiO_2 mirrors as a function of number of layer pairs are calculated as displayed in Fig. 3.5. The number of layers required by *a*-Ge/SiO_2 mirror to saturate the reflectivity of approximately 99.3% is only 3. The higher absorption loss of *a*-Ge limits to increase the reflectivity further. But *a*-Ge could be material of interest as a high index material to reach smaller reflectivity with fewer layer pairs.

Besides the optical properties, when the thermal conductivities of these two materials are considered, *a*-Si is proven to be better than *a*-Ge. The thermal conductivities of *a*-Si and

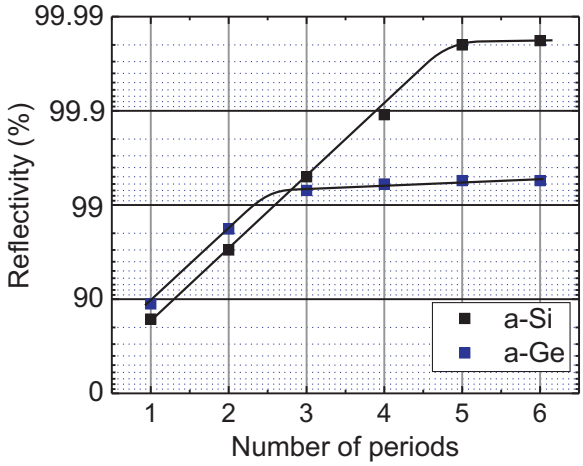

Fig. 3.5: *Reflectivity of a-Si/SiO_2 and a-Ge/SiO_2 mirror as a function of number of layer pairs.*

a-Ge are 1.8 and 0.5, respectively. Finally, the pros and cons of each material are tabulated in Tab. 3.2.

	real part, n	**imag. part, n**	**thermal cond., k**
a-Si	lower (×)	lower (✓)	higher (✓)
a-Ge	higher (✓)	higher (×)	lower (×)

Tab. 3.2: *Comparison between a-Si and a-Ge as dielectric mirror materials for GaSb-based BTJ VCSELs.*

3.1.3 Cavity Design for BTJ VCSELs

Given a finished active region and mirror design, the next task is to adjust the cavity mode has to the right wavelength and keep it controlled through two epitaxial growth steps. As known, the cavity mode wavelength should be located at the region of the highest mirror reflectivity to provide lowest threshold gain. This can be partially fulfilled by the right inner cavity length of the resonator. One of the important considerations in VCSEL design is the determination of inner cavity length L which is sandwiched by top and bottom DBR. Theoretically, nL should be integer multiple of $\lambda/2$ to fulfill the resonance condition of the emission wavelength λ.

Fig. 3.6 a) shows the standing wave pattern of the electric field intensity together with the refractive index profile of the GaSb-based VCSEL structure. Calculations are done with a simple 1D transfer matrix method [57]. As trade-offs among optical, electrical and thermal performance of the device, $nL = 3\lambda$ has been chosen for devices under study. A detailed discussion regarding this point is mentioned in [58, 59].

The following important design criteria can be identified in Fig. 3.6 b).

- Maxima of the electric field intensity are placed at both ends of the inner cavity of length L.

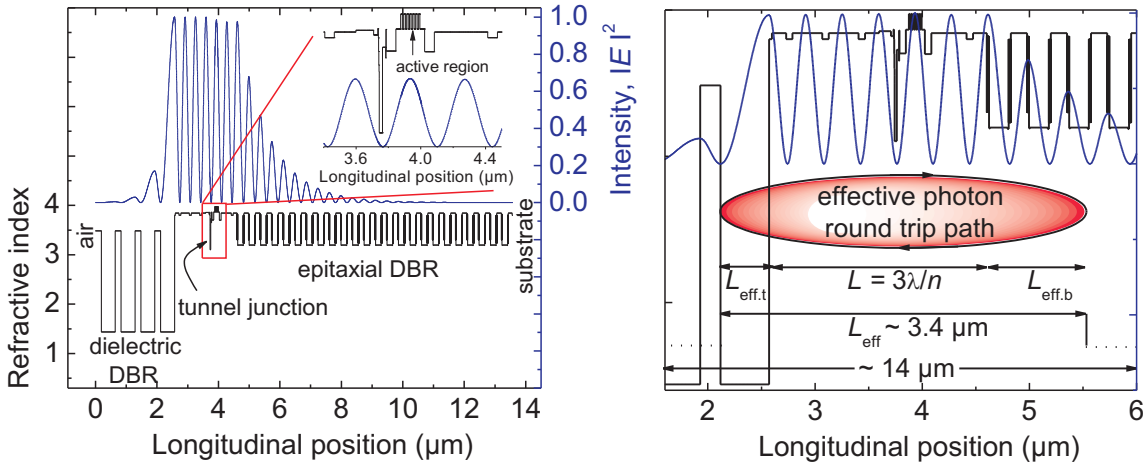

Fig. 3.6: *a) Standing wave pattern of the electric field intensity and refractive index profile in GaSb-based BTJ VCSELs in the longitudinal direction, where the center region of the structure containing the active region and tunnel junction is zoomed-in showing the active region and tunnel junction are placed in an antinode and node of the field, respectively. b) The effective cavity length for a 2.6 µm VCSEL.*

- The first layer of the bottom epitaxial and top dielectric mirror in Fig. 3.6 b), as seen from the inner cavity is of material with a lower refractive index than the adjacent material, GaSb.
- The effective cavity length of a 2.6 µm VCSEL can be calculated to 3.4 µm, where the field penetration depth in the bottom epitaxial mirror $L_{\mathrm{eff,b}} = 1\,\mu\mathrm{m}$ and in the top outcoupling dielectric mirror $L_{\mathrm{eff,oc}} = 0.4\,\mu\mathrm{m}$. Note that, since the FCA loss in the dielectric layers is negligible, the effective cavity length for the interaction between light and the absorbing medium is $\approx 3\,\mu\mathrm{m}$.
- The active region is placed in an antinode of the standing wave pattern so that optical gain in the active layer is efficiently used, while tunnel junction is placed in a node to minimize the optical FCA loss.
- 400 nm and 1 µm GaSb layer are used in the inner cavity by placing them below the active region and on top of tunnel junction, respectively. This makes the inner cavity thicker in GaSb-based BTJ VCSELs. The purpose of using these layers is to dissipate the heat from the active region while ensuring lateral current spreading in the device.
- These current and heat spreading layers are modulation doped in order to obtain a reasonably good electrical and optical performance. High doped layers are placed at the node of the standing wave pattern to minimize the FCA loss as shown in Fig. 3.6 b).

3.1.4 Gain-Cavity Tuning

The calculated wavelength of the quantum well gain section employed in 2.6 µm VCSELs has been found at 2780 nm (≈446 meV) as already mentioned. But experimentally the PL peak is found at 2760 nm. Note that such PL test structure was not subjected to any

heat treatment procedure. So, a negligible error of 3 meV is seen between the experiment and the calculation done in nextnano^{++} [60]. But InGaAsSb-based active region see the commonly known blueshift effect [61] which leads to a shift of the PL peak from 2760 nm to 2545 nm in the PL test sample as shown in Fig. 3.2. Such blueshift appears in the active region due to the annealing process carried out at 430°C for two hours.

During the VCSEL fabrication, specially after the tunnel junction structuring, the sample is exposed to 430°C as a growth temperature for the epitaxial overgrown layers. Before the overgrowth, the sample is cleaned by atomic hydrogen (atom-H). The reason of such cleaning using Atom-H is to remove the contaminations and remaining oxides more effectively. In fact, the cleaning procedure was carried out at a temperature of 80°C for 30 min. In this step, C-related contaminations and Sb-Oxides are almost completely removed, building volatile complexes with H-atoms. It was followed by a heating at 400°C for 30 min to remove the Ga-oxides as well. It should be noted that the high-temperature oxide desorption step before the overgrowth was not applied in 2.6 µm VCSEL sample so that the known blueshift of the active region can be minimized in the structure.

The PL peak 2545 nm (≈487 meV) is negatively detuned to the cavity dip at 2.6 µm (≈476 meV) with a gain-to-cavity mode offset of 55 nm (≈ 9 meV). As a common design rule, in order to have a better matching of the material peak gain with the cavity dip at RT under laser operating condition, the gain peak should be pre-detuned relative to the cavity resonance. Apart from these active region heating and blueshift effects, many body effetcs like the increase of the bandgap due to a well-known Burstein-Moss band-filling effect and the reduction of the bandgap due to the so-called bandgap narrowing effect by the coulombic attraction of the carriers play important roles in a VCSEL before threshold [62]. This clearly indicates that optimum gain-mode offset is one of the critical design parameters in GaSb-based VCSELs.

3.1.5 Tunnel Junction

In GaSb-based VCSELs, buried tunnel junction (BTJ) is one of the most important device components which offers the possibility to introduce strong lateral waveguiding, i.e. photon confinement in the device. In order to obtain this benefit, it is necessary to make sure that the tunnel junction (TJ) is properly designed and successfully implemented in the devices since several loss mechanisms, for instance, absorption loss and diffraction loss are related to TJ. Moreover, the strong waveguiding induced by the BTJ will lead to a multimode operation even in small sized devices. As a part of the optical design for tunnel junction, the following issues should be considered with high importance:

3.1.5.1 Absorption Loss

In the presented devices, TJ consists of highly doped n^+-InAsSb/p^+-GaSb layers to achieve efficient quantum tunneling. However, such high doping ($N_A = 2\,x\,10^{19}\,cm^{-3}$ and $N_D = 2\,x\,10^{19}\,cm^{-3}$) in these layers may introduce a significant amount of free carrier absorption (FCA) loss degrading the device performance. So, it is of great importance to minimize the optical loss, e.g. FCA introduced by these tunnel junction layers. In fact, the tunnel junction should be integrated into the device in a way that all electrical benefits (discussed

in Sect. 3.2.2) can be obtained while minimizing the FCA loss as much as possible.

The best way to reduce the FCA loss is to place these layers at the node of the optical standing wave in the cavity. Thus the overlap between these layers and regions of high electric field is minimized which results in a reduced FCA loss. Due to the high doping in these layers, their thicknesses could also be a crtical design issue. In devices under study, the thicknesses of these layers were 20 nm each which could be reduced further, leading to an improved device performance by minimizing the optical loss and at the same time the amount of optical waveguiding (discussed in Sect. 3.1.5.2).

For a tunnel juction, the single pass FCA loss can be calculated by [63]

$$\alpha_{\mathrm{BTJ}} = 2 - e^{-\alpha_{\mathrm{n}} L_n \Gamma_r^n} - e^{-\alpha_{\mathrm{p}} L_p \Gamma_r^p} \tag{3.1}$$

where L_n, L_p are the thicknesses and α_n , α_p are the FCA losses in n- and p- doped layers, respectively and $\Gamma_{\mathrm{r}}^{n,p}$ is the relative confinement factor of n- and p-doped layers in the tunnel junction. It is clear that $\Gamma_{\mathrm{r}}^{n,p}$ and L should be reduced in order to minimize the single pass FCA loss in these high doped layers. As shown in Fig. 3.7, the interface of n-InAsSb/p-GaSb layers is exactly placed at the node of the optical standing wave in order to minimize $\Gamma_{\mathrm{r}}^{n,p}$ which can be calculated using Eqn. 2.15 with $N_{\mathrm{QW}} = 1$ and $L_{\mathrm{QW}} = L_n$ or L_p . But it has been found that the placement of the n-InAsSb/p-GaSb interface at the node of the optical standing wave is not an optimum design because of the unequal losses in these two layers. For instance, the optimum placement of the tunnel junction layers should be shifted 7 nm toward the n-InAsSb layer due to the higher losses within this layer compared to p-GaSb for the design of 2.3 µm VCSELs [58].

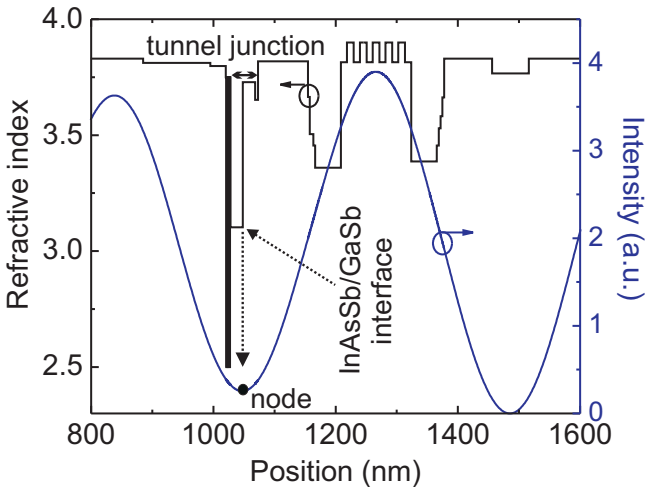

Fig. 3.7: *Electric field intensity and refractive index profile in BTJ VCSELs, showing the placement of the tunnel junction at the node of the optical standing wave.*

It should be noted that the very long emission wavelength facilitates the optical design in terms of the minimization of the FCA losses in tunnel junction layers. This is particularly due to the lateral extension of the optical standing wave in the cavity. For instance, while extending the VCSEL emission wavelength from 2.6 µm to 3.3 µm, the FCA losses will be

higher at 3.3 µm VCSELs since $\alpha \propto \lambda^2$. But considering Γ_r, the situation reverses since $\Gamma_r \propto \lambda^{-3}$. Ultimately, the combined effect will improve the situation, i.e. the FCA loss will decrease despite of the higher losses at a longer wavelength. In other words, the longer wavelength makes the optical design easier to place the highly absorbing tunnel junction layers in a minimum of the electrical field.

3.1.5.2 Waveguiding

Despite of the inherent single longitudinal mode behavior, lasing of higher order transverse modes is a common phenomenon in VCSELs with even relatively small active diameters. In oxide-apertured index-guided GaAs-based VCSELs, single-mode emission is observed only in very small devices of typically less than 4 µm diameter [64]. In long-wavelength InP-based BTJ VCSELs with molecular beam epitaxy (MBE) regrowth, this transverse single-mode operation has been found for devices with diameter of 6 µm [54], even though the index guiding of the device is stronger than in GaAs-based VCSEL structures. This is mainly due to the fact that the maximum transverse device dimensions approximately scale with the wavelength. So, very long wavelength VCSELs above 2 µm will get this benefit even more.

An theoretical analysis of transverse mode characteristics for index-guided GaSb-VCSELs will be presented in this section. This index-guiding is obtained by an effective refractive index step due to the presence of a buried tunnel junction (BTJ) concept. As a matter of fact, achieving a single transverse mode operation from GaSb-based BTJ VCSELs with even a small aperture diameter is a challenging task due to the presence of a strong index guiding behavior. Here we have experimentally presented how the index guiding can be reduced in the device and such reduction lead to an improvement in terms of a transverse single mode operation from large-area devices.

- **Transverse index guiding in BTJ VCSELs**
  The index-guiding in BTJ VCSELs mainly arises from a longer cavity in the central region with a tunnel junction aperture rather than in the perimeter. Consequently, a radial index step Δn_{eff} due to the step height (as shown in Fig. 3.8 by a dashed red-colored circle) is formed in the tunnel junction region. Note that the step from the tunnel junction propagates through the entire structure which is clearly seen after the regrowth in MBE. Thus, the step at the interface of the top epitaxially-grown GaSb layer and the e-beam evaporated dielectric DBR and also on top of the dielectric DBR is formed in the device structure as shown in Fig. 3.8.

  The index-guiding properties can be investigated by using a simple effective index model developed by Hadley [65]. In fact, the laser resonator can be described similar to a step index glass fiber by using the effective indices in the central part, n_C and in the outer part, $n_{Cl} = n_C - \Delta n_{\text{eff}}$. A theoretical formula relating this induced built-in refractive index step to a shift of the resonator wavelength $\Delta\lambda$ can be described by [65]

$$\frac{\Delta n_{\text{eff}}}{n_C} = \frac{\Delta\lambda}{\lambda_C} = \frac{\lambda_C - \lambda_{Cl}}{\lambda_C} \tag{3.2}$$

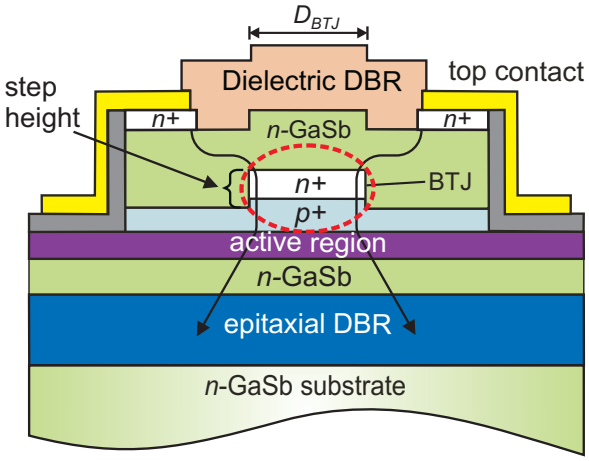

Fig. 3.8: *Schematic cross-sectional view of the GaSb-based VCSEL structure with BTJ. The current path is shown.*

where λ_C and λ_{Cl} are the resonance wavelengths in the area with tunnel junction and the area without tunnel junction of the VCSEL, respectively. These resonance wavelengths can be evaluated by means of the one dimensional (1D) transfer matrix method [57] and the effective refractive index in the tunnel junction region can be approximated by computing the longitudinally field weighted average refractive index [42]

$$n_C = \sqrt{\frac{\int n^2(z)|E(z)|^2\,\mathrm{d}z}{|E(z)|^2}} \tag{3.3}$$

where $|E(z)|$ is the amplitude of the longitudinal standing wave field, *n(z)* is the refractive index of each epitaxial layer in the longitudinal direction and the integration is performed from the substrate to the outer boundary of dielectric DBR.
The magnified view of the dotted red-circle in Fig. 3.8 is displayed in Fig. 3.9 where one can see that the step height is not only due to the n^+-InAsSb layer itself, but also grading layer and *n*-GaSb layer.

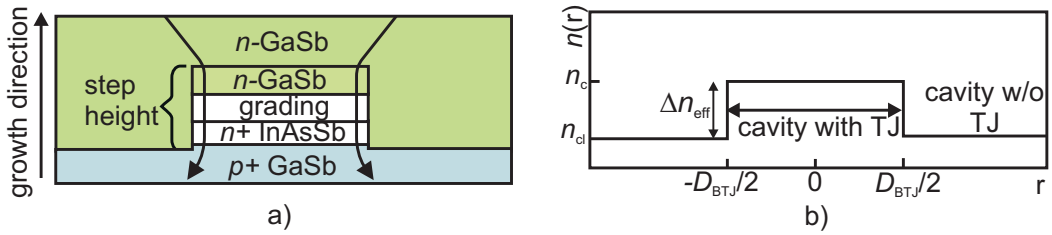

Fig. 3.9: *a) Magnified view (dashed red-colored circle in Fig. 3.8) of the tunnel junction region with current flow in GaSb-based BTJ VCSELs. b) The index guiding, caused by the step of the BTJ, is illustrated here. Cavity model with step refractive index profile n(r).*

- **Amount of index guiding**
  The lateral definition of the BTJ is accomplished by etching off the upper n^+-InAsSb, grading and a thin n-GaSb layer and covering the whole structure by an n-GaSb layer in a second epitaxial run. Finally, the total step height in BTJ VCSELs is in the range of 50-70 nm, where the contributions of the above-mentioned n^+-InAsSb, grading and thin n-GaSb layer to the total step height is 20 nm, 10-20 nm and 20-30 nm, respectively. In fact, this step height referring to the physical length difference between etched and non-etched part is rather high since grading and top n-GaSb layer must be included along with tunnel junction layer. It is obvious that the higher the etch depth in the tunnel junction region, i.e. the higher the step height, the higher the index guiding in the device. Fig. 3.10 shows the degree of the index guiding against the etch depth of the tunnel junction, where n_{eff} is calculated by Eqn. 3.2 and 3.3. Note that, throughout the entire discussion of this study, the effective refractive index

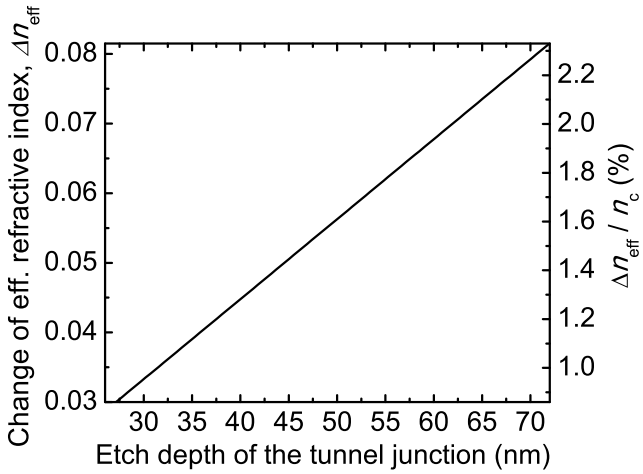

Fig. 3.10: *The change of the effective refractive index Δn_{eff} as a function of the etch depth of the tunnel junction.*

step Δn_{eff} caused by the BTJ has been assumed to be the prime reason for index-guiding in the device. For the devices presented here, we find constant wavelength spacing between transverse modes independent of driving current hinting that thermal guiding caused by local heating (the refractive index increases with increasing temperature) can be neglected [66]. Antiguiding caused by carrier gradients (high carrier concentrations decrease the refractive index) is also not considered to be a strong effect since the waveguiding property of a strong index-guided VCSEL is not significantly affected by temporal changes in the carrier density [67]. It should also be mentioned that the presented single-mode VCSELs operate in single-mode over the entire operating range.

- **VCSEL Design with regard to index guiding**
  In this section, the design of 2.3 and 2.6 µm VCSELs with two different degrees of index-guiding is briefly described. In 2.3 µm VCSELs, the relative change of the effective indices calculates to $\Delta n_{\mathrm{eff}}/n_{\mathrm{C}} \approx 2.4\%$, whereas, in 2.6 µm VCSELs, this value amounts to $\Delta n_{\mathrm{eff}}/n_{\mathrm{C}} \approx 1.7\%$, indicating a strong index guiding. This will lead to

multimode behavior even for small aperture diameters.

For 2.3 µm VCSELs, the higher effective index step is due to the use of thick grading layers in the cavity. The thinner grading layer was used in 2.6 µm VCSELs which results in a reduced step height. Fig. 3.11 illustrates the band diagram of both VCSELs only at the tunnel junction region, specifically, in the region of the dashed red-colored circle of Fig. 3.8. It should be noted that the tunnel junction is located at the node of the standing wave pattern in BTJ VCSELs in order to reduce the optical absorption loss which also helps in obtaining a reduced index-guiding in the device. The main

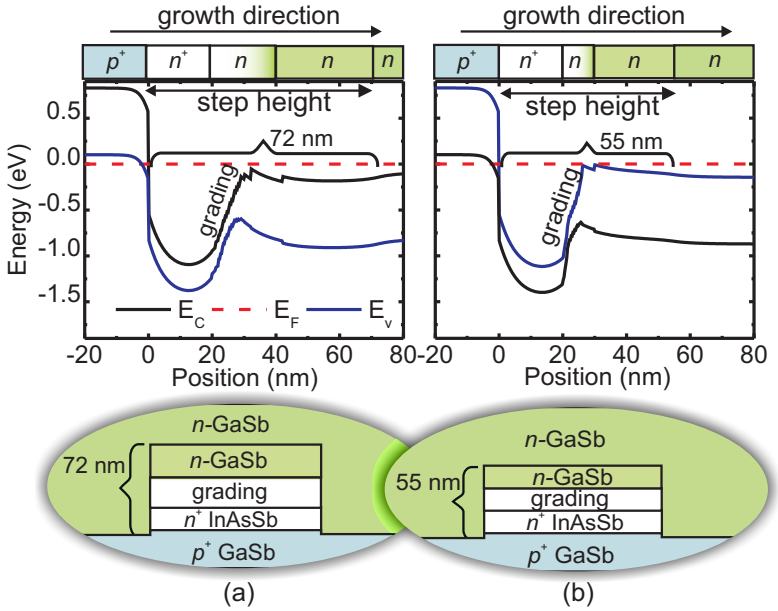

Fig. 3.11: *Band diagram of tunnel junction regions in BTJ VCSELs for the emission wavelength of (a) 2.3 µm and (b) 2.6 µm . Both band diagrams have been calculated with SimWindows 1.5.0 [68] using the material parameters from [69].*

reason for using grading layers in the cavity is to reduce electrical resistivity at the InAsSb/GaSb heterointerface. Importantly, the electrical performance in terms of series resistance of a 10 nm and 20 nm thick grading layer was found to be identical. But the use of such a 20 nm thick grading layer in the BTJ results in an increased index-guiding which has been observed in 2.3 µm VCSELs. Thus a thinner grading layer was introduced in 2.6 µm VCSELs in order to obtain a reduced index-guiding. The same reasoning also holds for the thickness of *n*-GaSb layer.

3.1.5.3 Diffraction Loss

In most VCSELs, the cavity propagation loss is mainly due to the outcoupling through Bragg mirrors and optical absorption in the semiconductor material. In addition to these two loss types, there is the diffraction loss, which is the excess loss caused by the fact that light does not propagate only in the longitudinal direction. Like all beams of light, the cavity field has a tendency to spread, i.e. to propagate also in the radial direction, which causes a radial leakage of radiation along the entire length of the cavity. For most VCSELs,

this leakage, i.e. the diffraction loss is small, since the typical VCSEL cavity is short in the longitudinal direction and relatively wide in the lateral direction. Thus, for most VCSELs the diffraction loss can be neglected. However, because of the BTJ and the resulting change in the topology of all layers above it, the intracavity field in the GaSb-based BTJ VCSEL experiences a strongly varying refractive index also in the lateral direction. This lateral disturbance results in an enhanced spreading of the light, thus considerably increasing the diffraction loss [70].

A direct measurement of the diffraction loss is very difficult. On the other hand, since diffraction is caused by the spatially varying real part of the refractive index, without being much influenced by e.g. the QW gain or material absorption, it can be estimated with fair accuracy by numerical simulation, provided that the numerical model of the complicated VCSEL structure does not overwhelm the computer resources. Therefore, Gustavsson et al. [70] implemented a numerical method for calculating the intracavity field, and the radial field leakage, that is efficient in terms of computer memory. It is a hybrid method using a 3D transfer matrix method (TMM) [71] for the VCSEL structure beneath the BTJ, where there is no lateral variation in the refractive index, and a beam propagation method (BPM) [72] for the BTJ and the structure above it.

In fact, such loss mechanism in the device can be minimized by reducing the step height induced by the BTJ. This has already been proven by devices under study where the step height has been reduced from 72 nm to 52 nm by decreasing the grading layer and cap GaSb layer thickness whose outcome will be discussed in Chap. 6. However, this reduced step height still results in an significant amount of loss which deteriorates the device performance. Further reduction of the step height thickness by decreasing the grading layer and the cap layer thickness seems to be challenging. Since such configuration will affect the device electrical properties. Besides, MBE regrowth also does not help out in planarizing the surface so that in the top DBR there would be a very little change of the refractive index in the radial direction. For instance, the index guiding in InP-based BTJ VCSELs caused by the step of the BTJ is influenced by the regrowth technique. Here this step is smoothed out by the MOVPE regrowth utilizing its planarization properties. The physics behind this planarization mechanism in MOVPE regrowth is the higher migration length of the deposited atoms resulting from a high growth temperature.

In order to reduce the diffraction loss, tunnel junction step can be smoothed out a bit on top of the device structure. Such modification can be brought at the interface of the overgrown GaSb layer and the top DBR which has been marked by a red-dotted ellipse as displayed in Fig. 3.12. This can be realized by a selective etching of approximately 30-35 nm GaSb layer after the overgrowth when the BTJ pillar height is of 50-55 nm. This might result in a reduced diffraction loss in our devices since now the top deposited dielectric mirror obtains a less abrupt change of the refractive index in the radial direction. This has already been confirmed by the numerical simulation done at Chalmers Univ. Tech., Sweden. Note that the complete removal of the BTJ pillar will yield a gain-guided device since a lower effective index appears (due to a low refractive index of InAsSb) at the center compared to the outer part of the device.

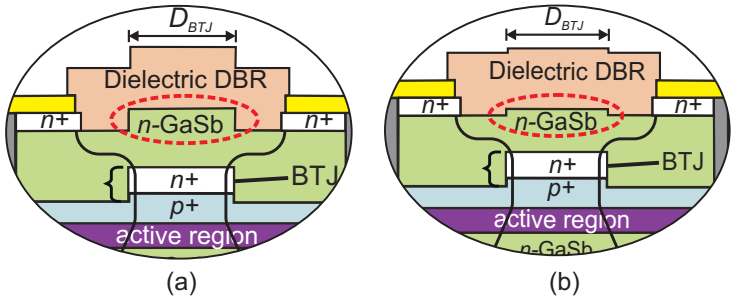

Fig. 3.12: *a) Schematic of the top part of the standard GaSb-based VCSEL structure, b) modified structure with a reduced tunnel junction step height.*

3.1.5.4 Transverse Mode Control

- **Waveguiding Ring**
  A transverse single-mode operation from large-area devices is always beneficial since they promise low differential series and thermal resistance, long lifetime due to low current densities and high output power at small divergence angles. In order to enhance the single-mode output power by suppressing higher order modes, an annular structure made of *a*-Si around the BTJ can be formed as shown in Fig. 3.13. The material has to be deposited around the BTJ in a way so that the flat refractive index can be obtained. Such structure can be named as waveguiding ring. The key concept is to broaden the optical field by utilizing such ring structure while maintaining the same lateral current confinement by BTJ. This broadened optical field will favor the fundamental mode which experiences a higher gain compared to the higher order modes. In other words, the gain difference between the fundamental and higher order mode will be higher which also helps in improving the single-mode output power.

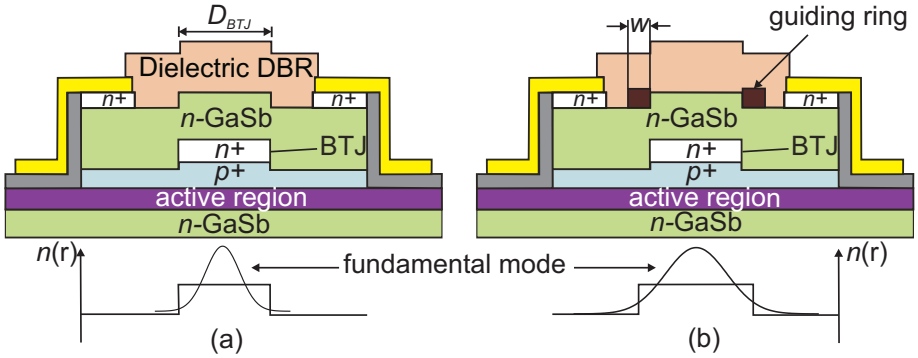

Fig. 3.13: *GaSb-based BTJ VCSEL a) without waveguiding ring, b) with ring structure of width w, buried in the top dielectric DBR. The fundamental mode intensity and the effective refractive index profile induced by the BTJ.*

Note that the ring shaped structure should have a certain thickness in order to achieve the desired waveguiding. If *a*-Si is used to form such structure, then the thickness of the evaporated material should be somewhat larger than the thickness that corresponds to the same optical thickness of the BTJ. This will lead to a flat effective

refractive index in the resonator.

- **Inverted Surface Relief**
  The so-called inverted surface relief (ISR) technique [73] can be applied to the devices in order to select only the single fundamental mode and suppress higher order modes. In this method, an annular deposition of additional quarter-wave thick antiphase *a*-Si layer on top of the dielectric Bragg mirror will lower the reflectivity for higher order modes. The resulting differences in threshold gain then strongly favor the fundamental mode. Compared to other mode filtering methods, the ISR technique involves a minor modification to the VCSEL processing since it offers a relatively less fabrication complexity with respect to the requirement of less precise deposited layer thickness. Such circular ring-shaped relief, intended for fundamental mode operation, was precisely defined using a standard photolithography and an extra $\lambda/4$ thick e-beam-evaporated *a*-Si was selectively added to the top dielectric mirror to provide an anti-phase reflection from the semiconductor-air interface as displayed in Fig. 3.14. Thus the modal threshold gain of the device was spatially changed by selective deposition of this anti-reflection coating.

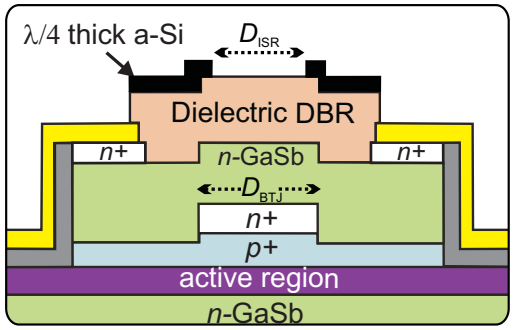

Fig. 3.14: *Schematic cross-sectional view of the GaSb-based VCSEL structure with inverted surface relief in the top mirror.*

The optimum diameter of the surface relief, D_{ISR} should be in the range of 60%-80% of the diameter of the BTJ, D_{BTJ}. Using an electro-thermal optical model, we have also simulated the modally-resolved output power versus current characteristics for the VCSEL with and without a surface relief for single fundamental mode control. The results show that the relatively large diffraction loss in these devices (particularly for higher order modes) gives rise to strong fundamental mode selection, indicating that a surface relief is redundant in this aspect for devices with a BTJ diameter smaller than 8 µm. However, the results show that the surface relief can be used to efficiently boost the maximum output power [74].

3.2 Electrical Design

In this section, electrical design issues for GaSb-based BTJ VCSELs will be discussed which is of significant importance for superior device performance. A large portion of the work in this dissertation focuses on the optimization of the electrical properties in the device. This specially includes the realization of a low resistive metal semiconductor ohmic *p*-side

contact, low resistive tunnel junction, efficient current confinement and good lateral current spreading. The characteristics of these several device components will be discussed now.

3.2.1 Top p-side Ohmic Contact on n-InAsSb

For the successful operation of such devices, high quality metal-semiconductor ohmic contacts with low specific contact resistivities (ρ_c) are important. But, the GaSb material system inherently has several problems which make the formation of ohmic contacts difficult. For instance, this material system is very reactive to the atmospheric oxygen or water which promotes the rapid formation of native oxides on the surface [75]. Besides, particularly in n-type GaSb, the problems of Fermi level pinning in the GaSb valence band [76] (which is, in fact, beneficial for ohmic contacts to p-type GaSb) and the low doping limit (2.5×10^{18} cm^3) for the commonly used Te dopant [77] impede to obtain high-quality ohmic contacts.

To date, the lowest value reported for contact resistances of unannealed ohmic contacts on n-GaSb is of the order of $10^{-4}\ \Omega\,\mathrm{cm}^2$ or even higher. Few groups, for instance, Vogt et al. [78], Yang et al. [79] and Robinson et al. [80] formed ohmic contacts on n-GaSb with low contact resistances on the order of $10^{-6}\ \Omega\,\mathrm{cm}^2$, but they applied high temperature (300°C-400°C) annealing steps on their alloy contacts. However, high temperature annealing may cause dopant diffusion and even it might affect the active regions [81]. Therefore, this work considers a low bandgap highly doped material to develop a low-resistive unannealed ohmic contact.

As a contact layer, n-type $InAs_{0.91}Sb$, a low bandgap material ($E_g = 0.296\,\mathrm{eV}$) and lattice-matched to GaSb ($E_g = 0.72\,\mathrm{eV}$) can be used. The use of this additional contact layer where the ohmic contacts will be formed on overcomes the above-mentioned problems. Because, at the surface of this material, the Fermi level is pinned near the conduction band [82] and it can be highly doped up to $1 \times 10^{20}\,\mathrm{cm}^3$ by using Te as a dopant [81]. In fact, high doping is necessary for the ohmic contacts in order to make the depletion region at the metal-semiconductor interface thin enough to enable carrier tunneling [83]. This is displayed in Fig. 3.15 a) by the band diagram of the metal, the highly n-doped contact layer and the buffer layer underneath. The band structure was calculated using SimWindows (version 1.5.0) [68].

Lauer et al. [84] demonstrated Ti/Pt/Au based contacts on the same contact layer using sputter etching in Ar+ plasma. They found the resistivities as low as $5.1 \times 10^{-6}\,\Omega\,\mathrm{cm}^2$, but this method involved the ion-induced damage of the contact layer surface during the longer sputter etching process. Obviously, one has to be extremely careful in this method in order to minimize this surface damage by properly controlling the parameters like self-bias DC voltage, applied high voltage, flow of Ar gases, sputter etching time which can make the contact surface oxide free and smooth prior to metal deposition. Small changes of these optimized parameters may lead to a bad ohmic contact. Moreover, a low resistance, $2.4 \times 10^{-8}\,\Omega\,\mathrm{cm}^2$ unannealed ohmic contact on n-type $InAs_{0.66}Sb$ has been developed by Champlain et al. [85] which is highly strained to GaSb.

An unannealed ohmic contact with low contact resistivity using a highly Te-doped n^+-

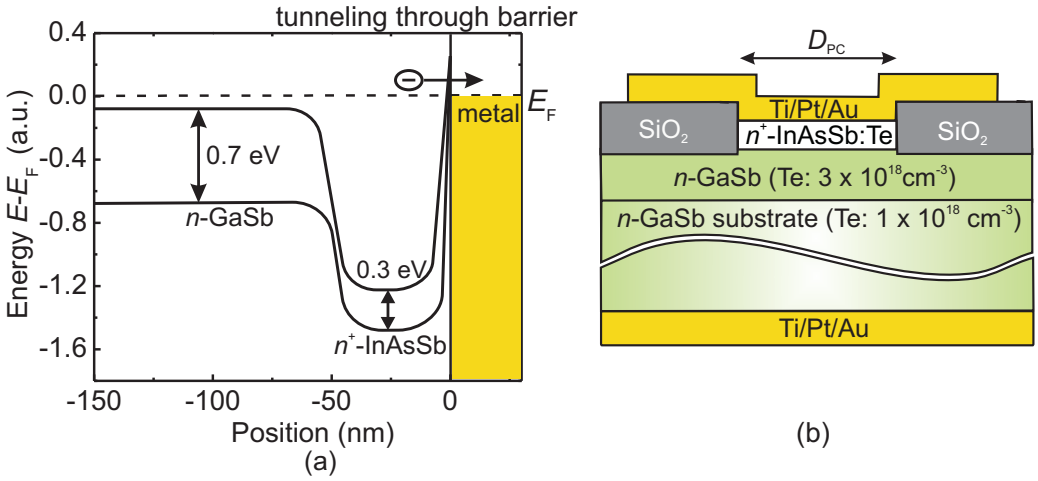

Fig. 3.15: *a) Band diagram of metal/n^+-InAsSb/n-GaSb. The dashed line indicates the Fermi level. The Schottky barrier at the metal-semiconductor interface is very thin which enhances the tunneling mechanism, b) Schematic cross-section of circular contact test devices. The diameter of the device is denoted by D_{pc}.*

InAsSb contact layer lattice-matched to GaSb will be mentioned here. This configuration is suitable for GaSb-based devices, such as VCSELs for wavelengths above 2 µm which have been demonstrated recently [27, 32, 33]. The surface preparation procedure based on a significantly simplified wet chemical treatment prior to metalization is also reported here.

The test samples used in this study consist of Te-doped n-GaSb substrate with doping concentration and resistivity of $1 \times 10^{18}\,\mathrm{cm}^{-3}$ and $0.0024\,\Omega\,\mathrm{cm}$, respectively, followed by a 500 nm thick Te-doped ($3 \times 10^{18}\,\mathrm{cm}^{-3}$) n-GaSb buffer layer and finally a 50 nm thick also Te-doped ($1 \times 10^{20}\,\mathrm{cm}^{-3}$) $n^+ - \mathrm{InAs_{0.91}Sb}$ contact layer. All the layers were grown by conventional solid-source molecular beam epitaxy (MBE) where As_2 and Sb_2 were generated by valved cracker cells. For Te doping, Ga_2Te_2 was used.

After the growth, circular mesas with 5 µm - 28 µm diameter were defined using standard UV lithography and subsequent citric acid-based etching by which the topmost InAsSb contact layer and a few nanometers of the GaSb buffer layer were removed. Then the mesas were covered with 150 nm of sputtered SiO_2 as a passivation layer. This layer was removed from the top of the mesas by a lift-off process to form circular contact openings. Before the metalization step, sulfur-based surface preparation procedure was applied since it is known that highly reactive Sb-based materials, such as our topmost contact layer, n-InAsSb, get oxidized very quickly in the atmosphere. Taking this into account, a conventional wet chemical etching step e.g. 18.5% HCl dipping for 30 s was employed to remove the surface oxides and then for preventing the further formation of oxides, the samples were rinsed with aqueous $(NH_4)_2S$ solution (with pH = 9.5) at room temperature. Afterwards the samples were blown dry with N_2 and promptly loaded into the electron beam metalization chamber. At a base pressure of 10^{-6} mbar and under the control of a thickness monitor, Ti/Pt/Au were sequentially evaporated. This surface preparation method fits quite well with the investigation done by Robinson et al. [80] where they formed In-bearing ohmic

contacts on n-GaSb.

The evaporated metal thicknesses for the top and backside contacts were 3/40/250 nm and 20/40/100 nm (Ti/Pt/Au) respectively. After the metal deposition, the contact pads were structured by metalization lift-off process. The final test structure is shown schematically in Fig. 3.15 b) where the diameter of the point contact is denoted by D_{pc}. The current-voltage-current density *(I-V-J)* characteristics of the point contacts with different diameters were measured in a four-point probe measurement system. The contact resistivities (ρ_{c}) were then deduced by the experimental method described in [86] where the current spreading under the mesa has been included. To investigate the effect of annealing on the contact resistance, several samples were additionally annealed at 350°C for 90 s in a rapid thermal annealing (RTA) furnace under flows of 4 slm of N_2 and 1 slm of H_2.

In order to see the influence of the sulfidation on the contact resistance, one sample was processed by only conventional HCl dipping without any sulfide treatment. As shown in Fig. 3.16, these test structures exhibit non-linear I-V characteristics with high contact resistivities of $1.2 \times 10^{-4}\,\Omega\,\mathrm{cm}^2$. In contrast, all the test devices processed by HCl dip followed by the sulfide dip exhibit good ohmic behavior as shown in Fig. 3.16, solid curve. Measured devices exhibit such ohmic behavior over a very high current density range of $\pm 70\,\mathrm{kA/cm}^2$ which is an adequate value for the operation of GaSb based VCSELs above the threshold current. In this way, the contact yielded a minimum specific contact resistance value of $5.6 \times 10^{-6}\,\Omega\,\mathrm{cm}^2$ without any annealing.

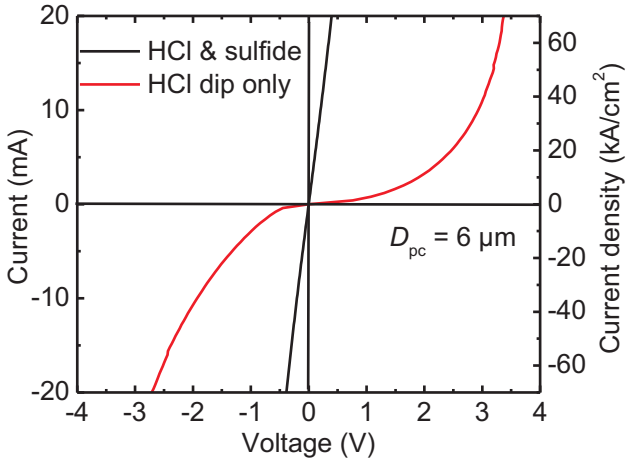

Fig. 3.16: *I-V-J characteristics of the point contacts without annealing.*

This striking difference might be due to a residual oxide layer at the metal semiconductor surface of the conventional HCl-dipped sample [75]. On the other hand, it is expected that by the sulfide passivation process, the dangling bonds at the contact surface are terminated in the form of S-In, S-As and S-Sb [87], which leads to a reduced ohmic contact since it allows the intimate contact between the metal and semiconductor.

Another pronounced feature which needs to be addressed is the annealing effect on the contact resistance. According to our investigation, annealing has a strong influence on the backside n-contact and results in lowering the contact resistivity. However, the current

spreads out in the 500 µm thick substrate and therefore the influence of the bottom contact of the test structure is negligible.

To obtain the optimum surface passivation time, one quarter GaSb wafer was splitted into six pieces where all the processing steps up to the metalization lithography were into the alkali 3.5% $(NH_4)_2S$ (pH = 9.5) at room temperature by varying the passivation time. The results are illustrated in Fig. 3.17 a) showing that the contact resistivity decreases with time up to 40 s and then rises again. The increase of contact resistance with time can be due to the thicker sulfide layer formed during the passivation which prohibits the intimate contact between metal and semiconductor. On the other hand, samples with very low passivation time, e.g. 4, 20 and 30 s, also shows higher contact resistance. As a possible reason, the reaction time between semiconductor surface and sulfide solution to replace the oxygen atoms by sulfur atoms at the semiconductor surface might not be sufficient making the surface sensitive to further oxidation by ambient air. In contrast to these findings, Robinson et al. [80] found a good ohmic contact to *n*-GaSb using a very short sulfide passivation time, i.e. 5 s.

In addition, the effect of the concentration of the $(NH_4)_2S$ solution on the contact resistance were investigated as displayed in Fig. 3.17 b) showing that the contact resistance increases with the concentration above 3% $(NH_4)_2S$. Apparently, the thick sulfide layer formed following passivation is not favorable when an ohmic contact is desired. Probably, the thick sulfide layer gets formed at the metal-semiconductor surface with the higher concentration causing the higher contact resistance. This is also in good agreement with the result of Robinson et al. [75]. Thus, by using 2.9% $(NH_4)_2S$ for 40 s as optimum sulfide treatment time, minimum contact resistivity values of approximately $5.6 \times 10^{-6}\,\Omega\,\mathrm{cm}^2$ were found without any annealing and it improves to $3.7 \times 10^{-6}\,\Omega\,\mathrm{cm}^2$ after annealing at 350 °C for 90 s.

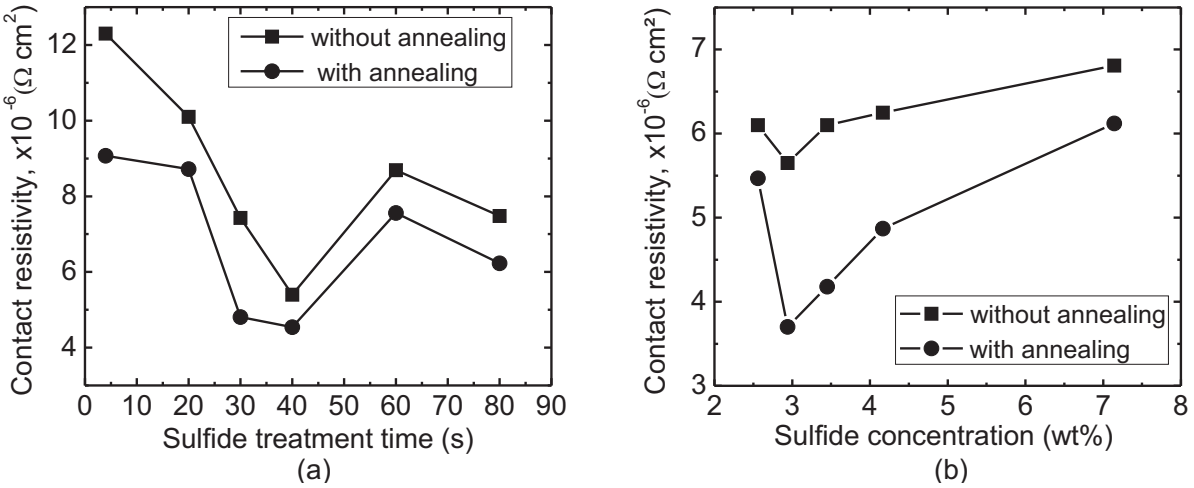

Fig. 3.17: *a) Contact resistivities with varying sulfide treatment time at constant 3.5% $(NH_4)_2S$. b) Contact resistivities with varying sulfide concentrations at constant sulfide passivation time of 40 s.*

Note that there was no observable etching of the contact layer (InAsSb) while dipping in $(NH_4)_2S$ solution according to the result of Suyatin et al. [88]. However, it is observed that

$(NH_4)_2S$-based solutions etch n- and p-GaSb at a steady rate [89]. Also, the sensitivity of the contact resistance on the Ti thickness was investigated. It has been found that the contact resistance decreases with decreasing Ti thickness. Therefore, only 3 nm of Ti was evaporated at the topside in order to ensure the good adhesion to the semiconductor surface. The reason for using Pt is to prevent the Au diffusion into the semiconductor. Its thickness does not have any influence on contact resistances but it ensures long-term thermal stability. The Au thickness also does not have any influence on contact resistances. 250 nm at the topside assures low mechanical damage on the contact pad while contacting with the probes.

The long-term stability of the contacts was also examined. The contact samples were left at ambient conditions for more than a year during which no reduction of the contact resistivities has been noticed.

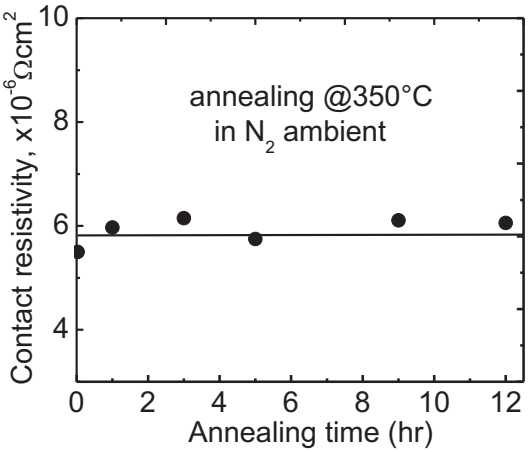

Fig. 3.18: *The contact resisitivites of the Ti/Pt/Au contact on n^+-InAsSb for various annealing times.*

Finally, the thermal stability of the contacts was checked by annealing the sample in N_2 ambient at 350 °C for several hours. These contacts were thermally stable with no deterioration of the contact resistances observed with increasing annealing time as shown in Fig. 3.18. However, for annealing temperatures higher than 400 °C, the degradation of the surface morphology at the backside became visible, because our backside contacts had to be formed on n-GaSb which is affected at this high temperature. In addition, the degradation of the contact resistance started to appear at an annealing temperature of 450 °C possibly due to Sb outdiffusion from the GaSb substrate. Additionally, also Au diffusion into the semiconductor takes place at such a high temperature in spite of the Pt diffusion barrier.

In summary, the fabrication of high quality ohmic contacts to n-GaSb using a lattice-matched n^+-InAsSb contact layer were investigated. A simple surface preparation method using sulfidation prior to metallization has been developed and suitable for the operation of GaSb-VCSELs.

3.2.2 Low-Resistive Tunnel Junction

The buried tunnel junction (BTJ) has been proven to be the most successful concept utilized in long-wavelength VCSELs. Due to the lack of a reliable oxidation technologies in InP- and GaSb-based material system, one has to consider an alternative technique by which current can be confined at the center of the device. In this aspect, BTJ concept is the best technology that can be used for the realization of intra-device ohmic contacts with an extremely low resistivity which ensures an effective lateral current confinement and optical confinement in the device. At the same time, it allows the substitution of the p-type layers by n-type ones on top of the BTJ to obtain low electrical resistance, and, as a consequence, reduced heat generation in the devices.

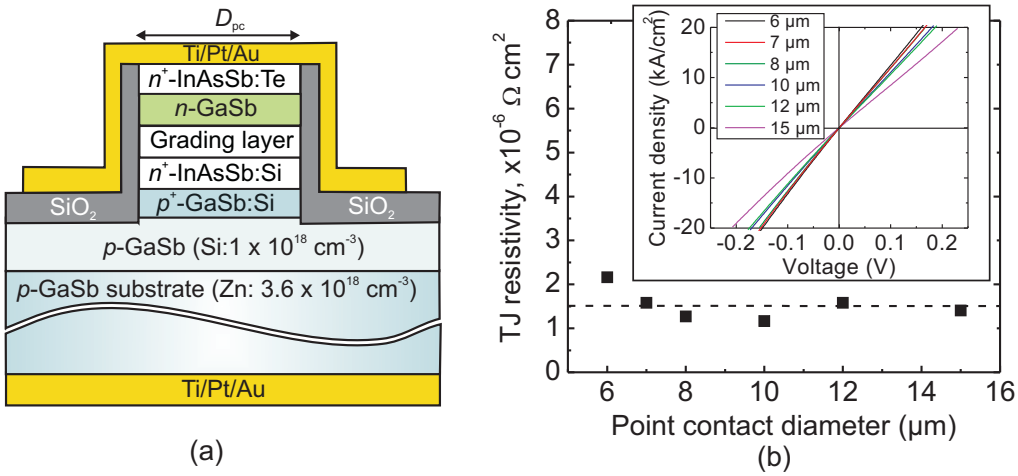

Fig. 3.19: *a) Schematic cross-sectional view of the test structure used for the determination of the tunnel junction resistivity, b) Measured tunnel junction resistivities for different mesa diameters where the J-V characteristics of different mesa diameters is shown as inset. The total resistivity $\rho_{\mathrm{tot}} = V/J$, consisting of contribution from contact, tunnel junction and substrate resistance, can be calculated from here.*

As mentioned before, the tunnel junction in our devices uses highly doped n^+-InAsSb/p^+-GaSb layer. Both layers are doped with amphoteric dopant Si. Such configuration benifits from a type-II broken-gap alignment which inherently introduces the degeneracy for TJ operation even with a low doping in these layers. In addition, the low effective masses of GaSb and InAsSb favor the carrier tunneling process.

In order to deduce the tunnel junction resistivity present in our devices, a test structure as schematically shown in Fig. 3.19 a) are processed on top of p-GaSb substrate so that finally the top p-side contact can be formed on n-InAsSb. The tunnel junction resistivity has been calculated to be as low as $1.5 \times 10^{-6}\,\Omega\,\mathrm{cm}^2$ based on different point contact diameters ranging from 6 µm to 15 µm. Fig. 3.19 b) displays the measured J-V characteristics for the current density range of $\pm 20\,\mathrm{kA/cm}^2$ where the point contact diameter dependent substrate current crowding can be clearly seen. This is due to the fact that substrate spreading resistance $R_{\mathrm{sub}} \propto 1/D_{\mathrm{pc}}$, whereas, both tunnel junction and top contact resistance R_{tj} and

$R_c \propto 1/D_{pc}^2$.

The tunnel junction resistivity ρ_{tj} is extracted by

$$\rho_{tj} = \pi \left(\frac{D_{pc}}{2}\right)^2 \left(R_{tot} - R_c - \frac{\rho_{sub}}{2D_{pc}}\right) \tag{3.4}$$

where ρ_{sub} is the p-GaSb substrate resistivity which is $0.0038\,\Omega$cm and R_{tot} is the total resistance measured experimentally,

$$R_{tot} = R_c + R_{tj} + \frac{\rho_{sub}}{2D_{pc}} \tag{3.5}$$

It is not possible to separate these resistance values except substrate resistance from the measured total resistance by the method in [86]. Therefore, the contact resistance was determined individually from another test sample as shown in Fig. 3.15. All these resistance values contributing to the total measured resistance are tabulated in Tab. 3.3 in order to extract the tunnel junction resistivity ρ_{tj}.

Description	D_{pc} **(µm)**	6	7	8	10	12	15
Total resistance	R_{tot} (Ω)	29	19.7	15.6	11.3	9	6.7
Contact resistance	R_c (Ω)	18	13	11.2	8	6.1	4.7
Substrate resistance	R_{sub} (Ω)	3	2.6	2.2	1.8	1.5	1.2
TJ resistance	R_{tj} (Ω)	8	4.1	2.15	1.5	1.4	0.8
TJ resisitivity (avg.)	ρ_{tj} ($\times 10^{-6}\ \Omega\,cm^2$)	1.5 ± 0.4					

Tab. 3.3: *The extraction of tunnel junction resistivity from the experimental measurement utilizing the method in [86]*

Importantly, the grading layers are used at the interface of n^+-InAsSb and p^+-GaSb. This graded junction is introduced between the n^+-InAsSb and the top n-GaSb layers for better electrical conductivity and ohmic characteristics. These grading layers are made of $(Ga_xIn_{1-x})(As_ySb_{1-y})$ with a homogeneously increasing Ga-content and decreasing In-amount. Details of the design and growth issues are described in [55, 58]. The influence of the grading layer in such structure can be understood from Fig. 3.20 where it is shown that the I-V characteristics becomes completely non-linear without the grading layer. This could be attributed to the presence of high potential barrier at InAsSb/GaSb heterointerface. In contrast, the test structure with grading layer shows low-resistance ohmic characteristics at nominal VCSEL operating current densities (10-20 kA/cm^2) as shown in inset of Fig. 3.19 b).

Therefore, such low-resistive ohmic tunnel junction with a grading layer can be implemented in VCSELs as an intracavity contact to obtain all electrical benefits.

3.2.3 Current Confinement

After the realization of low resistive top p-side contact and tunnel junction, it is of paramount importance for VCSELs to have an efficient current confinement by the tunnel junction itself. The efficiency of the current confinement can be expressed by dividing the current

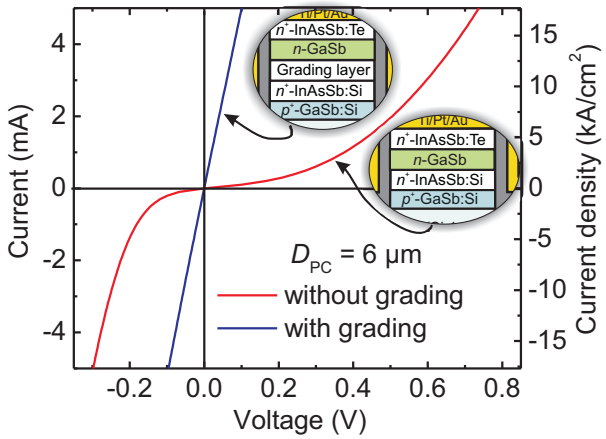

Fig. 3.20: *Measured J-V characteristics of the tunnel juncture test structures with and without grading layer at InAsSb/GaSb heterointerface.*

densities in the center and the outer part of the structure, the so-called blocking ratio. So, the higher the blocking ratio, the better the current confinement in the device.

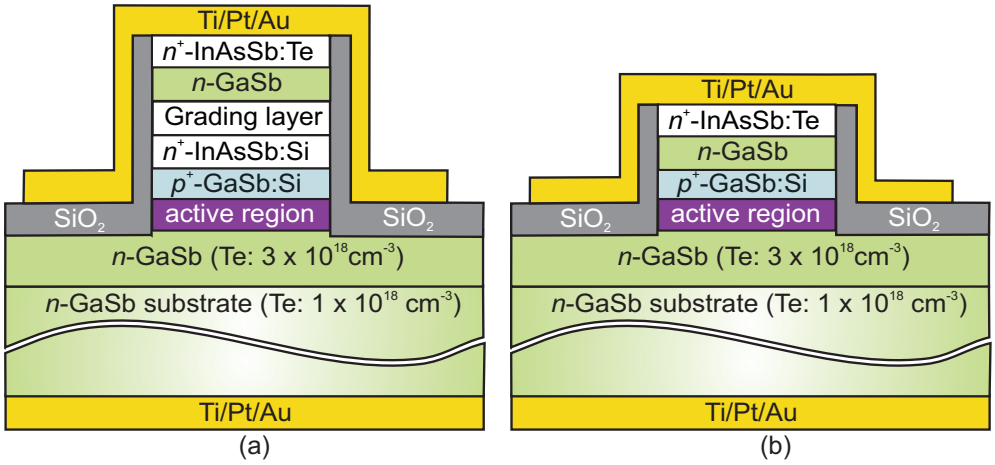

Fig. 3.21: *Schematic cross-sectional view of the test structure used for the determination of the current confinement efficiency in VCSELs. Both a) conducting and b) blocking test structures were grown in single growth step.*

The current confinement efficiency was investigated with simplified non-lasing structures with active region but without Bragg mirror as illustrated in Fig. 3.21. Such structures were realized in a single growth step in order to determine the maximum achievable blocking ratio. These structures can be referred to as conducting and blocking ones. In the conducting structure, the presence of both tunnel junction layers n^+-InAsSb and p^+-GaSb make a structure conducting, whereas the absence of n^+-InAsSb layer make it blocking as shown in Fig. 3.21 a) and b), respectively. Note that, the blocking performance in such structure is influenced by the doping concentration of the n-GaSb layer, which is right below the n^+-InAsSb contact layer. Because the doping concentration controls the depletion region width in n-p^+ reverse biased junction when the device is forward biased, therefore

the blocking behavior. Note that the lower doping limit for n-GaSb is in the range of 1×10^{17} cm^{-3} due to the background p-doping or antisite defects in GaSb material.

The test structures are formed by etching down through the tunnel junction. The current confinement is impressively confirmed by the J-V measurement for the current density up to 20 kA/cm^2, as displayed in Fig. 3.22. The curves are taken for two point structures with $D_{\mathrm{pc}} = 10\,\mu\mathrm{m}$ which corresponds to $D_{\mathrm{BTJ}} = 10\,\mu\mathrm{m}$ and $D_{\mathrm{BTJ}} = 0$. This means that these structures represent either a center region with tunnel junction or blocking interface, respectively. At a VCSEL operating voltage of 1 V, a current density of 20 kA/cm^2 is achieved for the device with $D_{\mathrm{BTJ}} = 10\,\mu\mathrm{m}$, only 0.001 kA/cm^2 is observed for the structure with $D_{\mathrm{BTJ}} = 0$. This yields a current density ratio of 20,000 as shown in inset of Fig. 3.22. Since the VCSEL processing requires twofold epitaxial growth, this value is reduced due to the oxides or C-related contaminations before the overgrowth. To remove the contaminations and oxides, wet chemical based cleaning followed by Atomic Hydrogen Cleaning (AHC) is used prior to overgrowth which reduces the blocking ratio value about one order of magnitude lower than the reference sample. Nevertheless, it has been found out that the value of 1,000 is sufficient for lasing operation in GaSb-based VCSELs.

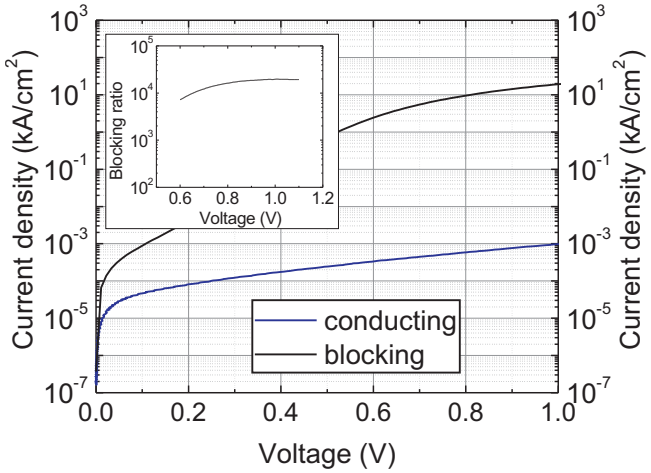

Fig. 3.22: *J-V characteristics of conducting and blocking test structures in order to evaluate the current confinement efficiency. The blocking ratio as a function of applied voltage is shown as inset.*

3.2.4 Lateral Current Spreading

Beside the active region diode, top p-side contact, tunnel junction and bottom epitaxial DBR, the top n-GaSb based lateral current spreading resistance also contribute to the electrical characteristics of the device. The fundamental equation governing the voltage drop ΔV_{cs} due to such resistance is given by [90]

$$\Delta V_{\mathrm{cs}} = J\rho_n \left(\frac{D_{\mathrm{BTJ}}}{2}\right)^2 \frac{1}{2d_{\mathrm{cs}}} \ln\left(\frac{D_{\mathrm{cont}}}{D_{\mathrm{BTJ}}}\right) \tag{3.6}$$

where J is the current density with respect to the tunnel junction area, ρ_n the resistivity of n-GaSb layer, d_{cs} the thickness of the current spreading layer and D_{cont} the inner diameter

of the contact ring as shown in Fig. 3.23. For GaSb-based VCSELs at 2.6 µm, using the thickness of the top n-GaSb current spreading layer, $d_{\mathrm{cs}} = 1.1$ µm and the resistivity of that corresponding material $\rho_n = 0.0025\,\Omega\,\mathrm{cm}$, applying $20\,\mathrm{kA/cm^2}$ to the device with $D_{\mathrm{BTJ}} = 8$ µm and $D_{\mathrm{cont}} = 18$ µm, the voltage drop due to the spreading resistance can be calculated to be approximately 30 mV.

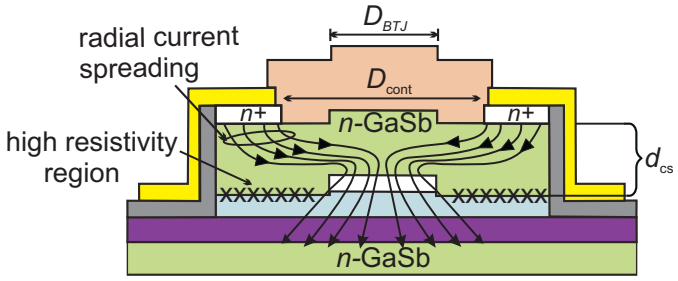

Fig. 3.23: *Current spreading phenomenon in GaSb-based BTJ VCSELs. The lateral current flow through the tunnel junction is shown.*

3.3 Thermal Design

Thermal modeling is one of the key design issues for devices utilizing the low bandgap material system, GaSb. Generally the device performance, i.e. optical output power and threshold current is limited by thermal effects. To gain a deep insight into GaSb-based BTJ VCSELs, at first the theoretical and systematic thermal analysis using a heat dissipation model will be presented here. The device thermal parameters, such as internal temperature distribution, heat flux, and thermal resistance can be extracted out of the model based on the two-dimensional (2-D) rotationally symmetric, steady-state heat transfer model. The analysis was done by using COMSOL Multiphysics finite element analysis simulation software [91]. The thermal conductivity of each layer in GaSb-based BTJ VCSELs are taken from the literature [92, 93] and summarized in Tab. 3.4 along with brief details and the thickness of that corresponding layer. In this analysis, the effective thermal conductivities with anisotropy were used for thin multilayers, e.g. active region. The effective thermal conductivities in lateral and vertical directions are given by [94]

$$k_{\mathrm{l}} = \frac{d_1 k_1 + d_2 k_2}{d_1 + d_2}, \qquad k_{\mathrm{v}} = \frac{d_1 + d_2}{d_1/k_1 + d_2/k_2} \tag{3.7}$$

where k_1/k_2 and d_1/d_2 are the thermal conductivity and thickness for layer 1/layer 2, respectively. For the active region and bottom epitaxial Bragg mirror, the effective thermal conductivity value is used defined by Eqn. 3.7. Here, reduced values are expected that are caused by phonon mean free path restrictions in thin layers.

As shown in Fig. 3.24 b), a large amount of heat from the active region flow laterally and vertically downward toward the GaSb substrate through bottom epitaxial DBR and also laterally toward the top p-side Au-contact. This has been indicated by long white arrows, showing the heat rapidly spreads out over a wide area in the radial direction. The heat source is sandwiched by top and bottom GaSb heat spreading layer which also contributes

Description	Material	Thickness (nm)	k (W/m-k)
Top p-side contact	Au	300	317
Passivation layer	SiO_2	250	1.4
Top dielectric DBR	a-Si/SiO_2	188/455	1.8/1.4
Top current spreading layer	GaSb	1120	32 [92]
Bottom current spreading layer	GaSb	520	32 [92]
Top n-side contact	Au	300	315
Bottom epitaxial DBR	$AlAs_{0.08}Sb$/GaSb	200/170 (24 pairs)	19.8 [93]/32 [92] k_l= 20, k_v = 14.4
Active region (QW/Barrier)	$In_{0.43}GaAs_{0.14}Sb$/GaSb	10/8	4/32 [92], k_l = 16, k_v = 5

Tab. 3.4: *Thermal conductivity for different layers in GaSb-based BTJ VCSELs*

to dissipate the heat.

The active region diameter, $D_{\mathrm{BTJ}} + 2r_{\mathrm{diff}} = 5.5\,\mu\mathrm{m} + 3.4\,\mu\mathrm{m} = 8.9\,\mu\mathrm{m}$ has been considered in this simulation by taking the effective pumped area of the device into account, where r_{diff} is the carrier diffusion length which has been experimentally measured. This will be presented in Chap. 6. Since the wallplug efficiency is nearly zero at threshold, all input electrical power is assumed to be dissipated in the form of heat. Thus, the volumetric heat source density Q can be experimentally determined by

$$Q = \frac{I_{\mathrm{th}} \cdot V_{\mathrm{ac}}}{V} = \frac{I_{\mathrm{th}} \cdot V_{\mathrm{ac}}}{\frac{\pi}{4} \cdot (D_{\mathrm{BTJ}} + 2r_{\mathrm{diff}})^2 \cdot h} \tag{3.8}$$

where V_{ac} and I_{th} are the voltage drop across the active region and threshold current, respectively, V and h are the volume and thickness of the active region, respectively. The voltage drop across the active region is obtained by subtracting ohmic drop arising from the laser series resistance from the measured threshold voltage V_{th}

$$V_{\mathrm{ac}} = V_{\mathrm{th}} - I_{\mathrm{th}} \cdot R_{\mathrm{s}} \tag{3.9}$$

where R_{s} is the series resistance. The measured threshold current, threshold voltage and series resistance of the device with $D_{\mathrm{BTJ}} = 5.5\,\mu\mathrm{m}$ are 3.2 mA, 0.62 V, and 33 Ω, respectively. So, V_{ac} can be calculated to ≈ 0.51 V. Thus the total dissipated heat power in the active region is 1.6 mW. The rest of the power ≈ 0.4 mW is assumed to be dissipated as joule heating in the other layers whose effect to rise in active region temperature is almost negligible. Using these values in the simulation, the maximum heating of $\Delta T = 4$ K in the active region with respect to the heatsink temperature is obtained which corresponds to a thermal resistance of ≈ 1995 K/W, showing a good agreement with the experimental value mentioned in Chap. 6.

As displayed in Fig. 3.24 a), most of the heat (80%) generated in the active region flow downward mainly to the copper heatsink by conduction through the GaSb substrate (45%)

and epitaxial bottom DBR (35%). The rest of the heat is mainly transferred to the air by radiation and natural convection through the top p-side Au contact. The top dielectric DBR hardly conducts any heat due to the low thermal conductivities of dielectric materials. Since the presented devices with upside-up concept already show good thermal properties, the upside-down concept would even improve the thermal management in such devices.

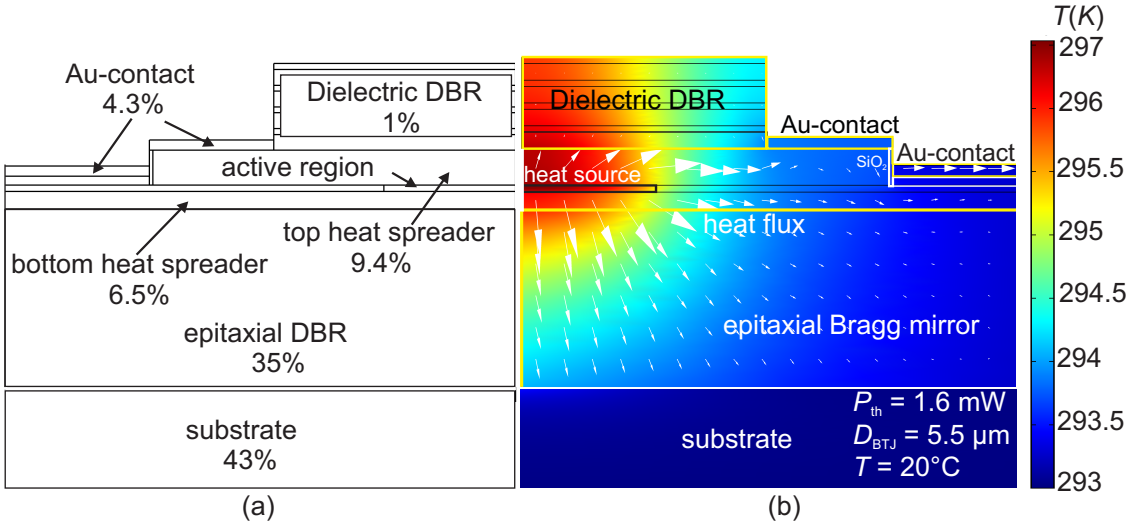

Fig. 3.24: *a) 2-D GaSb-based top emitting VCSEL structure employing a rotational structural symmetry along the z-axis used in the simulation. The contribution of different layers of the device in dissipating the heat is shown in percentage as well. b) 2-D steady state heat flux and temperature distribution. The black rectangle represents the QW region which has been assumed to be the main heat source in this simulation. The bottom epitaxial Bragg mirror on top of 500 µm thick GaSb substrate and top dielectric Bragg mirror have been marked with yellow border lines. White arrows represent the magnitude and the direction of the heat flow.*

4 GaSb-VCSEL Fabrication

Fabrication processes play crucial roles in realizing high performance devices. Having already dealt with the device design for GaSb-VCSELs in Chap. 3 now all of the processing steps involved in the fabrication of such devices will be described in this chapter. This device fabrication has gone through many iterations of optimization, but ultimately only the steps finally involved in the fabrication of working devices will be briefly described here.

4.1 Fabrication Techniques

Though all the device results which will be presented in Chap. 6 for the top-emitting structure, a significant amount of time was spent in optimizing the processing steps for the realization of bottom-emitting structures within the frame of this work. As already mentioned, the bottom emitting devices have a better thermal management. From epitaxial growth point of view, the bottom-emitting structure is advantageous since devices can be fabricated with the short cavity concept [95], i.e. the inner cavity is sandwiched by both top and bottom dielectric DBR. Compared to the top-emitting structure, the 8-10 µm thick bottom epitaxial DBR will not be needed in this case, making devices less growth time-consuming. Note that for a top-emitting structure, the MBE growth continues for 14-15 hours in growing such thick epi-DBR.

Furthermore, it is also important to assure a stable, reproducible and uniform growth platform before the VCSEL growth. This can be done by growing some calibration test structures. For instance, *in-situ* reflectance is used to monitor the growth routinely. In addition, a pre-growth calibration of the material growth rate and determination of incorporation factor of group-V elements are performed using several test structures. This clearly indicates that top-emitting structure involves a lot of effort in advance before growing a VCSEL structure.

So, the emphasis in this chapter will be given on the processing steps for bottom-emitting structure which allows us to grow a VCSEL structure without such a tedious set of calibration runs and the growth of a very thick epi-DBR itself. The drawback of this concept is that it involves complicated and time-consuming processing steps in realizing the device.

4.1.1 Upside-up Design

As far as the device structure and processing are concerned, GaSb-based BTJ VCSEL processing with upside-up configuration is simpler and easier than upside-down technique. In addition, the processing time is also rather short, i.e. less than 3 weeks. Details of each processing step involved in VCSEL with upside-up concept can be found in [59]. Nonetheless, the process flow in realizing such devices will be briefly mentioned below. All the fabrication process is illustrated with the sequence in Fig. 4.1 and 4.2.

1. **Half-VCSEL Structure by MBE Growth**
   First epitaxial growth for base structure consisting of bottom epitaxial mirror, GaSb current spreading layer, active region, tunnel junction layers and cap GaSb layer. See Fig. 4.1 a).

2. **1st Pre-processing Analysis**
   Before the actual device processing begins, i.e. after the first epitaxial growth it is of great importance to measure the reflectivity spectrum of the half-VCSEL structure. A lot of valuable information relating to epitaxial growth, e.g. rough estimation of the thickness of the bottom epi-DBR as well as the layers contributing to the inner cavity can be extracted from the spectrum which is taken into account for the following device processing steps.

3. **Tunnel Junction Structuring**
   Selective wet chemical etching for removing cap GaSb layer and dry chemical etching for only InAsSb tunnel junction layer. See Fig. 4.1 b).

4. **Overgrowth**
   Second epitaxial growth by MBE after a wet-chemical pre-cleaning step followed by an *in-situ* cleaning with atomic Hydrogen under high vacuum condition. See Fig. 4.1 c).

5. **2nd Pre-processing Analysis**
   Several useful measurements, e.g. photoluminescence, reflectivity and high-resolution X-ray diffraction (HRXRD) are done after the overgrowth. The photoluminescence measurement for the active region is done directly on a part of the wafer where there is no highly doped first tunnel junction layer, InAsSb. That part is also free from topmost highly doped contact layer, facilitating the PL measurement. Also the reflectivity measurement is performed on a part of that wafer with tunnel junction layers but without contact layer. Note that the highly doped absorbing contact layer is not part of the cavity. Besides, the structural components of the device, such as the alloy composition and the layer thickness of QWs, DBRs can be known from the exact fit of a simulated X-ray diffraction pattern to a measured diffraction pattern.

6. **Mesa Formation and Passivation by SiO_2**
   Forming the mesa by wet chemical etching for removing top contact layer and dry chemical etching for GaSb layer and stopping the etching process before the active region. See Fig. 4.1 d).
   Mesa passivation by SiO_2. See Fig. 4.1 e).

7. **Contact Layer Structuring**
   Etching of topmost InAsSb contact layer by wet chemical etching. See Fig. 4.2 f).

8. **Metal Evaporation for *p*- and *n*-side Contact**
   E-beam evaporation of non-alloyed Ti/Pt/Au contact with a correct thickness. Details of the evaporation technique after the contact surface preparation can be found in Chap. 3. See Fig. 4.2 g).

9. **Evaporation of Top Dielectric Bragg Mirror**
   E-beam evaporation of 4 pairs of SiO_2/a-Si. By adjusting the thickness of the first

dielectric layer contributing to the inner cavity, the epitaxial growth inaccuracy can be corrected in this step. See Fig. 4.2 h).

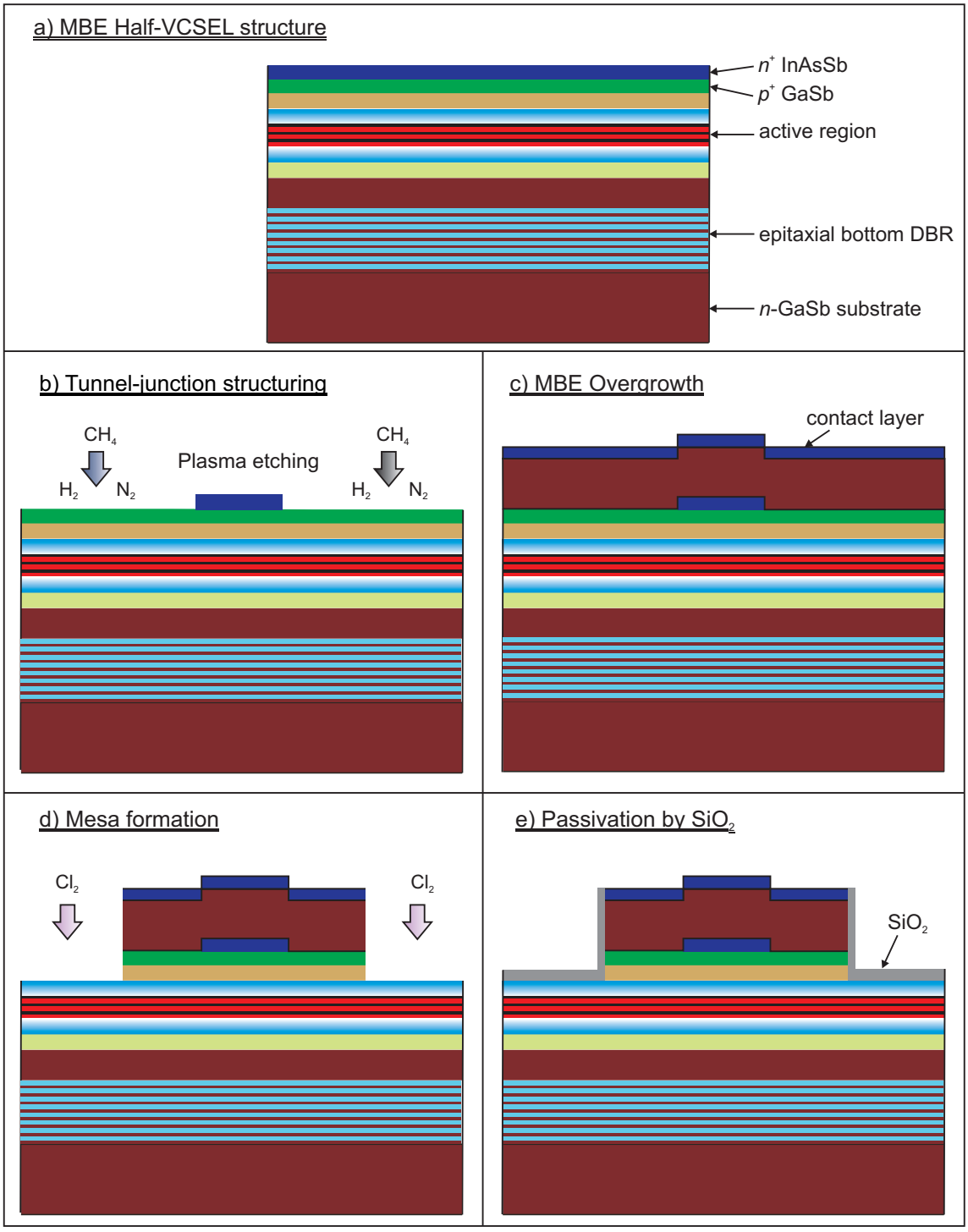

Fig. 4.1: *Illustration of the process flow for GaSb-BTJ VCSELs with upside-up configuration*

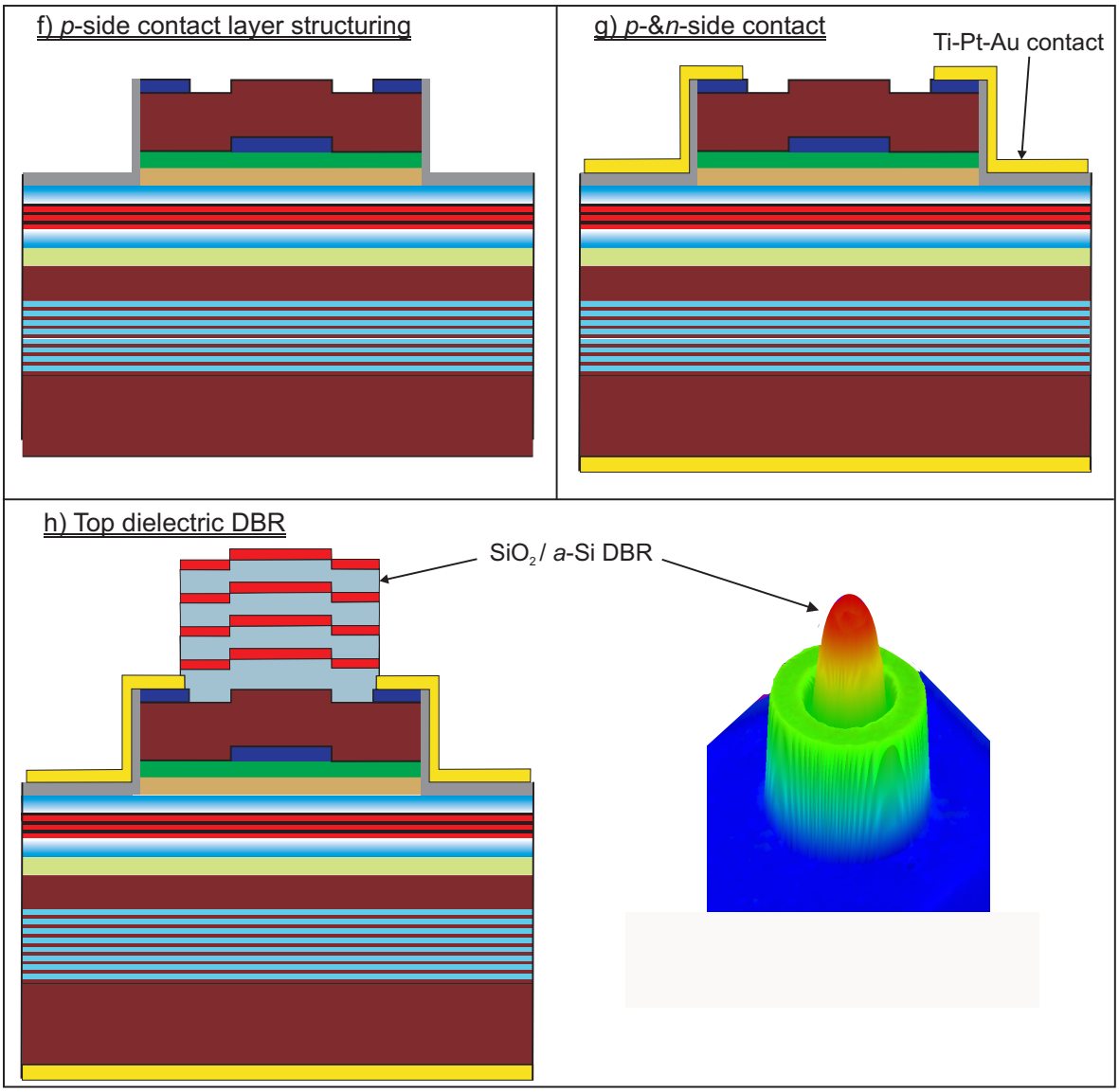

Fig. 4.2: *Process flow for VCSELs with upside-up configuration (contd.). White light interferometer photo (bottom right)*

4.1.2 Upside-down Design

VCSELs with upside-down configuration are often considered to be a better concept for an improved thermal management in long-wavelength devices. In InP-based VCSELs, this has already been confirmed [53]. Recently a so-called new concept short-cavity InP-VCSEL has been reported [95], that can be utilized in GaSb-based VCSELs too. The pros and cons of this concept will be as follows:

Pros

- No epitaxial bottom DBR lead to a simple epitaxial structure
- Large fabrication tolerances due to use of top and bottom dielectric DBR with a very broad stopband

- Better thermal properties due to an efficient heat removal through the bottom integrated Au-heatsink and top metal contact.

Cons

- Complex device structure
- Complex device processing including substrate removal
- Time-consuming processing

Now the process flow of the device with upside-down configuration will be described. GaSb VCSEL processing with an upside-down configuration involves 10 lithography steps, wet-chemical and dry-chemical etching, overgrowth with GaSb and InAsSb after structuring of the tunnel junction, the deposition of dielectric mirrors and metal contacts through e-beam evaporation. After the galvanic deposition for a thick gold-heatsink as pseudo-substrate, the GaSb substrate is removed. The device processing is continued at the backside of the sample.

1. **Half-VCSEL Structure by MBE Growth**
   Compared to VCSEL epi layers for the upside-up concept, the only difference for upside-down configuration is the missing epi-DBR and insertion of 200 nm thick lattice-matched $InAs_{0.91}Sb_{0.09}$ layer which will act as a etch-stop layer in the substrate removal process . The half-VCSEL structure after the first epitaxy step is displayed in Fig. 4.3. Then the next processing steps, e.g. the tunnel junction structuring, overgrowth step, mesa formation and passivation by SiO_2 are exactly the same as the processing steps mentioned in Sect. 4.1.1. See Fig. 4.3 a).

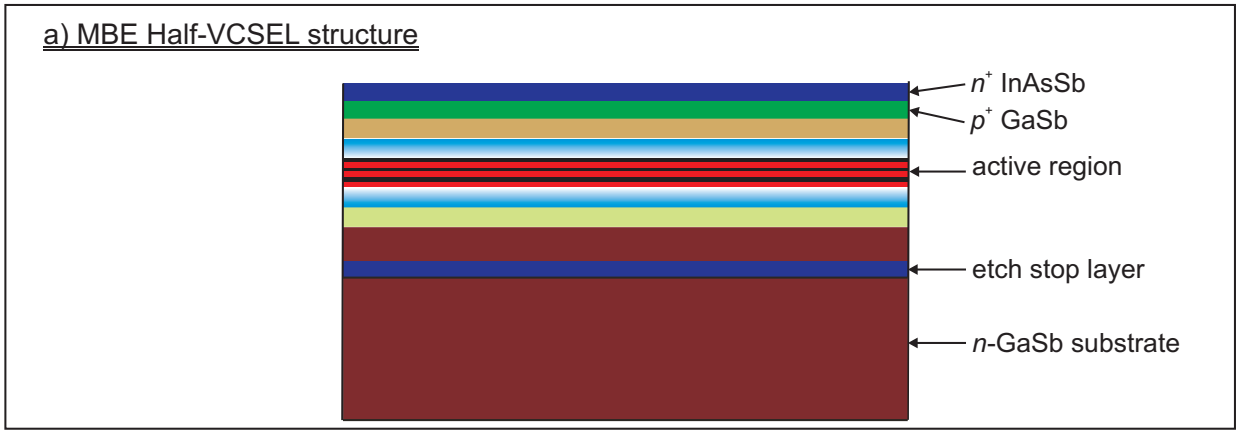

Fig. 4.3: *Schematics of the process flow for GaSb-BTJ VCSELs with upside-down configuration, see Fig. 4.1 for process flow no. 2-5*

2. **1st Pre-Processing Analysis** See Sect. 4.1.1.
3. **Tunnel Junction Structuring** See Sect. 4.1.1 and Fig. 4.1 b).
4. **Overgrowth** See Sect. 4.1.1 and Fig. 4.1 c).

5. **2nd Pre-Processing Analysis** See Sect. 4.1.1.

6. **Mesa Formation and Passivation by SiO_2** See Sect. 4.1.1 and Fig. 4.1 d) and e).

7. **Contact Layer Structuring**
   Etching of topmost InAsSb contact layer by wet chemical etching. See Fig. 4.4 f).

8. **Metal Evaporation for *p*-side Contact**
   E-beam evaporation of non-alloyed Ti/Pt/Au contact ring for p-side with a correct thickness. Details can be found in Chap. 3. See Fig. 4.4 g).

9. **Evaporation of Hybrid Bottom Mirror**
   As back mirror, e-beam evaporation 1.5 pairs of SiO_2/a-Si + Au to reach sufficient reflectivity. See Fig. 4.4 h).

10. **Alignment Marker for the Backside**
    For doing the standard photolithography at the backside of the sample after the substrate removal, some alignment markers are structured by etching through all semiconductor layers including the etch stop layer by reactive ion etching (RIE) using chlorine. These structures can be considered as alignment markers which helps in aligning the structures at the backside of the sample. See Fig. 4.4 i).

11. **Pseudo-Substrate - Electroplated Gold**
    Before the substrate removal procedure, the backside of the sample should be covered with approximately 50 µm thick gold layer by electroplating which will act as an integrated heatsink as well as a pseudo-substrate for the mechanical stability of the sample. See Fig. 4.4 j).

12. **Substrate Removal**
    As a part of the substrate removal procedure, initially the bulk of the 500 µm thick GaSb substrate should be thinned down to 60-80 µm using a combination of lapping and mechanical polishing in Brome-Methanol solution. The sample was then carefully cleaned in order to make sure that no residue would create non-uniformities during the next wet chemical thinning. It was necessary to thin down the sample to 60-80 µm prior to wet etching because the non-uniformity of the etching can create the disappearance of the etch stop in some parts of the sample before the substrate is fully removed. See Fig. 4.4 k).

    Then the remaining substrate should be removed by using highly selective CrO_3:HF:H_2O-based etching solution to expose the etch stop InAsSb layer. The etching solutions were prepared by mixing 33% CrO_3 solution (33 wt%) with 50% HF (50 wt%). Then this mixture is diluted with water. This can be expressed by the notation $D_{1:x}$, i.e. dilution of 1 volume part of mixture solution with x volume parts of water. By using such solution, bulk GaSb can be etched very selectively against InAsSb. Fig. 4.5 a) displays the etch rate in µm/min as a function of dilution ratio x where it is seen that the etch rate decreases with increasing x as expected. The etching rate of 6 µm/min using dilution ratio $x = 5$ is used during the substrate removal for a controllable etching.

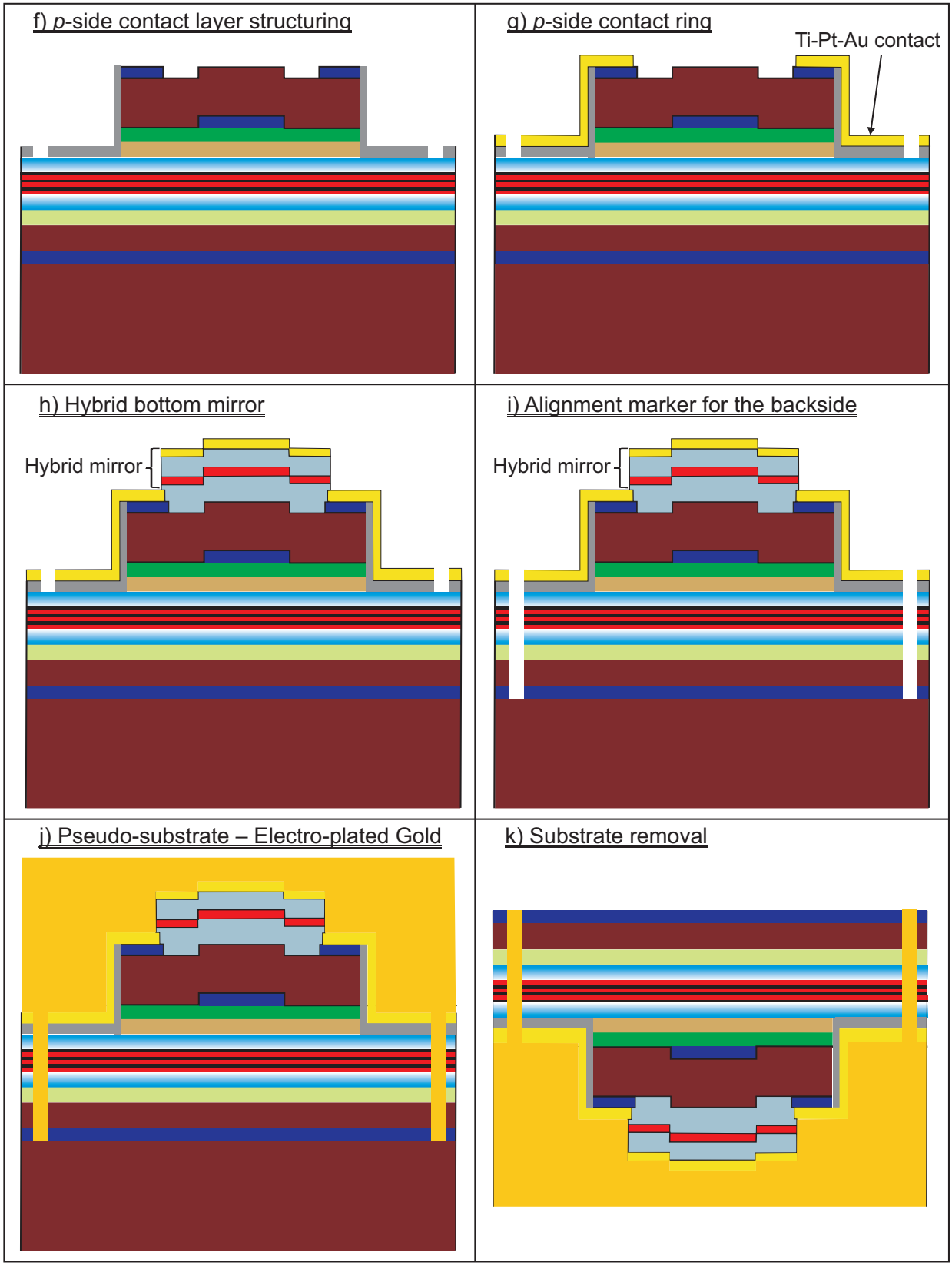

Fig. 4.4: *Process flow for VCSELs with upside-down configuration (contd.)*

During the etching, it must be avoided that the metallized p-side and GaSb-substrate get exposed to the etchant at the same time which results in an electrochemical effect [96, 97]. In order to prevent this known effect, the sample with metallized p-side down is glued to the HF-acid resistant CaF_2 carrier using adhesive and chemically nonreactive beeswax. Beeswax is a material of choice because of its excellent resistant to acid and its low melting point of just above 60°C. Care should also be taken in covering the edge of the sample with beeswax so that metallized p-side does not appear in the etching solution. Otherwise, a strong lateral etching will be observed at the edge of the sample.

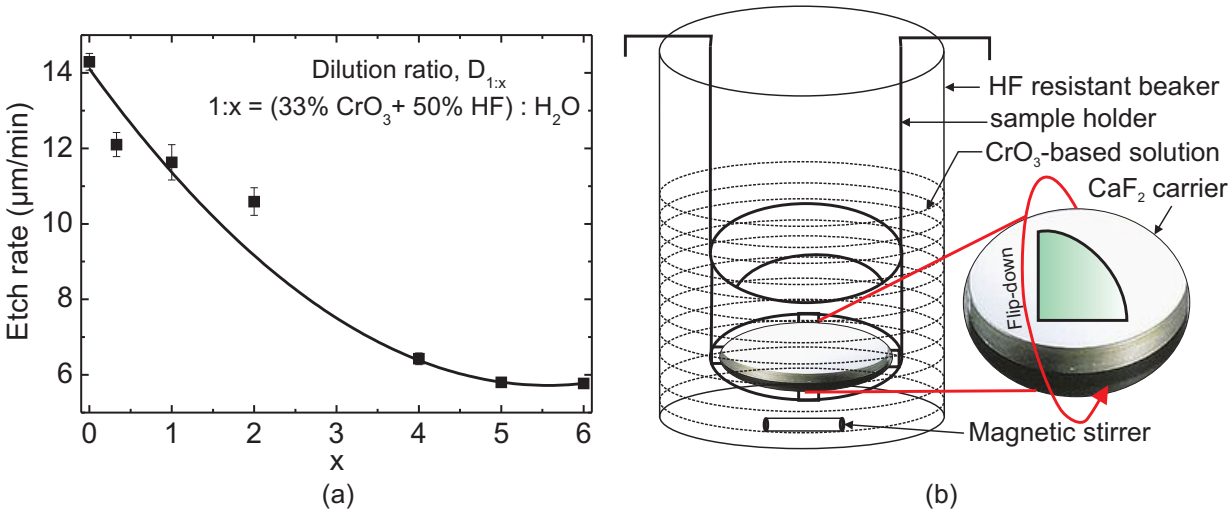

Fig. 4.5: *a) Etch rate of GaSb substrate as a function of dilution ratio ($D_{1:x}$). Error bars are used to indicate the range of measured etch depth, b) the schematic of the setup used for the GaSb substrate removal.*

During the etching, very viscous brown-colored reaction products are formed on the GaSb surface which decreases the etch rate. In order to prevent this effect, the sample attached to the CaF_2 carrier is flipped down and kept at the sample holder as shown in Fig. 4.5 b). Then the sample with holder is immersed into the etching solution under continuous stirring by a magnetic stirrer which remove reaction products from the GaSb surface. This arrangement also helps in getting a constant etch rate. In addition, fresh etch solution is used after the use of old etchant for 5-6 minutes. During the substrate removal process, at least 2 fresh solutions should be used for etching of 60-80 µm GaSb. Due to a very high selectivity of this etching solution against GaSb, the etching stops at the etch stop layer InAsSb. Thus a smooth, mirror-like light-blue colored InAsSb layer can be obtained in this way. The CaF_2 carrier can be separated from the sample by gently heating them in N-Methylpyrrolidone (N-MP) for a couple of minutes. Due to the residuals of beeswax, a very thorough cleaning is necessary. This can be done by rinsing the sample in a xylene cleaning solvent and then dipping in diluted HCl and the subsequently cleaning in deionized (DI) water.

13. ***n*-side Contact Layer Structuring**
    Like bottom *p*-side, *n*-side metal-semiconductor contact is formed on a highly doped n^+-InAsSb layer which has to be structured in order to reduce the free carrier absorption losses. In other words, InAsSb layer should be etched away from the light emitting region defined by the BTJ plus an extension on both sides. Again the etching of this contact layer is done by using citric acid-based etchant with a reasonable selectivity against GaSb layer underneath. See Fig. 4.6 l).

    It should be noted that, the metal *p*-side of the sample must not get in touch with the etching solution while removing the InAsSb contact layer. Otherwise, the etching rate will increase and the etch selectivity will decrease. In order to avoid this problem, the *p*-side of the sample is again glued to a glass carrier with the beeswax. After the etching, the sample is detached by heating in N-MP and finally cleaned in the xylene solvent.

14. ***n*-side Contact Ring**
    E-beam evaporation of non-alloyed Ti/Pt/Au contact ring for *n*-side after a sulfidation-based surface treatment. Details can be found in Chap. 3. See Fig. 4.6 m).

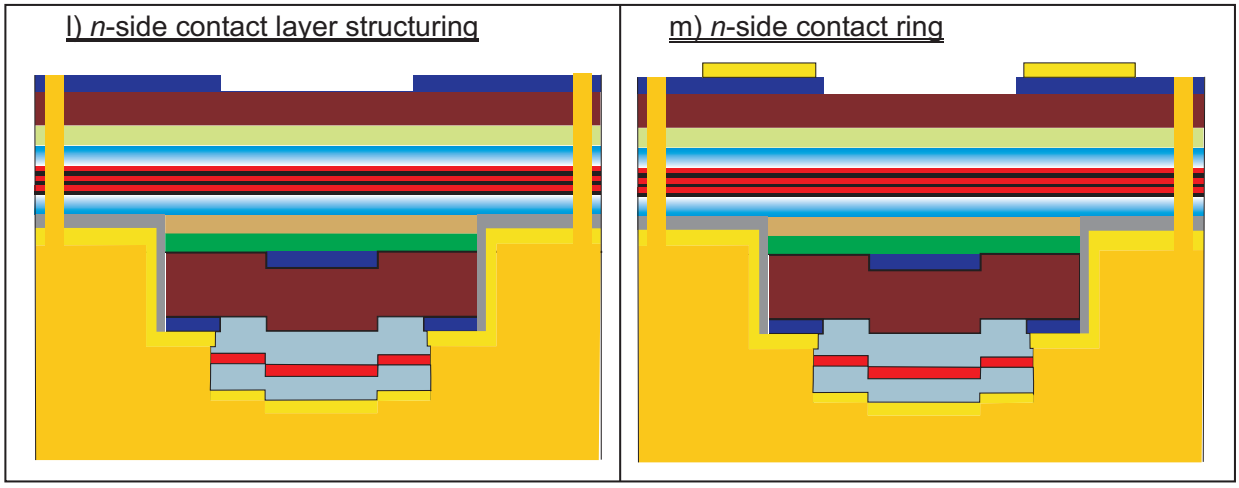

Fig. 4.6: *Process flow for VCSELs with upside-down configuration (contd).*

15. **Electrical Separation**
    The single device is electrically separated from the adjacent one by etching through all semiconductor layers up to before the bottom SiO_2 passivation layer. This can be done by wet chemical etching of InAsSb layer in citric acid-based solution followed by dry chemical etching of the rest of the semiconductor materials in a RIE reactor using chlorine. See Fig. 4.7 n).

16. **Evaporation of Top Dielectric Bragg Mirror**
    See Sect. 4.1.1 and Fig. 4.7 o).

This chapter illustrates the manufacturing process of GaSb-based BTJ VCSELs with a pictorial representation. The emphasis has been given on the processing for VCSELs with an

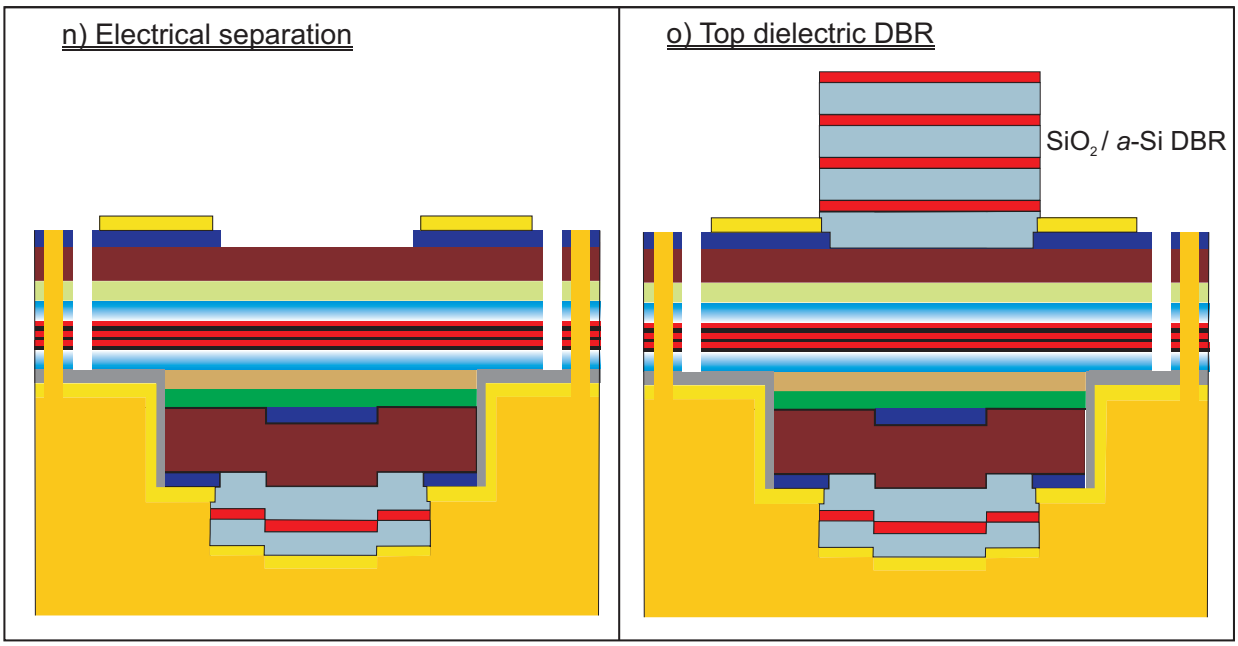

Fig. 4.7: *Process flow for VCSELs with upside-down configuration.*

upside-down configuration. But unfortunately, due to various problems in the challenging fabrication processes mentioned above, the upside-down configuration has not been proved yet to be a successful concept to fabricate working VCSELs in spite of its some important benefits. The most critical part of this concept is the substrate removal step which needs to be removed homogeneously over the whole sample surface with a good selectivity against the etch stop layer. During the subsequent wet chemical etching after the substrate removal process, special care should be taken to keep the rest of the cavity layers unaffected. These need to be investigated in the future thoroughly.

5 Material Characterization

The active region providing gain is one of the most important parts in VCSELs. Before its use in VCSELs as a gain medium, often edge-emitting laser diodes are fabricated to evaluate the active region in a qualitative and quantitative way. The main reason of spending a reasonable amount of time in studying edge-emitting lasers is that edge-emitters, due to its simple device structure, allows the extraction of the active region performance from the measured device performance. In addition, due to its simple, easy and less time-consuming device processing, rapid feedback in terms of extracting the useful data from the device performance can be obtained for the design of the next generation devices.

5.1 Ultra-low Threshold Edge-Emitter

Photoluminescence

In order to investigate the optical emission properties of the quantum well samples, photoluminescence measurement is generally performed. Fig. 5.1 shows the low-temperature photoluminescence of $In_{0.43}Ga_{0.57}As_{0.15}Sb_{0.85}$ QWs used in EEL to evaluate the quality of the active region. Low-temperature photoluminescence (PL) spectra exhibit FWHM as narrow as 4 meV. This reflects the excellent optical properties of the active region material. As a rule of thumb, a FWHM lower than 10 meV indicates a good crystalline quality of the grown structure.

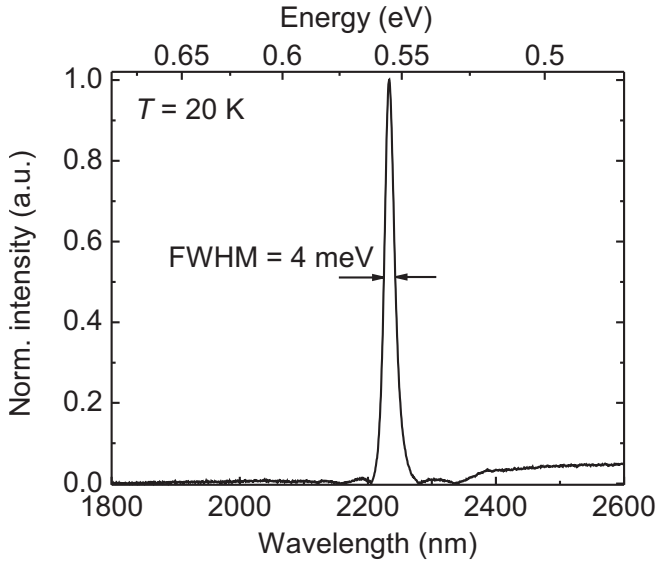

Fig. 5.1: *Photoluminescence measurement at 20K from edge-emitter. The linewidth (FWHM) is indicated in meV.*

Characteristic Laser Parameters

To justify this active region performance, also the characteristic laser parameters is experimentally measured. In fact, characteristics laser parameters from the simple edge-emitting laser enables to evaluate the performance of the active region beyond that of the photoluminescence measurement. This feedback eases to make the decision whether the active region configuration used in edge-emitters can be successfully implemented in VCSELs. Tab. 5.1 shows the characteristic parameters of the active region used in edge-emitters.

CW $J_{\mathrm{th,inf}}$ [$\mathrm{A/cm^2}$]	pulse $J_{\mathrm{th,inf}}$ [$\mathrm{A/cm^2}$]	α_{i} [$\mathrm{cm^{-1}}$]	η_{i} [%]	CW T_0 [K]	pulse T_0 [K]
63	44	3.3	34 ± 4	34 K	44 K

Tab. 5.1: *Characteristic laser parameters of the edge-emitter utilizing the active region used in 2.6 µm VCSELs. The values of some laser parameters are indicated with calculated errors.*

In Tab. 5.1, $J_{\mathrm{th,inf}}$ is the required threshold current density for a laser with $\alpha_{\mathrm{m}} = 0$ or infinite length. That means only the internal loss must be compensated to reach laser threshold. T_0 is the characteristic temperature which expresses the sensitivity of the active region with temperature in terms of threshold current. The presented values are given in the temperature range from 0°C to 50°C.

Note that this MBE-grown GaInAsSb/GaSb strained quantum-well (QW) ridge waveguide (RWG) diode lasers show ultra-low threshold current densities of 44 $\mathrm{A/cm^2}$ ($L \to \infty$) for a single QW which is the lowest reported value in CW operation near room temperature (15°C) [98]. Finally, This active region, showing an excellent performance, has been used in 2.6 µm VCSEL structure.

5.2 2.6 µm VCSEL Structure Characterization

After obtaining an optimized and good quality active region by edge-emitting lasers, it is of great importance to characterize the material of VCSEL sample. Such characterization is carried out in several steps by which one can get a lot of information about the sample, for instance, epitaxial growth quality, layer thickness inaccuracy etc. This information is very useful since the necessary action can be taken during the VCSEL processing to compensate any errors made during the epitaxial growth.

5.2.1 Half-VCSEL Structure

As already mentioned, the first epitaxial growth of GaSb-based BTJ VCSELs ends with the tunnel junction layers followed by a grading and cap layer which can be considered as a half-VCSEL structure. At this stage, the reflectivity spectrum of the structure can be measured in order to see the epitaxial growth inaccuracies in terms of layer thicknesses and the reflectivity of the bottom epitaxial DBR. The center wavelength of the mirror is first estimated as the energy at the halfway point between the energies where the reflectivity

value is approximately 90%. Note that layer thickness inaccuracies mainly comes from the growth of 8-9 µm thick (depends on the resonance wavelength) bottom epitaxial DBR and the incomplete inner cavity. The reflectivity spectrum is then calculated using transfer matrix method.

Fig. 5.2 shows the measured reflectivity spectrum of the half-VCSEL structure designed for 2.6 µm in the wavelength range from 2 to 3.4 µm. The simulated reflectivity spectrum has been inserted in the same figure, indicating the 24 pair AlAsSb/GaSb Bragg mirror with a reasonable reflectivity and an incomplete cavity. It should be stressed that the cavity-dip in the spectrum formed by the bottom epitaxial DBR and top semiconductor-air interface is not at the middle of the stopband, at the short wavelength side instead. This is resulting from the incomplete thinner cavity of the structure.

The measured profile shows a good match with the simulated one except at the magnitude of the reflectivity in the stopband region. The mismatch in the stopband regime is due to the presence of many strong water absorption lines as can be identified in from Fig. 5.2. In fact, these absorption lines reduces the measured normalized reflectivity. Finally the better fit at the stopband width, even at the oscillation fringes outside the stopband and at the cavity dip aligned at a particular wavelength simply tells that the thickness of the quarter-wave alternating layers in the bottom mirror and the incomplete cavity thickness after the first growth step is almost correct. Such close fit also proves to have a proper knowledge on the material refractive index data in this long wavelength regime.

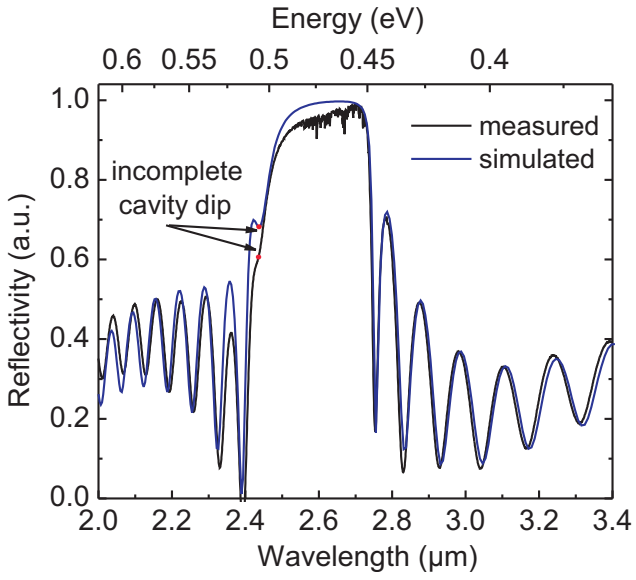

Fig. 5.2: *The measured and simulated reflectivity spectra of the half-VCSEL structure designed for 2.6 µm emission wavelength after the first epitaxial growth. The red-marked dots are placed at the cavity-dip points with the same wavelength, hinting that the cavity thickness after the first epitaxial growth is correct.*

5.2.2 Cavity-Dip

After the growth of a half-VCSEL structure, tunnel junction is structured in the sample to form the current confinement aperture. But the realization of a complete GaSb-VCSEL requires twofold epitaxial growth step, as already mentioned. The incomplete cavity is completed by growing GaSb-layer in the second growth step which facilitates to check the epitaxial growth thickness error again after the overgrowth and necessary action can be taken during the device processing.

The reflectivity spectrum of the VCSEL structure after the overgrowth is measured again. This time the cavity dip in the spectrum should be at the middle of the stopband indicating a correct cavity thickness. This will lead to a optimum device performance by obtaining a maximum bottom mirror reflectivity. Often the cavity dip is found a bit left or right of the middle of the stopband due to the epitaxial growth thickness inaccuracy, hinting a wrong cavity thickness. Fig. 5.3 illustrates the simulated and measured reflectivity spectra of the VCSEL structure after the second growth step. The shift of the cavity dip towards the short wavelength side from the center of the stopband can be observed here, i.e. the cavity becomes thinner compared to the designed thickness. The inaccurate cavity thickness can be corrected by adding some material before the dielectric mirror evaporation.

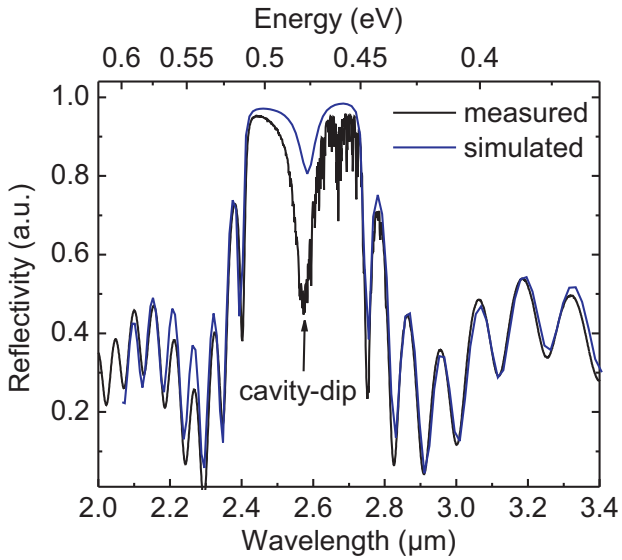

Fig. 5.3: *The measured and simulated reflectivity spectra of the VCSEL structure after the overgrowth and without the top DBR. The cavity dip shifts to the middle of the stopband due to the complete cavity in the structure. A lot of absorption lines around 2.6 μm can be identified in the measured spectrum.*

Before the dielectric mirror evaporation, the reflectivity spectrum is measured once again for the processed VCSEL sample. One part of the processed wafer with a dimension of 3 mm × 5 mm remains unprocessed. Since this unprocessed part have exactly the same condition like a chip in the wafer, one can now obtain the exact cavity thickness information from the cavity dip in the spectrum. The main purpose of this final reflectivity spectrum measurement is to know how much the phase matching layer has to be removed or added before the dielectric mirror evaporation. This information obtained from such final mea-

surement might be different from the one obtained after the overgrowth because of the fact that during the processing some material might be lost from the topmost GaSb layer which can make the cavity a bit thinner, resulting a shift of the cavity dip from the designed wavelength.

5.2.3 Phase-Matching

The cavity mode wavelength has to be located in the region of highest mirror reflectivity to provide lowest threshold gain and it has to appear the long wavelength side of the gain peak since the gain spectrum shifts towards long wavelength as the device heats up. Heating of the active layer is unavoidable in electrically-pumped devices and this effect should be taken into account when the devices are designed and fabricated.

Not only for enhancing the reflectivity for the bottom mirror but also for some other issues like the overlap of the electric field with the active region and with the absorbing tunnel junction layers, the perfect phase matching is extremely important in these long-wavelength lasers. Because the misalignment between the maximum of the electric field and the active region will introduce a reduced effective gain in the device. At the same time, a large overlap of the highly absorbing tunnel junction layers with the electric field introduce a high intracavity absorption losses.

In VCSELs, the resonant mode wavelength critically depends on the cavity optical length and the mirror phase characteristics. If all the epi-layers would be grown exactly to the designed specifications, no separate mode adjustment would be necessary. However due to epi-layer thickness variation during the growth and also around the wafer itself, it is necessary to make mode wavelength adjustments. The most efficient way of adjusting the cavity mode is the changing of the cavity optical length by removing or adding layers with a certain thickness. In GaSb-VCSELs, these adjustments may be performed at the interface of the topmost epi-grown GaSb layer and the first layer of the dielectric mirror. Too large cavity length can be corrected by etching the topmost epi-grown GaSb layers, while correcting too short cavity lengths has to be done by growing an additional layer with the dielectric material, e.g. *a*-Si or SiO_2 before the dielectric mirror evaporation.

5.3 3.4 µm VCSEL Structure Characterization

On the way towards longer emission wavelength, a VCSEL structure at 3.4 µm was designed. After the overgrowth of this structure, PL and reflectivity spectra are measured as displayed in Fig. 5.4 a). PL peak was found at 3346 nm where the cavity dip was at 3370 nm with an offset of 2.7 meV. Note that the cavity dip was not found at the middle of the stopband, i.e. 3.4 µm. This is just due to the thinner cavity resulting from the growth inaccuracy during the overgrowth. However, the cavity thickness can be adjusted during the device processing in order to shift the cavity resonance to the right wavelength. It is also expected that the active region emission during laser operation shifts to the lower energy side by 3-4 meV due to internal heating.

The multi-QW (MQW) active region used in this structure consists of five 11 nm-thick $Ga_{0.43}In_{0.57}As_{0.29}Sb_{0.71}$ type-I quantum wells, confined in 10 nm-thick $Al_{0.3}Ga_{0.3}In_{0.4}As_{0.4}Sb_{0.6}$

quinternary barriers to obtain an emission near 3.4 µm at RT. The crystalline perfection of this sample was studied by HRXRD. Fig. 5.4 b) shows an XRD measurement of the VCSEL after the overgrowth. The peaks arising from the quantum wells of the active region and the signal from the TJ can clearly be seen, proving the good material quality. A series of satellite peaks originating from the quantum well/barrier periodicity can be observed here. As can be seen, the satellite peaks appear narrow and intense, and one can observe the presence of clearly resolved Pendellösung fringes indicating the smooth interfaces and the high crystalline perfection.

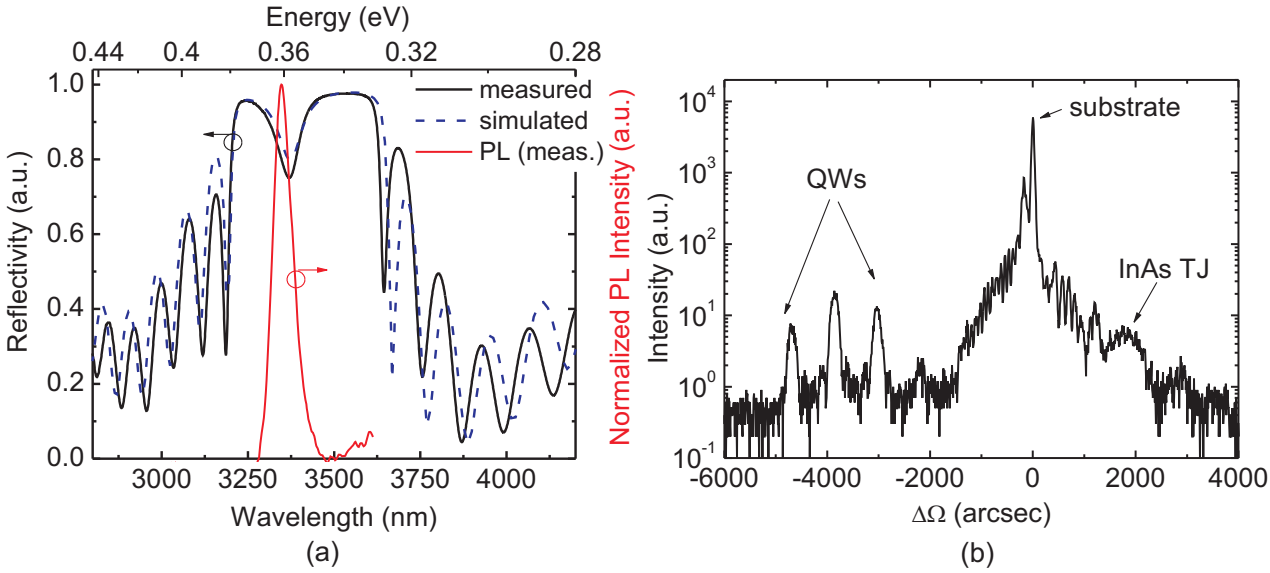

Fig. 5.4: *a) The measured and simulated reflectivity spectra of the 3.4 µm VCSEL structure after the overgrowth and without the top DBR. The cavity resonance occurs at the left side of the stopband middle, yielding a thin cavity due to growth inaccuracy, b) X-ray diffractometry measurement of 3.4 µm VCSEL after the overgrowth. The peaks from QWs can be clearly identified.*

5.4 Material Data for GaSb-VCSELs

For designing and analyzing GaSb-based VCSELs, it is of great importance to have the accurate knowledge of the refractive indices and their variation with wavelength for all epitaxial and dielectric layers used in the device structure. The refractive index dispersion data of epi n-GaSb and n-AlAsSb layer with a doping concentration of $n = 5 \times 10^{17}\,\mathrm{cm}^{-3}$ has already been measured and discussed in [59]. The refractive indices of dielectric mirror materials, i.e. a-Si/a-Ge and SiO_2 used in GaSb-VCSELs for the wavelength regime from 2.3 µm to 5 µm will be presented here. Then the dependence of absorption coefficient α on wavelength for a-Si and a-Ge materials will be reported.

5.4.1 Refractive Index

The variation of the refractive index with wavelength for a-Si and a-Ge material was determined experimentally in the mid-infrared wavelength regime using the method described in [99]. According to this method, a layer of unknown refractive index should be deposited on

a substrate of known refractive index. By measuring the wavelength dependent reflection spectra of this Fabry-Pérot etalon structure, one can determine both the refractive index and the geometric thickness of the layer. In this thesis, an approximately 1 µm thick e-beam evaporated *a*-Si, *a*-Ge and SiO_2 layers were deposited on an InP substrate to determine the refractive index in the energy range from 0.25 eV to 0.55 eV, as displayed in Fig. 5.5.

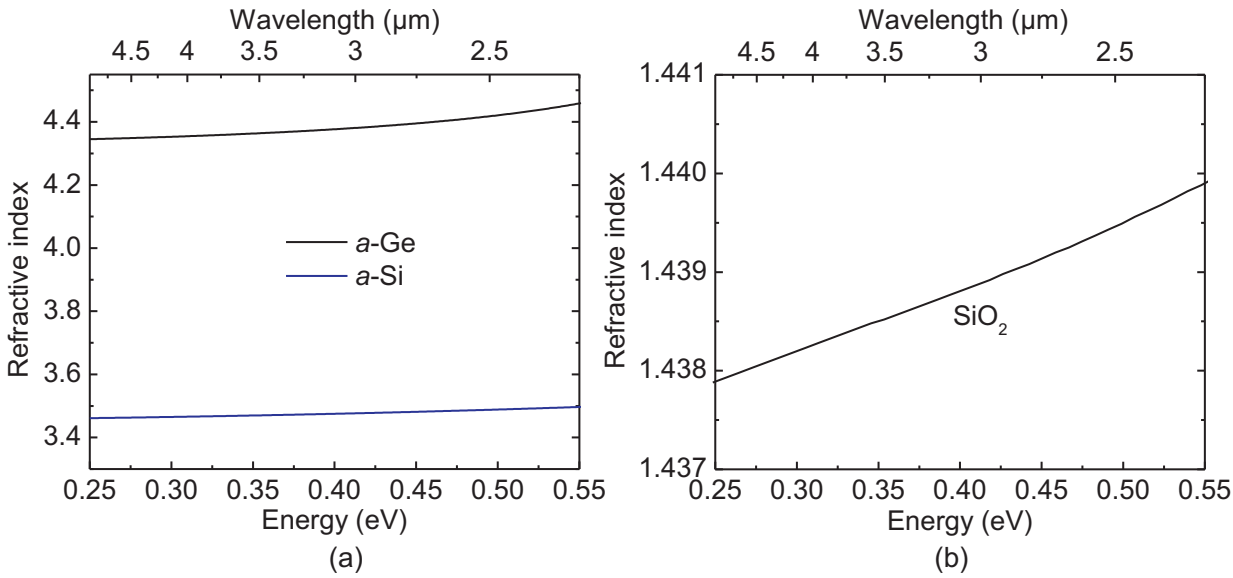

Fig. 5.5: *Refractive index dispersion data in the mid-infrared wavelength regime for a) a-Ge and a-Si and b) SiO_2 materials.*

5.4.2 Absorption

To measure the absorption coefficient of these dielectric materials, i.e. *a*-Si or *a*-Ge films were deposited on a transparent quartz glass substrate by e-beam evaporation at a base pressure of 10^{-6} mbar. The film thickness of *a*-Si and *a*-Ge films was 1038 nm and 1052 nm, respectively. The thickness was determined by Dektak surface profilometer. The schematic of a thin film on a transparent substrate is illustrated in Fig. 5.6. The film has thickness d and complex refractive index $\bar{n} = n - \mathrm{i}\kappa$, where n is the real part of the refractive index and κ the extinction coefficient which can be expressed by in terms of absorption coefficient

$$\kappa = \frac{\alpha\lambda}{4\pi} \tag{5.1}$$

To measure the absolute values of the absorption coefficient for energies around the absorption edge, a standard transmission measurement using ultraviolet-visible (UV/VIS) spectrometer is performed. Below the bandgap, the absorption is superimposed by interference fringes due to different refractive indices of film and substrate. For the region of weak absorption, the absorption signal is at the noise level of the spectrometer. So, it is not possible to determine the absorption coefficient from UV/VIS measurements which forces us to apply the highly sensitive photothermal deflection spectroscopy (PDS) [100] measurement in weak absorption region ($\alpha d < 1$). But α values in this method are relative ones which is calibrated by shifting the PDS spectrum to transmission spectra in the region of spectral overlap. Thus PDS in combination with UV/VIS transmission spectroscopy was

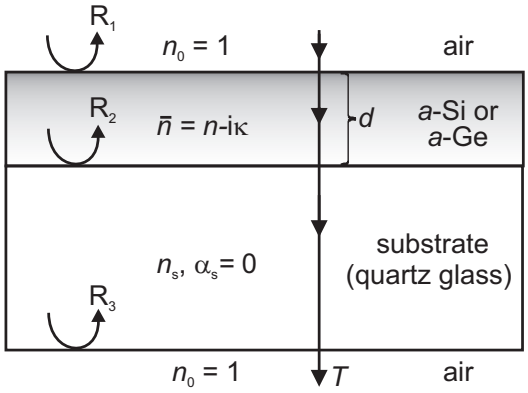

Fig. 5.6: *System of an absorbing a-Si/a-Ge layer on a thick finite transparent quartz glass substrate.*

used to determine the absorption coefficient as a function of wavelength as displayed in Fig. 5.7.

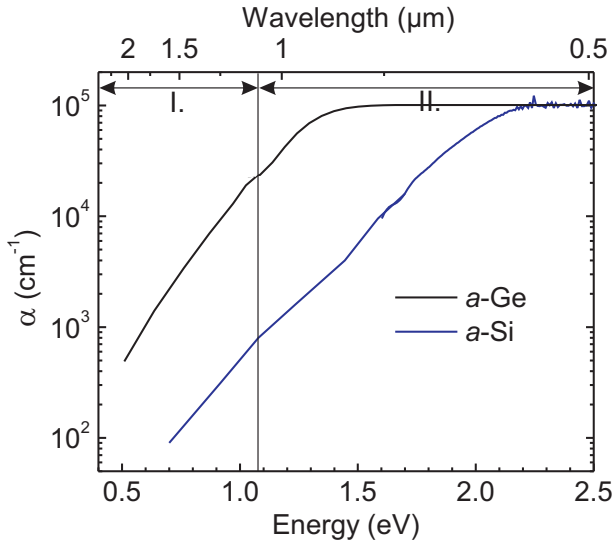

Fig. 5.7: *Spectral dependence of absorption coefficient for a-Ge and a-Si in the mid-infrared wavelength regime. Region I and Region II are obtained by PDS and transmission measurement, respectively. Due to the limited sensitivity of the UV/VIS spectrometer and the saturation of the PDS signal, the absorption coefficient cannot be determined in the range of high absorption.*

The value of α was calculated from the transmission data using the procedure described in [101]. All the reflections at three interfaces have been taken into account while calculating α from transmissivity spectrum. The calculation of α from the standard transmission measurement. The absorption coefficient α is given by [101]

$$\alpha = -\frac{1}{d} \ln \left(\frac{1}{B} \{ A + [A^2 + 2BT(1 - R_2 R_3)]^{1/2} \} \right) \tag{5.2}$$

where

$$A = -(1 - R_1)(1 - R_2)(1 - R_3) \tag{5.3}$$

$$B = 2T(R_1R_2 + R_1R_3 + 2R_1R_2R_3) \tag{5.4}$$

$$R_1 = \left(\frac{n-1}{n+1}\right)^2 \tag{5.5}$$

$$R_2 = \left(\frac{n-n_\mathrm{s}}{n+n_\mathrm{s}}\right)^2 \tag{5.6}$$

$$R_3 = \left(\frac{n_\mathrm{s}-1}{n_\mathrm{s}+1}\right)^2 \tag{5.7}$$

T is the transmittance and R_1, R_2 and R_3 are the intensity reflection coefficients of the air-film, film-substrate, and substrate-air interfaces, respectively. The range of validity of these formulas is limited to the region where no interference fringes are observed ($\alpha d > 1$).

6 GaSb-Device Results

Having already discussed about the device design and manufacturing process, here comes the VCSEL characterization now. In this chapter, the experimental characterization of the electrical, optical and thermal properties of GaSb-based BTJ VCSELs will be reported. Most of the results will be presented for those laser structures designed for the emission wavelength of 2.6 µm. An application-based results proving the suitability of such lasers in gas sensing will be presented at the end of this chapter. This chapter will be concluded by the device results designed for VCSELs at a record long emission wavelength of 3.4 µm.

6.1 GaSb-VCSELs at 2.3 and 2.6 µm

6.1.1 Electrical Characteristics

In general, the electrical characteristics for VCSELs utilizing low bandgap material system is a subject of considerable interest, especially for laser devices aimed for CW operation. This holds well for antimonide VCSELs which should have a reasonably low electrical resistance leading to a reduced joule heating. In addition, in apertured VCSELs, current confinement is very critical for the desired device features, e.g. true single-mode operation and a reduced threshold current yielding a CW operation. In the following, the experimental results on the dc current-voltage (I-V) measurements as well as the current confinement efficiency in GaSb-based BTJ VCSELs emitting at 2.6 µm will be presented and analyzed.

6.1.1.1 Current-Voltage Characteristics

An HP 4142B semiconductor parameter analyzer with a high power source/monitor unit was used to measure the electrical characteristics of the devices. This electrical characterization will mainly include the analysis of the VCSEL series resistance and its dependence on the BTJ aperture diameter utilizing current-voltage (I-V) characteristics. In general, as compared to other semiconductor laser diodes, VCSEL exhibit high series resistances owing to the presence of several device components, for instance in devices under study, the heterojunction barriers of the multiple DBR interfaces, tunnel junction, spreading resistance due to the current confinement by the aperture in addition to top p-side and n-side contact.

To obtain a value for series resistance R_s, two methods were used. The first method considers the deviation of the $\log(I) - V$ curve from linearity at high currents allows to determine R_s according to

$$\Delta V = I R_\mathrm{s} \tag{6.1}$$

where ΔV is the amount of voltage deviation from the linear region at a laser driving current of I.
To confirm the value of R_s, the second method utilizes the following equation [102]

$$I \frac{\mathrm{d}V}{\mathrm{d}I} = I R_\mathrm{s} + \frac{\eta k_\mathrm{B} T}{q} \tag{6.2}$$

The term $I\mathrm{d}V/\mathrm{d}I$ is linearly related to I with a slope equal to R_s and an intercept with y-axis at $I = 0$ equal to $\eta k_\mathrm{B}T/q$, where η is the ideality factor. As known, the derivative $\mathrm{d}V/\mathrm{d}I$ above threshold is determined by R_s. Therefore, at the lasing threshold, the term $I\mathrm{d}V/\mathrm{d}I$ should decrease rapidly from $IR_\mathrm{s} + \eta k_\mathrm{B}T/q$ to IR_s.

Fig. 6.1 illustrates the experimentally observed variation of $I\mathrm{d}V/\mathrm{d}I$ with current along with the corresponding light-current (L-I) characteristics for a VCSEL with $D_\mathrm{BTJ} = 6\,\mu\mathrm{m}$. The

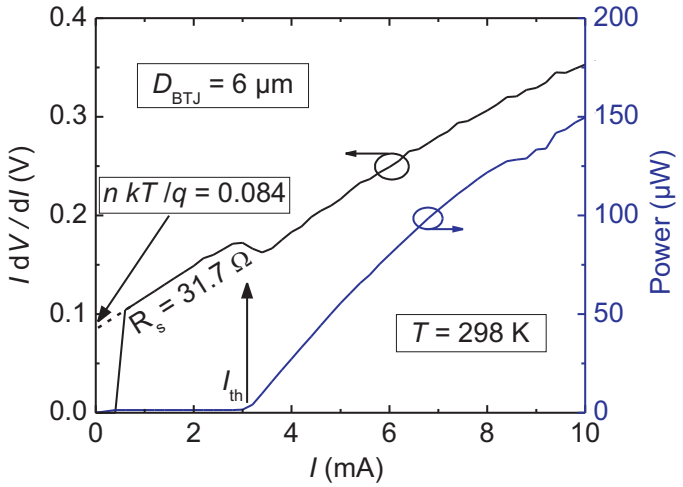

Fig. 6.1: *$I\dfrac{\mathrm{d}V}{\mathrm{d}I}$ versus I and L-I characteristics for a VCSEL with $D_\mathrm{BTJ} = 6\,\mu m$, indicating voltage saturation at I_th.*

values of R_s and η have been extracted to $31.7\,\Omega$ and ≈ 3.2, respectively. The value of ideality factor $\eta > 2$ suggests that the series resistance is distinctly influencing device performance. It should be stressed that this method is strictly valid only below lasing threshold and without the stimulated emission process [103].

The I-V characteristics of BTJ VCSELs for different aperture diameters are shown in Fig. 6.2 a). It is seen that the slope of the I-V curve decreases with the increase in BTJ aperture diameter, hinting thereby a reduction in series resistance. The variation of R_s as a function of BTJ aperture diameter is shown in Fig. 6.2 b). The inverse dependence of series resistance on VCSEL aperture size is due to the increased size of the conductive cross-sectional area, which is in agreement with Ohm's law. Due to inhomogeneous current supply resulting a current crowding effect near the aperture in top-emitting VCSELs, R_s approximately scales as $R_\mathrm{s} \propto D_\mathrm{BTJ}^{-1}$, as expected [104].

The series resistance R_s increases from $12\,\Omega$ at $D_\mathrm{BTJ} = 20\,\mu\mathrm{m}$ to $40\,\Omega$ at $D_\mathrm{BTJ} = 5\,\mu\mathrm{m}$ with the decrease of BTJ aperture diameter. Note that in Fig. 6.2 b), R_s amounts to $29\,\Omega$ for $6\,\mu\mathrm{m}$ VCSEL determined by Eqn. 6.1, which is in good agreement with the value obtained by derivative method.

One clearly recognizes the moderately low resistive device design of $2.6\,\mu\mathrm{m}$ VCSELs. For instance, the threshold voltage V_th is $0.66\,\mathrm{V}$ for the $6\,\mu\mathrm{m}$ diameter VCSEL presented here whereas the photon energy is $0.47\,\mathrm{eV}$. The rest of the voltage drop at threshold comes

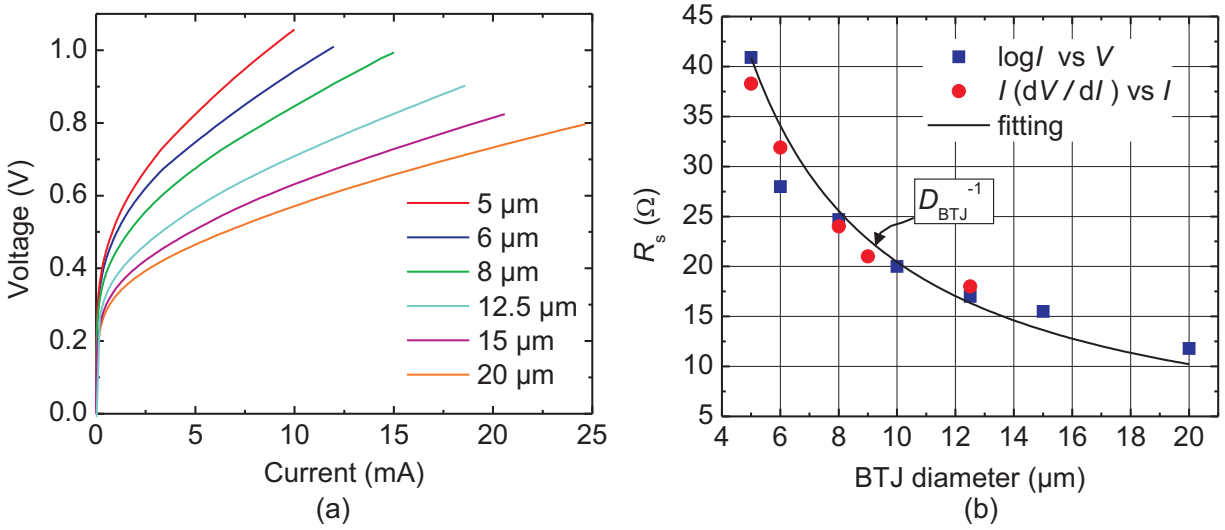

Fig. 6.2: *a) VCSEL operating voltage versus applied current for BTJ aperture diameters between 5 µm and 20 µm. Measurements were performed in CW at 25°C b) Measured series resistance R_s as a function of BTJ diameter by two different techniques.*

across several device components outside the active region, e.g. top p-side contact, BTJ, top lateral current spreading layer for the annular contact, 500 µm thick n-doped substrate, n-side contact and heterojunction barriers of the multiple DBR interfaces.

In order to justify the contribution of voltage drop from the top p-side contact, the transmission line measurement (TLM) [105] concept was used. The TLM test structures processed in the same VCSEL wafer were used in this case, provided that the mask set included TLM patterns. The measurement was carried out by two-point probe technique. Fig. 6.3 shows the schematic view of the measurement procedure and the test structures used where d is

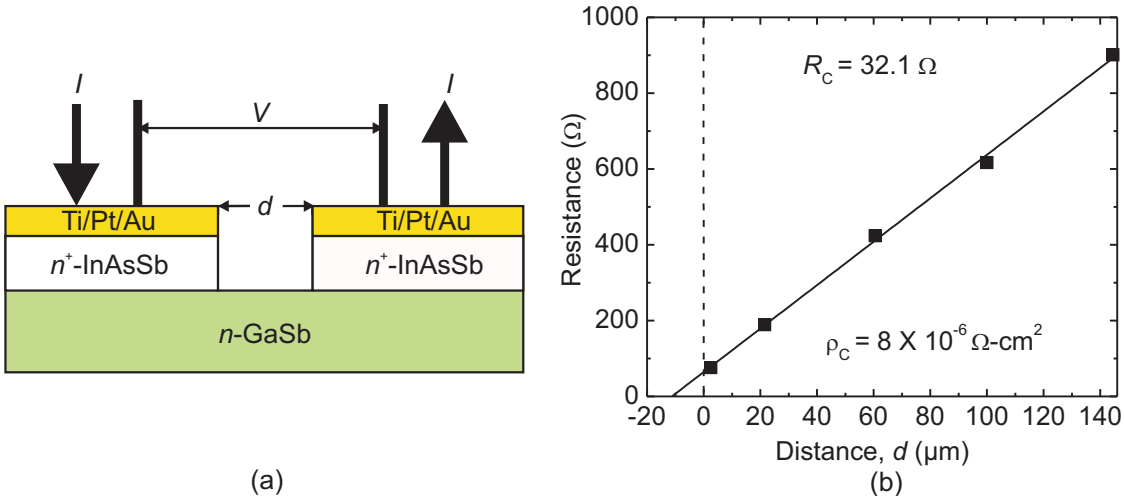

Fig. 6.3: *a) TLM measurement and the structures used in measuring the contact resistivity, b) Extraction of top contact resistance by TLM.*

the contact pad spacing and R_c is the resistance due to the contact. The contact resistivity

ρ_c was found to be as low as $8 \times 10^{-6}\,\Omega\,cm^2$, being sufficiently low resistive in devices for CW operation. Considering this resistivity value, the voltage drop at threshold for the top p-side contact can be calculated to be 4 mV.

Taking the TJ contact resistivity measured in Chap. 3, the voltage drop at BTJ can be calculated to be 24 mV. The voltage drop due to lateral current spreading amounts to 12 mV by using Eqn. 3.6. The rest of the voltage drop can be attributed to across resistance due to backside n-doped substrate, n-side contact and heterojunction barriers of the multiple DBR interfaces. The latter is dominating in such devices, despite the fact that the current spreads out in the bottom mirror.

6.1.1.2 Current Confinement Efficiency

The current confinement efficiency was checked for VCSELs at 2.6 µm by utilizing the test structures in the same processed sample. This is demonstrated in Fig. 6.4, where the current density for a test structure with D_{pc} = 23 µm BTJ is compared with an equally large blocking region (see Fig. 3.21). As can be clearly seen in Fig. 6.4, the current densities of the BTJ are more than four orders of magnitude larger than for the blocking region with reverse-biased p^+n region and several kA/cm^2 are achieved at an applied voltage as low as 1 V. Also marked in Fig. 6.4 are these J-V characteristics of test structures are measured by varying the temperature. Evidently, the blocking and conducting properties in VCSELs do not deteriorate with increasing temperature. In other words, the current confinement efficiency by BTJ remains same in VCSELs operated at higher temperatures.

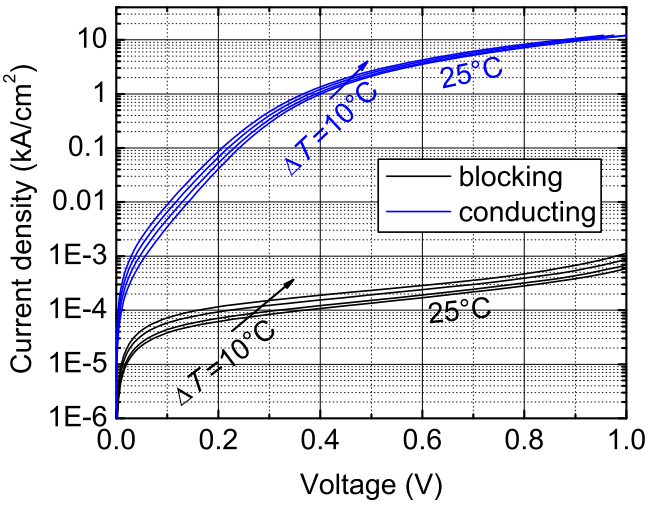

Fig. 6.4: *Temperature dependent J-V characteristics of the test structures with D_{pc} = 23 µm representing device central part with BTJ and outer part without BTJ in order to show the current confinement efficiency in 2.6 µm VCSELs.*

6.1.2 Optical Characteristics

After the electrical characterization, now the optical properties of BTJ VCSELs at 2.6 µm including spectral properties and tuning behavior will be described in details. These properties will demonstrate the suitability of VCSEL lasers as light sources for gas sensing applications.

6.1.2.1 Light-Current Characteristics

CW light-current (*L-I*) characteristics of devices with three different aperture diameters of 5, 5.5 and 6 µm were measured at room temperature as displayed in Fig. 6.5. These measurements were carried out on a water-cooled copper heatsink. The temperature of the heatsink was controlled by thermostat. A Peltier-cooled InAs photodetecctor from Judson Technologies with cutoff wavelength around 3.5 µm was used to detect the light.

The threshold currents of 5, 5.5 and 6 µm devices are 1.46, 3.3 and 4.5 mA, respectively. The lowest effective threshold current densities among these three devices was found to be as low as 2.6 kA/cm^2, where lateral carrier diffusion of 1.7 µm on each side of the BTJ is taken into account. The details of the experimental determination of carrier diffusion length will be discussed in Subsect. 6.1.2.7. Several dips in *L-I* characteristics of Fig. 6.5 is due to the presence of water vapor absorption lines in the device-working regime. The rollover peak power of 0.5 mW has been reached in the device with $D_{\mathrm{BTJ}} = 6\,\mu\mathrm{m}$, yielding a differential quantum efficiency of 10.4%. The temperature dependent *L-I* characteristics of a device

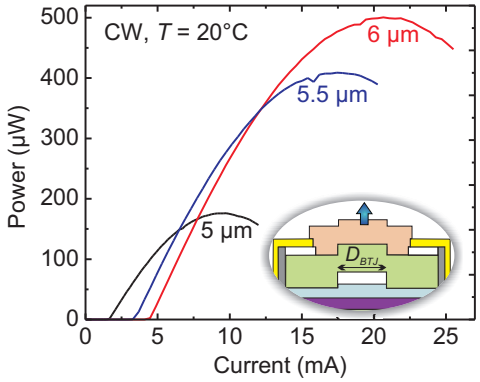

Fig. 6.5: *Output (L-I) characteristics of GaSb-based VCSEL with different BTJ diameters. Schematic of the VCSEL with a label for aperture diameter as inset.*

with $D_{\mathrm{BTJ}} = 6\,\mu\mathrm{m}$ are presented in Fig. 6.6 a). The device shows CW operation up to 55°C heatsink temperature. The rollover peak power of this device obtained at RT (i.e. 25°C) is 0.3 mW, yielding a differential quantum efficiency of 9.6%. At RT, the threshold current I_{th} is 3.9 mA, corresponding to an effective threshold current density of around 5.6 kA/cm^2.

The dependence of the threshold current and maximum output power as a function of the heatsink temperature is displayed in Fig. 6.6 b). As can be seen the maximum output power in the device decreases roughly linearly with increasing temperature as expected. But the

threshold current increases with increasing temperature and the minimum threshold current is located at a temperature below -20°C.

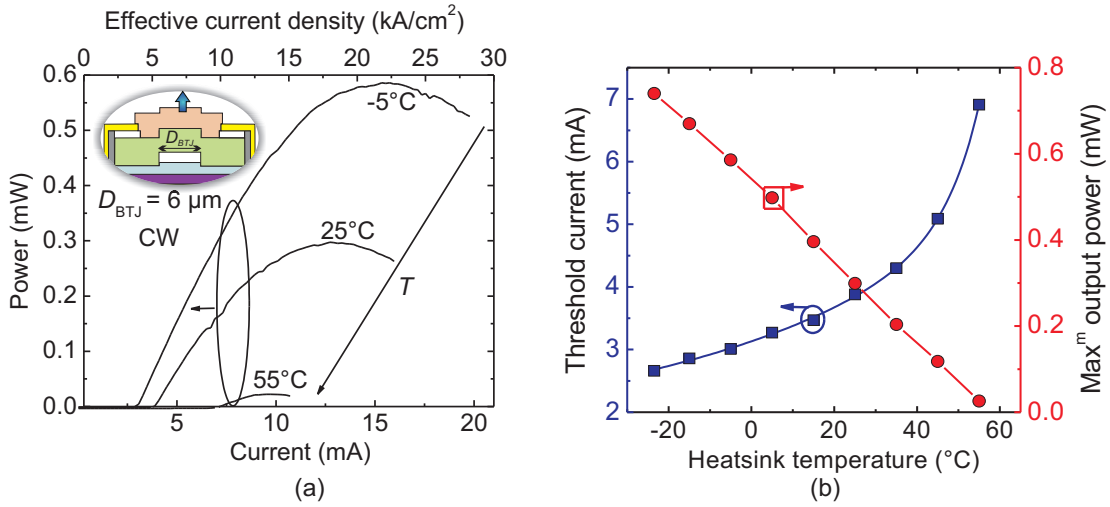

Fig. 6.6: *a) Temperature dependent L-I characteristics of 2.6 µm BTJ-VCSEL. b) Threshold current and maximum output power against heat sink temperature* T_{hs}

6.1.2.2 Lasing Spectra

Emission spectra of VCSEL lasers were measured with a Vertex 70 (Bruker Optics GmbH) and a Peltier-cooled extended InGaAs detector. The measured spectral lasing linewidths are limited by the resolution of the Fourier transform infrared (FTIR) spectrometer.

Compared to edge-emitting lasers, due to the larger resistive heating and smaller cavity volume of the VCSEL, the wavelength-tuning range and frequency response are significantly larger and faster which is exploited in gas sensing application. The thermal tunability of a VCSEL with $D_{\mathrm{BTJ}} = 7\,\mu\mathrm{m}$ was measured by varying the heatsink temperature T_{hs} at a constant current as illustrated in Fig. 6.7 a). The wavelength tuning range $\Delta\lambda$ of the VCSEL has been measured to be 10 nm. Note that the emission wavelength is found to shift linearly with increasing temperature as displayed in Fig. 6.7 b). As can be seen, the device exhibits single-mode operation over the entire temperature range with a tuning rate of 0.24 nm/K.

The current tunability of the VCSEL was measured by varying the laser driving current at a constant T_{hs}. The emission spectra of the same device at various laser driving currents are displayed in Fig. 6.8 a), yielding distinct single-mode emission across its entire operating range. They show a side-mode suppression ratio (SMSR) of over 25 dB. $\Delta\lambda$ has been measured to be 5 nm. The wavelength shifts at a rate of 0.56 nm/mA.

High tuning rates are very attractive for gas sensing applications since several gas absorption lines may be scanned at a time by the temperature and current-induced self-heating effect.

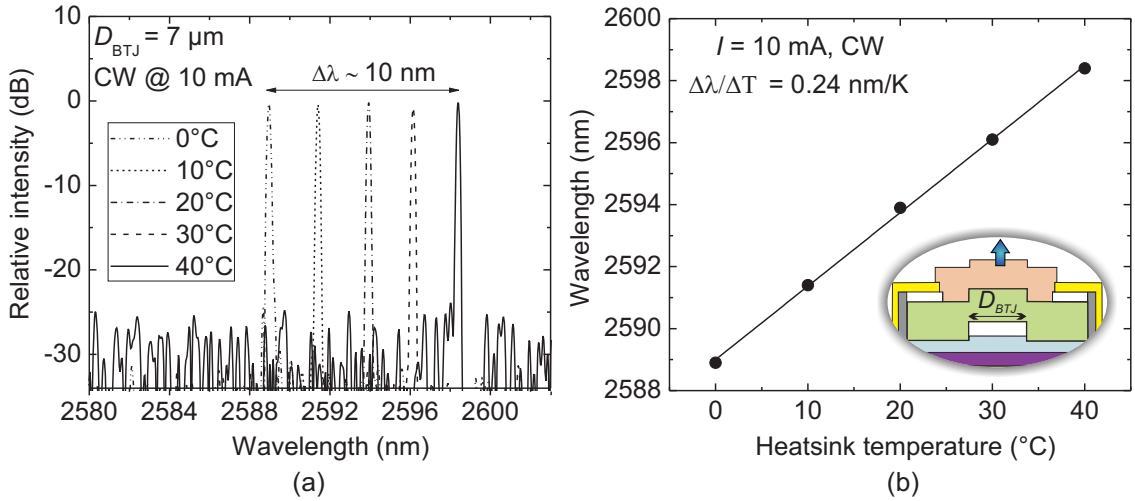

Fig. 6.7: *a) Spectra of VSCEL by varying heatsink temperature at a constant driving current of 10 mA. b) Temperature dependent wavelength variation with a tuning rate of 0.24 nm/K.*

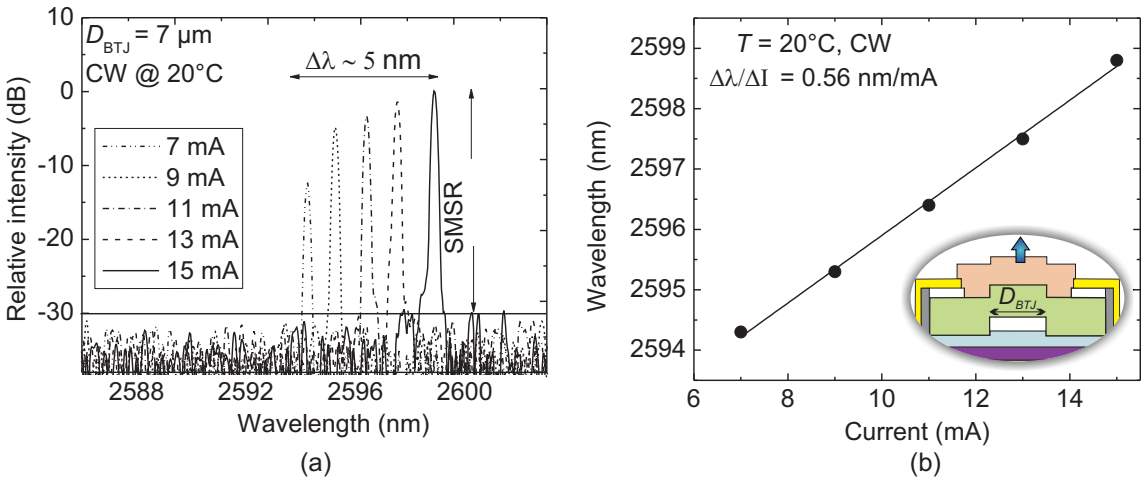

Fig. 6.8: *a) Spectra of VSCEL by varying driving currents at a constant heatsink temperature of 20°C. b) Current dependent wavelength variation with tuning rate of 0.56 nm/mA.*

6.1.2.3 Subthreshold Spectra

The VCSEL's spectra in subthreshold regime provides a lot of insight information of the device, such as waveguiding behavior, cavity loss [106], bandfilling effect, carrier distribution under pumping condition etc. By having a knowledge on these properties, one can evaluate the performance for devices under study and then possibly make an optimum design for next generation devices.

Subthreshold emission spectra of the devices were measured with a Vertex 70 (Bruker Optics GmbH) and a RT operating extended InGaAs detector. Measuring subthreshold spectra is a bit challenging due to the low optical power from the device at a current below

threshold. One has to use a long integration time on the FTIR spectrometer in order to get a decent and reasonable subthreshold-spectra of the device.

As known, for a given size, VCSEL exhibits many transverse modes in sub-threshold amplified spontaneous emission spectra even in small-size devices while only the fundamental mode reaches threshold. Such modes in subthreshold regime are also referred to as "cold-cavity" modes. This is just because of the fact that these modes are not affected by the optical gain or spatial hole burning which facilitates to measure the device aforementioned properties in an accurate way. Since the carrier density is clamped above threshold, the observed redshift of the resonance wavelength is due to heating of the active layer and mirrors.

Fig. 6.9 a) displays the resonance wavelength for fundamental mode at below- and above-threshold regime of the device with a BTJ aperture diameter 9 µm. The *L-I*-characteristics (as shown in inset) and driving current dependent optical emission spectra of that device has been measured in CW at a heatsink temperature of 20°C. Above threshold, the current tuning rate has been found to be 0.52 nm/mA, assuming a linear dependence of the resonance wavelength on the laser current. On the other hand, below threshold the observed wavelength shift is not only due to the heating but also a change in population inversion condition so-called bandfilling effect. By considering the current-induced heating effect, the bandfilling alone leads to a shift of the resonance wavelength of $\Delta\lambda_{\mathrm{bf}} \approx 2.9$ nm or $\Delta\lambda_{\mathrm{bf}}/\lambda_{\mathrm{cav}} \approx 0.12\%$, where λ_{cav} is the cavity resonance wavelength. In Fig. 6.9 b) one optical emission spectrum is shown for the same VCSEL operating in the subthreshold region at a current of 2.1 mA. From the spectral measurement of Fig. 6.9 b) we can clearly identify the wavelength of different modes. The label "1st" indicates the fundamental mode, "2nd" the second order mode, and "3rd" the third order mode and so on.

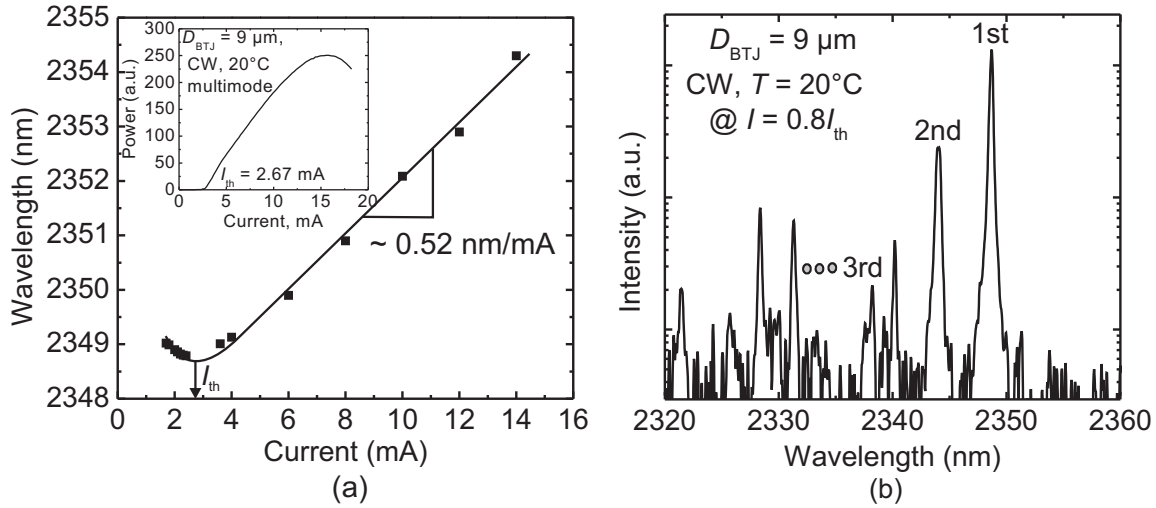

Fig. 6.9: *a) Resonance wavelength for the fundamental mode as a function of laser current in both below and above threshold regions. L-I characteristics for VCSEL with emission at 2.35 µm is shown in the inset. b) subthreshold spectrum for VCSEL driven at 2.1 mA, whereas* $I_{\mathrm{th}} = 2.7\,mA$

6.1.2.4 Cavity Mode Adjustment

One of the advantages of using dielectric top mirror in GaSb-based BTJ VCSELs lies in the capability of compensating for thickness inaccuracies in the epitaxial growth of the cavity. Due to the twofold epitaxial growth in presented VCSELs, such thickness inaccuracy could appear again during the overgrowth. In addition, during the device processing, losing some material could introduce additional uncertainties in the cavity length, i.e. cavity resonance wavelength. Fig. 6.10 shows the reflectivity spectra of the top and bottom Bragg mirror and the lasing spectra of VCSEL. The emission wavelength of 2.5 µm clearly tells that there is a growth error in the cavity thickness since the VCSEL structure was designed for 2.6 µm. Such an error makes an off-resonance from the bottom mirror reflectivity maximum. This can be compensated through the addition of cavity extension layer, e.g. *a*-Si layer with a certain thickness between the dielectric mirror and the laser cavity. This kind of correction shows the power of using dielectric mirror to complete the inner cavity at the last step of the processing.

Devices emitting at 2.6 µm show a much better performance in terms of threshold current, output power and maximum CW operating temperature compared to 2.5 µm devices. As can be seen in Fig. 6.10, the laser emission at 2.6 µm is well-aligned with the center of the stopband, having a maximum reflectivity. So, an appropriate thickness of *a*-Si layer was deposited on top of the device as a part of the cavity to shift the cavity dip position to 2.6 µm. On the way towards long emission wavelength, thus the maximum wavelength achieved is 2.63 µm which is the longest wavelength ever reported for any GaSb-based single-mode VCSELs operating in CW. Devices emitting at other wavelengths apart from the designed wavelength (2.6 µm here) exhibit worse performance due to the following reasons:

- Lower bottom mirror reflectivity, resulting a high threshold gain
- Decreased Γ_r^{act} due to a poor overlap of the electric field with the active region
- Increased Γ_r^{BTJ} due to a better overlap of the field with the tunnel junction layers

6.1.2.5 Transverse Mode Characteristics

The transverse mode characteristics of GaSb-based BTJ VCSELs emitting at 2.3 and 2.6 µm were extensively studied, both theoretically and experimentally. Such an extensive analysis presented in the following provides insight into the control of transverse mode of VCSELs under study. As mentioned earlier, the optical index guiding in the devices is achieved by an effective refractive index step due to the presence of a laterally structured BTJ in the cavity.

All lasing modes in VCSELs of different active diameters are experimentally measured. Then the experimental results are compared against the theoretical data for two different VCSEL designs for 2.3 and 2.6 µm, yielding a good agreement. VCSELs at 2.6 µm with 9 µm BTJ aperture diameter show single-mode emission over the entire operating range. This single-mode behavior from large-aperture device results from a reduced step height caused by a thinner tunnel junction compared to 2.3 µm VCSELs which eventually lead

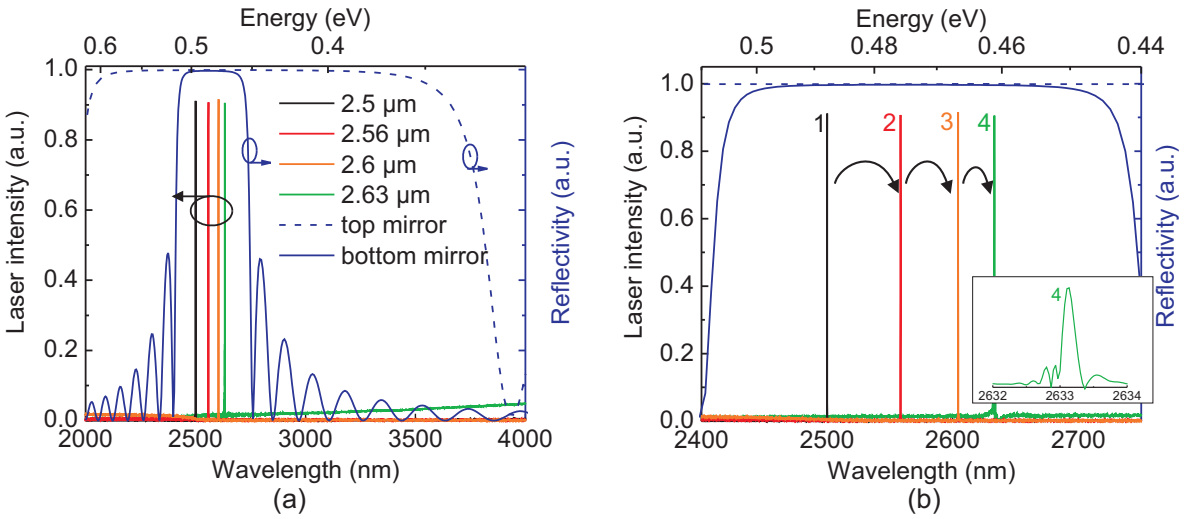

Fig. 6.10: *a) Shifting the laser emission wavelength to longer wavelength by increasing the cavity length through a-Si layer. The reflectivity spectra of top and bottom mirror are shown as well, b) Zoomed-in view of the reflectivity spectrum of the bottom mirror in its stopband regime and CW operating single-mode lasing spectra, 1)* T_{hs} *= 10°C,* I *= 14 mA,* D_{BTJ} *= 7.5 µm, 2)* T_{hs} *= 15°C,* I *= 12 mA,* D_{BTJ} *= 5.5 µm, 3)* T_{hs} *= 24°C,* I *= 17 mA,* D_{BTJ} *= 8 µm, and 4)* T_{hs} *= -6°C,* I *= 13 mA,* D_{BTJ} *= 8 µm.*

to a weaker optical index guiding in the device. The transverse mode spacing between the excited modes is also determined and the results are compared with the theory. The far-field patterns ensure that devices with reasonable aperture diameters operate in single fundamental LP_{01} mode, showing that the devices are well-designed. The analysis also indicates that single-mode behavior from large aperture devices can be further improved with a further reduction of the step height of the tunnel junction. These developments in such an easy control of transverse modes can significantly advance the use of BTJ-VCSELs with greater reliability for a number of sensing applications.

- **Emission spectra**
  Fig. 6.11 a) displays the output characteristic and the current dependent CW spectra of a 9 µm GaSb-based BTJ VCSEL with an emission wavelength of 2.3 µm at a heatsink temperature of 20°C. The device exhibits multimode operation. Beside the fundamental mode at around 2.35 µm, also LP_{11}, LP_{21}/LP_{02}, LP_{31}/LP_{12} and $LP_{41}/LP_{03}/LP_{22}$ modes can be identified. The identification of these modes is reported here based on the theoretical consideration discussed in Sect. 2.5 and 2.8.

  Output characteristic and current dependent CW spectra for the VCSEL at 2.6 µm with an aperture diameter of 9 µm at 20°C are shown in Fig. 6.11 b), yielding distinct single-mode emission over the entire operating range. The SMSR is over 25 dB. Note that VCSELs at 2.3 µm with 9 µm aperture exhibit multimode emission, whereas 2.6 µm VCSELs with the same aperture show single-mode emission with a good SMSR. This can be mainly attributed to a reduced refractive index step due to the lower step height in 2.6 µm VCSELs, proves the expected device improvement due to the thinner tunnel junction. Though devices at 2.6 µm is benefited a bit in

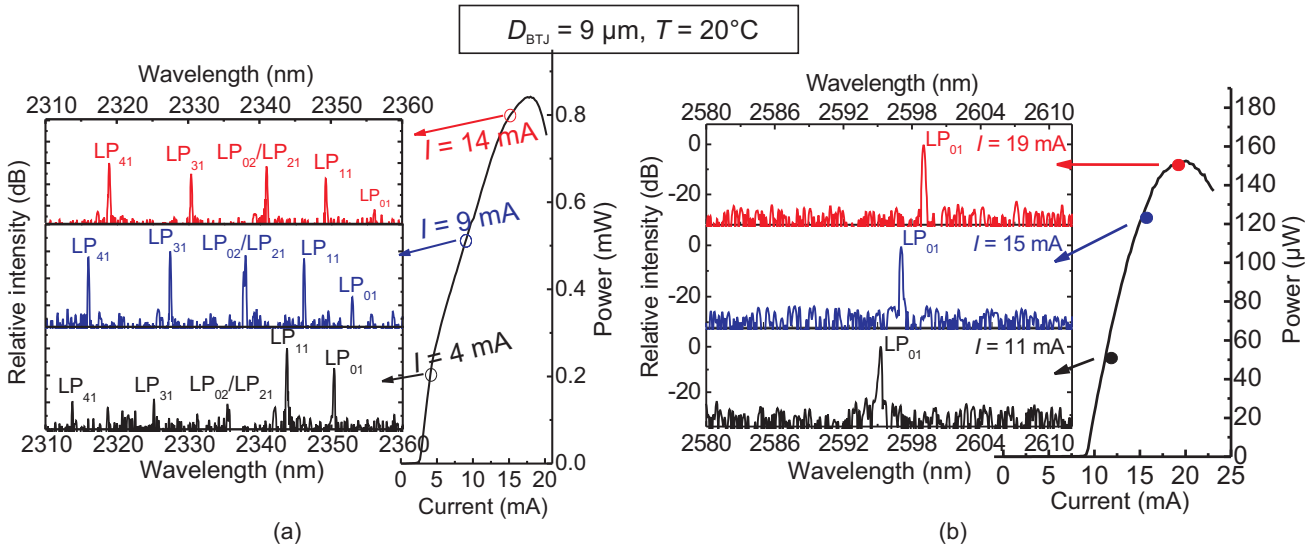

Fig. 6.11: *Output characteristics and driving current dependent spectra at a heatsink temperature of 20°C for VCSELs at:*
a) 2.3 µm with an aperture diameter of 9 µm. The first six transverse modes can be identified. At low currents, LP_{11} is the strongest mode, while at higher currents the higher order modes are dominating. Due to the degeneracy, LP_{21} and LP_{02} are designated as superimposed modes. Similarly, LP_{31} and LP_{12} or LP_{03}, LP_{22} and LP_{41} are degenerated modes which are not mentioned here, figure modified from [59].
b) 2.6 µm. Only LP_{01} mode can be identified, yielding single-mode operation with a SMSR > 25 dB

terms of the single-mode emission also from the longer emission wavelength as can be understood from Eqn. 3.2.

- **Mode and aperture diameter dependent resonant wavelength**
  The mode dependent resonant wavelength can be related to the mode dependent phase parameter B_{lp} via [107]

$$\lambda_{lp} = \lambda_{1D} - \lambda_{1D}\frac{n_C - n_{Cl}}{\langle n \rangle}(1 - B_{lp}) \tag{6.3}$$

where λ_{1D} is the 1D design wavelength and $\langle n \rangle$ being the average refractive index of the laser resonator.

Fig. 6.12 a) shows the measured (extrapolated) and calculated wavelengths for LP_{01}, LP_{11}, LP_{21}/LP_{02} and LP_{31} modes against the BTJ diameters of VCSELs at 2.3 µm. These transverse modes are mentioned here since they appear in this order in a VCSEL. The experimental procedure for the determination of such mode dependent resonant wavelengths of the devices is discussed in [59]. It should also be noted that the lasing wavelength shifts to shorter wavelengths as the transverse cavity dimensions (i.e. BTJ aperture diameter) are reduced. The same behavior is also observed in oxide-apertured VCSELs. The blueshift results because small cavities transform the lasing

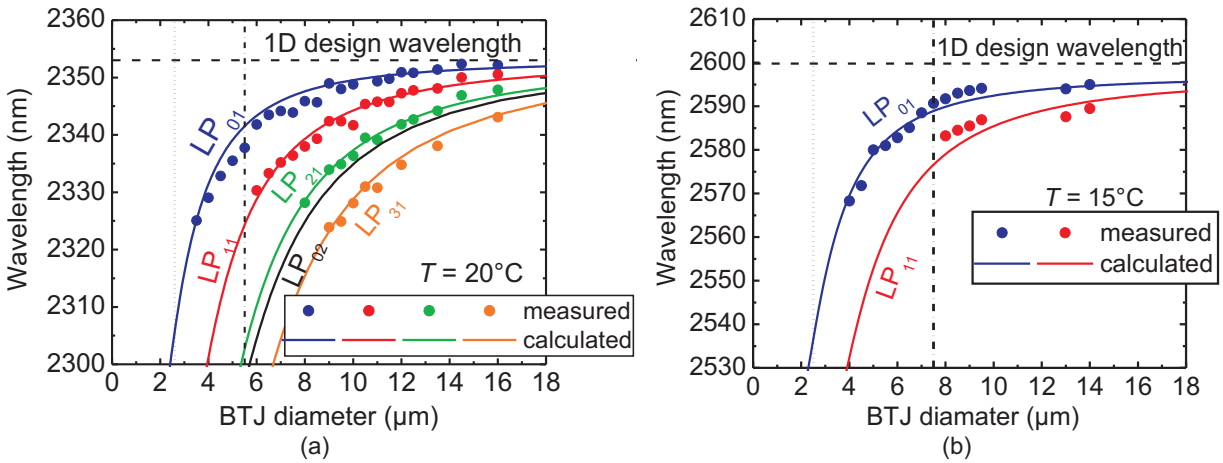

Fig. 6.12: *Extrapolated and calculated wavelengths of LP_{01}, LP_{11}, LP_{21}/LP_{02} and LP_{31} modes according to Eqn. 6.3 against BTJ-diameter of VCSELs at a) 2.3 µm, figure modified from [59] and b) 2.6 µm. Higher order modes are not included here. The horizontal dashed line indicates the 1D design wavelength which is obtained from the one-dimensional transfer matrix method. The theoretical (according to Eqn. 2.30) and experimental single mode cutoff condition for both VCSELs are shown as a vertical dotted line and dashed-dotted line, respectively.*

mode from a plane wave into a true three dimensional mode [42, 108].

The extrapolated wavelengths for the first two LP_{01} and LP_{11} modes against devices with different BTJ diameters are plotted also in Fig. 6.12 b) for VCSELs at 2.6 µm. The measured values are in good accordance with the theory. The strong dependence of the emission wavelength on the aperture diameter in 2.6 µm VCSELs is due to the strong index guiding in the device and the very long emission wavelength. The design of VCSELs for a specific narrow wavelength range therefore requires considering this effect.

There is an obvious deviation of experimental single mode cutoff line (dashed-dotted) from the theoretical line (dotted) in VCSELs under study which is simply due to the aforementioned reason discussed in Sect. 2.9. It is worth pointing out in Fig. 6.12 that the devices with $D_{\mathrm{BTJ}} \leq 5.5\,\mu\mathrm{m}$ for 2.3 µm VCSELs and $D_{\mathrm{BTJ}} \leq 8\,\mu\mathrm{m}$ for 2.6 µm VCSELs will emit in a single fundamental mode with power at least 25 dB above any higher order modes or noise.

- **Transverse mode spacing**
  Fig. 6.13 a) displays the transverse mode spacing between the fundamental mode (LP_{01}) and the first higher order mode (LP_{11}) as a function of the BTJ aperture diameter at constant internal heating for VCSELs emitting at 2.3 µm. Note that the mode spacing values presented here are based on the above-threshold lasing spectra in cw. It is seen that the mode spacing decreases with increasing active diameter of the device due to the fact that the index difference between two adjacent modes

decreases in a large area device. The measured values are in very good agreement with calculated values using Eqn. 2.22. Note that, the transverse mode spacing for a certain aperture diameter in GaSb-based BTJ VCSELs is a bit higher than in GaAs or InP-based VCSELs because of larger emission wavelength and strong index-guiding. Measured values are in the range of 2-12 nm as shown in Fig. 6.13 a).

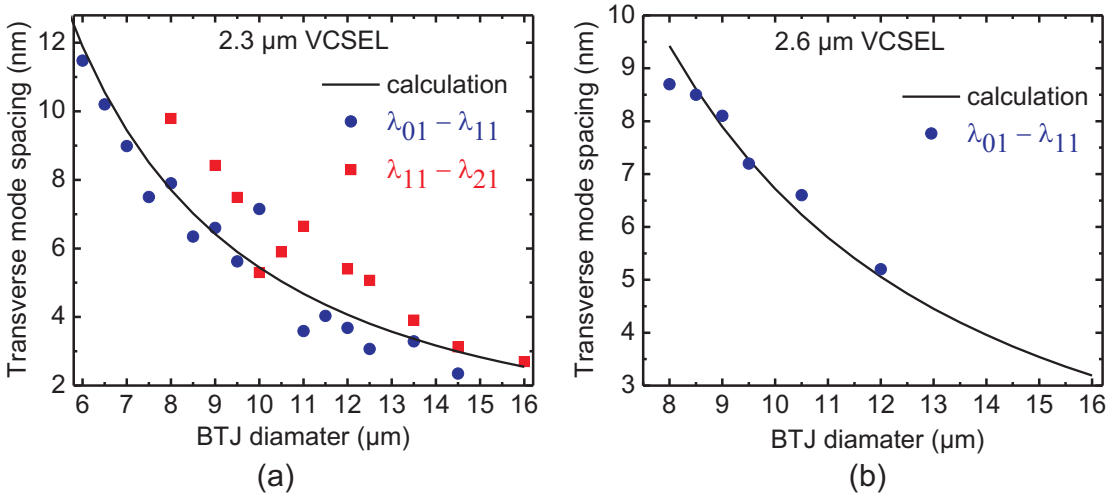

Fig. 6.13: *Wavelength separation between LP_{01} and LP_{11} modes against BTJ diameters based on the lasing spectra above-threshold for VCSELs: a) at 2.3 µm b) at 2.6 µm VCSEL. Separation between LP_{11} and LP_{21}/LP_{02} modes for 2.3 µm VCSEL is also shown . The separation between these modes is calculated by using Eqn. 2.22.*

The mode spacing of VCSELs at 2.6 µm is illustrated in Fig. 6.13 b). Note that the mode spacing should be somewhat larger in 2.6 µm VCSEL than 2.3 µm VCSEL due to the longer emission wavelength of 2.6 µm VCSEL. But the long wavelength effect is a bit outbalanced by lower index guiding in 2.6 µm VCSEL according to Eqn. 2.22.

A further comment should be made about the amount of index guiding in the device which can be estimated from the mode spacing. The well-fit of measured value with the theory indicates that the value of index step we have calculated according to Eqn. 3.2 and Eqn. 3.3 is almost right. In other words, using such experimental data, one can easily calculate the value of the BTJ induced step index by Eqn. 2.22. For instance, with $n_C = 3.4$, $\lambda = 2.35\,\mu m$ and $\Delta\lambda_t = 9\,nm$ (the measured wavelength separation between LP_{01} and LP_{11} mode from Fig. 6.13) for a BTJ-VCSEL of 7 µm aperture diameter emitting at 2.3 µm, the refractive index step n_C-n_{Cl} can be calculated to be 8×10^{-2} which is pretty close to 8.2×10^{-2} we calculated by Eqn. 3.2 and Eqn. 3.3.

6.1.2.6 Far-Field

Far-field measurement was performed at ambient room temperature, in CW operation and on a system with a computer controlled *xyz*-motorized stage. A Peltier-cooled extended

InGaAs detector was kept at a reasonable distance (≈20 cm) from the VCSEL to detect the emitted light. The device emits in a single-fundamental LP_{01} mode with a Gaussian intensity distribution. Due to the rotational symmetric Gaussian beam profile, VCSELs are perfectly suited for simple fiber coupling. Fig. 6.14 a) displays full three-dimensional measured far-field profiles of 2.6 µm GaSb-based BTJ-VCSELs with aperture diameter of 6 µm.

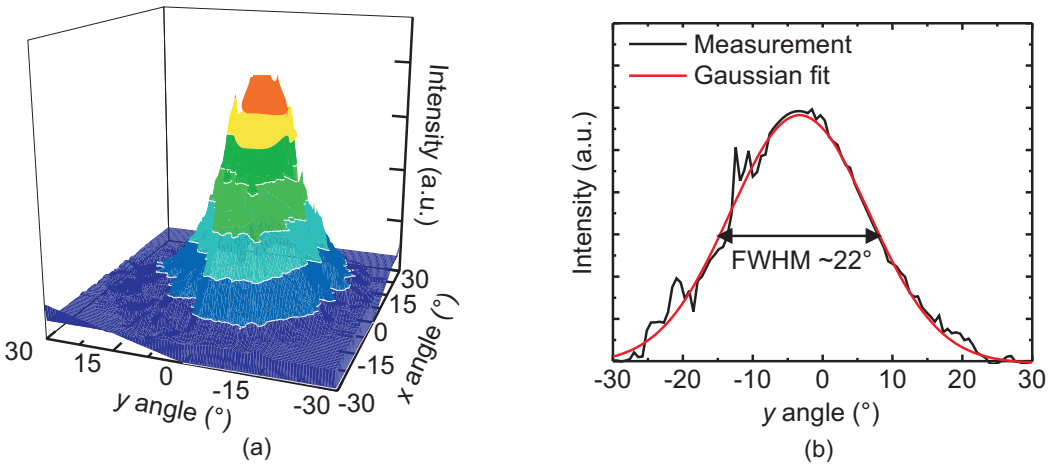

Fig. 6.14: *a) Measured far-field of GaSb-based BTJ-VCSELs at 2.6 µm with an aperture diameter of 6 µm at three times threshold current. This measurement is done at ambient room temperature. b) Measured FWHM far-field angle is 22°C.*

The y-directional far-field profiles of the device is also shown in Fig. 6.14 b) which exhibits a single-lobe pattern with a narrow divergence angle defined by the FWHM angle. Using Eqn. 2.27, this angle is calculated to be 25°. Devices have single intensity peaks also in x-direction (not shown), revealing single transverse mode operating and the good beam quality of the BTJ-VCSEL. It should be noted that, the stronger index guiding in devices under study, compared to GaAs-based oxide-apertured VCSELs, results higher FWHM far-field angles with a certain aperture diameter [109] which can be seen in Fig. 6.14.

6.1.2.7 Carrier Diffusion Length

The threshold current density in any aperture VCSELs is mainly scaled by the current spreading and the lateral carrier diffusion in the active region. Current spreading takes place in the region between the current aperture and the active region. In our BTJ VCSELs, the vertical distance between the BTJ aperture and the active region is roughly 100 nm, so the influence of the current-spreading phenomenon on the threshold current is negligible. Also, if one assumes the thin region below the aperture is low-doped, then the assumption is valid. Hence the threshold current density of the devices under study is mainly governed by the radial carrier diffusion in the active region. It means that the carrier diffusion length needs to be experimentally measured in order to determine the threshold current density accurately. The threshold current I_{th} in VCSELs can be expressed with the threshold current density J_{th} by the following equation:

$$I_{th} = \frac{\pi}{4}(D_{BTJ} + 2r_{diff})^2 J_{th} \propto (D_{BTJ} + 2r_{diff})^2 \tag{6.4}$$

where r_{diff} is the lateral carrier diffusion length. It is evident that I_{th} is proportional to the square of the BTJ aperture diameter plus an extension caused by the carrier diffusion on both sides of the BTJ. Clearly, this is the area of the active region which is being effective pumped during device operation. Fig. 6.15 shows the measured CW threshold current against BTJ aperture diameter for 2.6 µm VCSELs at a constant device internal temperature. In fact, devices with different aperture diameters have different internal heating at constant heatsink temperature. So, it is important to measure the threshold current of

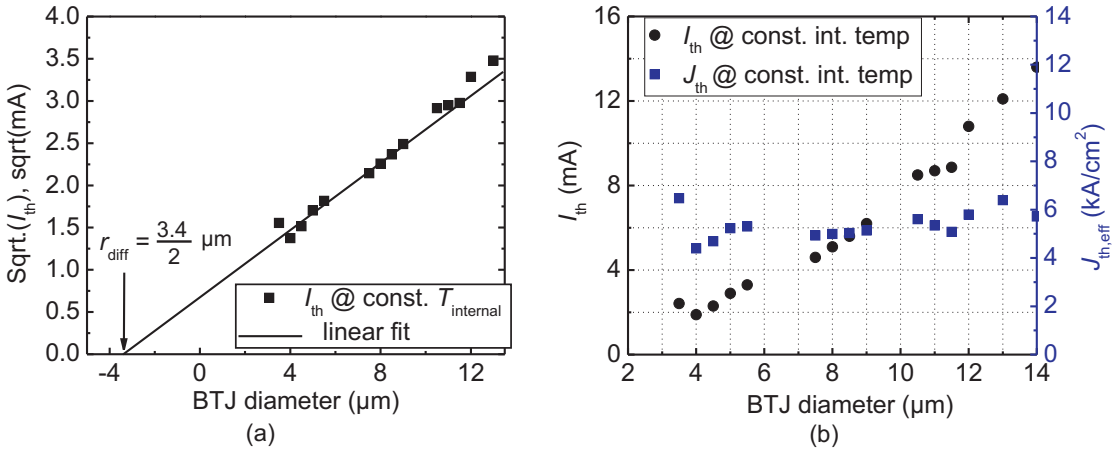

Fig. 6.15: *Square root of the measured CW threshold current at constant internal temperature against BTJ diameter of VCSELs emitting at 2.6 µm. Extracting the carrier diffusion length from a) and taking that into account, the threshold current densities in such devices have been calculated, as displayed in b). The increase of the threshold current in devices with small aperture diameters is due to the high diffraction losses.*

VCSELs at constant internal temperature which is simply the sum of the heatsink temperature and the temperature rise ΔT in the active region of the device at threshold. ΔT value can be obtained by measuring the thermal resistance R_{th} and the applied threshold power P_{th} for each device.

$$\Delta T = R_{\mathrm{th}} \cdot \Delta P_{\mathrm{th}} \tag{6.5}$$

Note that the proportionality behavior indicated in Equation 6.4 is valid up to the device with a certain BTJ diameter since J_{th} starts to increase at small aperture diameters which can be attributed by the diffraction loss present in such devices. By plotting the square root of the threshold current against BTJ diameter, one can calculate the diffusion length from the intercept of the x-axis. A diffusion length of ≈1.7 µm on each side of the BTJ is evaluated in Fig. 6.15 for 2.6 µm VCSELs, being in good accordance with values determined for other BTJ-VCSELs [53]. Once the diffusion length is experimentally determined, the effective threshold current density can be calculated as shown in inset of Fig. 6.15. Note that the minimum of the threshold current has been found at the device size of approximately 4 µm diameter, hinting that these devices are strongly index guided. If the device would be weakly index guided, e.g. implanted VCSELs, the minimum of the threshold current would shift to device with larger aperture diameter where the diffraction loss would start to dominate earlier with decreasing device size [110]. As a matter of fact, the strong index guiding in the GaSb-based BTJ VCSELs is achieved by an high effective refractive index step due to the presence of a laterally structured BTJ in the cavity [111].

6.1.2.8 Maximum CW Operating Temperature

Fig. 6.16 a) shows the maximum CW operating temperature $T_{\max}$ against BTJ diameter ranging from 3.5 µm to 20 µm. It is seen that $T_{\max}$ decreases with the increase of the BTJ diameter except $D_{\mathrm{BTJ}} \leq 4\,\mu\mathrm{m}$. In other words, the smaller devices are suitable for the higher temperature operation in CW mode. In order to identify the reason of this behavior, we measured the thermal resistance of each device as displayed in Fig. 6.16 b). The decrease of the thermal resistance with device diameter does not even follow $1/D_{\mathrm{BTJ}}$ behavior as expected for top emitting VCSELs. Therefore, the heat removal in such BTJ VCSELs is not one-dimensional, three-dimensional instead. The thermal resistance can be measured or extracted from the shift of emission wavelength to longer wavelength with increasing temperature and with increasing current which can be mathematically written as follows:

$$R_{\mathrm{th}} = \frac{\dfrac{\Delta\lambda}{\Delta P_{\mathrm{el}}}\,|_{T=\mathrm{const.}}}{\dfrac{\Delta\lambda}{\Delta T}\,|_{P_{\mathrm{el}}=\mathrm{const.}}} \tag{6.6}$$

Here, $\dfrac{\Delta\lambda}{\Delta P_{\mathrm{el}}}\,|_{T=\mathrm{const.}}$ is the electrical power tuning coefficient at a constant heatsink temperature and $\dfrac{\Delta\lambda}{\Delta T}\,|_{P_{\mathrm{el}}=\mathrm{const.}}$ is the thermal tuning coefficient at a constant applied electrical power.

At this point, Tab. 6.1 can be introduced in order to demonstrate a comparison of thermal resistance among VCSELs with active region diameter between 5 µm and 13 µm based on different material system. Thus one can have a better feeling about the thermal performance in devices under study. In particular, the thermal resistance value of the InP-based BTJ VCSEL mentioned in Tab. 6.1 is for the structure mounted epi-side-down onto an integrated Au-heatsink. Therefore, the presented top-emitting GaSb-based devices without any integrated heatsink shows a reasonably good thermal properties, indicating a good thermal design. As a part of the investigation to identify the reason of having a lower $T_{\max}$

	GaAs-based	**InP-based**	**GaSb-based**
Thermal resistance (K/W)	$1350 \leq R_{\mathrm{th}} \leq 3650$ [112]	$3500 \leq R_{\mathrm{th}} \leq 700$ [53]	$1980 \leq R_{\mathrm{th}} \leq 870$

Tab. 6.1: *Thermal conductivity for VCSELs with active diameter, $5\,\mu m \leq D_{\mathrm{a}} \leq 13\,\mu m$ ($D_{\mathrm{a}} \equiv D_{\mathrm{BTJ}}$) on different material system.*

at device with a larger diameter, the electrical CW threshold power P_{th} consumed by the device at a constant internal temperature is measured for VCSELs of different size. It is found that P_{th} is increasing at a higher rate than the decreasing rate of thermal resistance with increasing device size as demonstrated in Fig. 6.16 c). This is why the maximum CW lasing temperature decreases with the increase of the aperture diameter. For the device with very small aperture diameter, the threshold current increases again due to the high diffraction losses which leads to an increasing CW threshold power, resulting a lower CW operating temperature. The lower decreasing rate of thermal resistance and the higher increasing rate of consumed threshold power with increasing device aperture diameter give a dependence of temperature rise in the active region on the device size. As illustrated

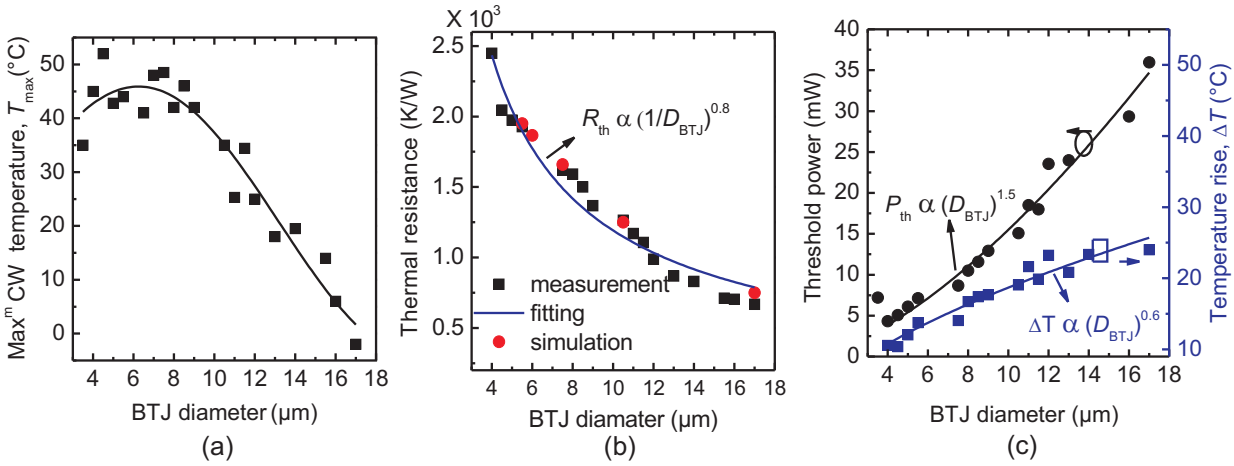

Fig. 6.16: *The dependence of a) maximum CW lasing temperature ($T_{\max}$) and b) thermal resistance at 20° C as a function of BTJ diameter of 2.6 µm VCSELs. The measured thermal resistance points are obtained by the method employing the lasing wavelength shift with temperature and applied electrical power, whereas, the calculated (red-marked) points are by the finite element method (FEM) simulation, showing a good agreement. The curve fitting was done with the measured data. c) The consumed threshold power at a constant internal temperature and the temperature rise of the active region with respect to the heatsink temperature against BTJ diameter of 2.6 µm VCSELs. The continuously increasing temperature rise of the devices with BTJ diameters indicates that the device performance can be further improved by a better thermal design.*

in Fig. 6.16 c), the temperature rise is scaled by the relation $\Delta T \propto D_{\mathrm{BTJ}}^{0.6}$. However, the temperature rise in the devices would be independent of device size if R_{th} and P_{th} would obey the scaling law $\propto {D_{\mathrm{a}}}^{-1}$ and $\propto D_{\mathrm{a}}$, respectively, where D_{a} is the active diameter, as expected for top emitting GaAs-based VCSELs [104].

For the case the aperture diameter defined by BTJ is larger than theoretical diameter of TEM_{00} mode, (corresponds to the LP_{01} fiber mode) i.e. $D_{\mathrm{BTJ}} > d_{\mathrm{TEM,00}}$, maximum CW operating temperature $T_{\max}$ is higher for lower size devices. This is true for devices under study which has been confirmed by the far-field measurement. In fact, devices up to 5 µm aperture diameter have a tendency to increase their CW operating temperature when moving from larger devices as shown in Fig. 6.16 a). TEM_{00} mode diameter $d_{\mathrm{TEM,00}}$ can be given by [113]

$$d_{\mathrm{TEM,00}} = \frac{4\,\lambda}{\pi\,\Theta_{1/e^2}} \tag{6.7}$$

where Θ is the angle in radians subtended by the $1/e^2$ diameter points in the far field. For example, for VCSELs with $D_{\mathrm{BTJ}} = 6\,\mu\mathrm{m}$ at 2.6 µm and $\Theta_{1/e^2} = 0.66$ rad (obtained from far-field measurement), $d_{\mathrm{TEM,00}}$ calculates to 5 µm. Therefore, the maximum CW operating temperature in these devices is governed by the thermal issues.

6.1.2.9 Diffraction Loss

As already mentioned, diffraction loss has been proven to be one of the dominant loss mechanisms in GaSb-based VCSELs [70]. As a part of loss-budget calculation, the diffraction loss was calculated as a function of the BTJ diameter (see Fig. 6.17). As expected, the diffraction loss increases when the BTJ diameter is decreased, and for $D_{\mathrm{BTJ}} \leq 8\ \mu$m the diffraction loss is of the same order of magnitude as the outcoupling loss through the mirrors; this can lead to an increased threshold current for VCSELs with a small BTJ.

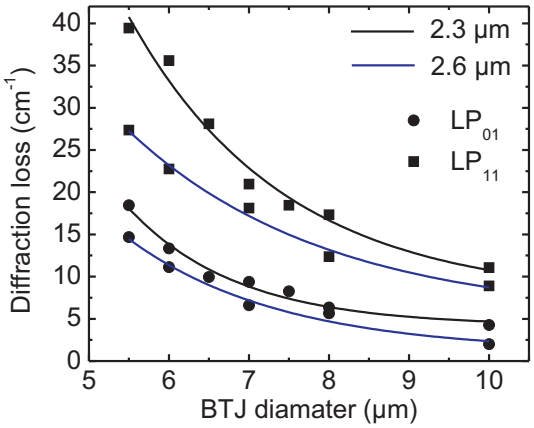

VCSEL @ 2.6 μm loss budget (D_{BTJ} = 8 μm)

	cm^{-1}	Type
Top mirror outcoupling loss	1.8	Calculated
Bottom mirror outcoupling loss	2.9	Calculated
Diffraction loss	5.5	Calculated
	10.2	
Total cavity loss	23.2	Measured
Rest	13	

(+) (-)

(b)

Fig. 6.17: *a) Simulated diffraction loss as a function of the BTJ diameter. Two different cavities are analyzed, the 2.3 µm VCSEL and the 2.6 µm VCSEL, the latter with a smaller BTJ-induced step in the cavity structure, thereby reducing the diffraction loss. For each cavity the diffraction loss for the fundamental mode field (LP_{01}) and for the first higher order mode field (LP_{11}) is calculated. b) Calculation of loss budget for 2.6 µm VCSELs with $D_{\mathrm{BTJ}} = 8\,\mu$m. (Diffraction loss calculation done in collaboration with Prof. Anders Larsson, Chalmers Univ. Tech., Sweden.)*

Fig. 6.17 a) also shows that the diffraction loss was somewhat lower for the 2.6 µm VCSEL. To understand how the diffraction loss is influenced by a change in the wavelength, we can view the BTJ as an aperture for the intracavity field. For a simple aperture one would say that the diffraction loss scales roughly as the square of the wavelength, simply because for a longer wavelength the aperture becomes smaller, measured in wavelength, and thus more of the light is diffracted off axis. On the other hand, if the aperture is a phase modulating one, with different amount of phase modulation inside and outside the aperture diameter, one would expect a decrease in the diffraction loss as the difference in phase modulation is decreased between the light passing through within the aperture and the light passing through outside the aperture. Of course, the BTJ and the structure above it is a more complicated structure than a simple aperture, but the trends in the behavior with respect to the diffraction loss should be the same. Thus we would expect that going from 2.3 µm to 2.6 µm, a 13% increase in wavelength, would result in an increased diffraction loss of ∼30% because the aperture becomes smaller measured in wavelengths. This was also confirmed in simulations keeping the phase modulation the same for both

wavelengths. On the other hand, the longer wavelength means that also the BTJ-induced step height is smaller measured in wavelength. This implies that the imposed phase modulation is smaller which lowers the diffraction loss. These two effects would thus partly balance each other; simulations showed that the net result would still be an increase of the diffraction loss as the emission wavelength is increased to 2.6 µm. Hence, the diffraction loss is reduced by decreasing also the physical BTJ-induced step height, to further reduce the phase modulation of the aperture. Thus, the 2.6 µm VCSEL cavity was modified by reducing the BTJ-induced step height from 72 nm in the 2.3 µm VCSEL to 55 nm. This strategy was successful, giving a small net reduction of the diffraction loss compared to the shorter-wavelength device. Finally, Fig. 6.17 a) shows that diffraction loss can be an important mode selecting mechanism. It strongly favors single mode operation in the fundamental LP_{01} mode thanks to the large loss difference to the first higher order mode.

Also the other loss mechanisms in VCSELs, such as outcoupling loss for both top and bottom mirrors obtained by the calculation is listed in Fig. 6.17 b). The total cavity loss has been measured to be as high as 23.2 cm^{-1}. The experimental procedure involved in obtaining the total loss value will be described in Subsect. 6.1.2.11. So, the remaining loss of 13 cm^{-1} can be attributed to the free-carrier absorption (FCA) losses in the epitaxial mirror, QW active region and the 3λ thick GaSb cavity. Out of those remaining losses, the average FCA loss in the epitaxial mirror can be calculated by

$$\bar{\alpha}_{\mathrm{m}}^{\mathrm{FCA}} = \frac{n_{\mathrm{l}}\alpha_{\mathrm{h}} + n_{\mathrm{h}}\alpha_{\mathrm{l}}}{n_{\mathrm{h}} + n_{\mathrm{l}}} \tag{6.8}$$

where $\bar{\alpha}_{\mathrm{m}}^{\mathrm{FCA}}$ is the average absorption coefficient in the epitaxial mirror, n_{l} and n_{h} the low and high refractive indices of the mirror material and the absorption coefficient in the high and low index material are denoted with α_{h} and α_{l}. For the emission wavelength of 2.6 µm, we have, $n_{\mathrm{AlAsSb}} = 3.19$, $n_{\mathrm{GaSb}} = 3.83$, $\alpha_{\mathrm{AlAsSb}} = 13.2$ cm^{-1} and $\alpha_{\mathrm{GaSb}} = 10.1$ cm^{-1} which yields $\bar{\alpha}_{\mathrm{m}}^{\mathrm{FCA}} = 11.7$ cm^{-1}, whereas the optical absorption losses in such DBRs were measured to be 5-10 cm^{-1} at 2.3 µm [114].

6.1.2.10 Internal Temperature

Neither the direct measurement nor the analytical analysis or modeling can accurately tell the internal temperature T_{in} of VCSELs. This is just because of the device self-heating as well as the presence of several unknown effects, e.g. QW Auger recombination in the device above threshold. Such heat-generating unknown effects introduces the non-linearity in the device *L-I* characteristics measured at constant T_{hs}. By removing only the self-heating effect from other effects, it is possible to obtain the *L-I* characteristics with a reduced non-linearity. For devices under study, we follow the wavelength method from [115] to obtain the *L-I* characteristics at constant internal temperature. Fig. 6.18 a) illustrates the contour curves of the device lasing wavelengths at different driving currents and heatsink temperature. Each constant emission wavelength curve indicates a constant internal temperature of the device which can be extracted by extrapolating those curves to $I = 0$. From Fig. 6.18 a), the internal temperature at which the laser turns off can be determined to be approximately 77°C which is the highest temperature the laser would work in pulsed mode. In order to verify this, the laser internal rollover temperature and turn off temperature defined by Eqn. 6.9 and Eqn. 6.10, respectively are plotted against the heatsink temperature

as shown in Fig. 6.18 b).

$$T_{\mathrm{ro}} = T_{\mathrm{hs}} + P_{\mathrm{ro}} R_{\mathrm{th}} \tag{6.9}$$

$$T_{\mathrm{off}} = T_{\mathrm{hs}} + P_{\mathrm{off}} R_{\mathrm{th}} \tag{6.10}$$

where P_{ro} and P_{off} are the applied electrical power at VCSEL thermal rollover and turn off, respectively.

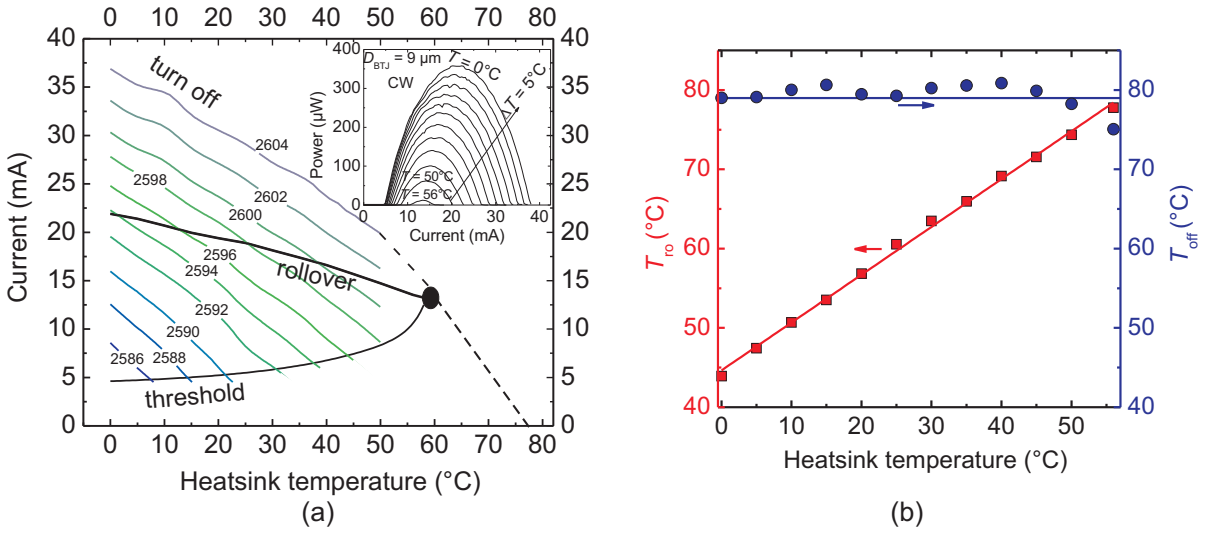

Fig. 6.18: *a) Curves of constant laser emission wavelength at different driving current and heatsink temperature. Each constant wavelength curve represents the constant internal temperature of the device which can be extracted by extrapolating them to $I = 0$. The laser turn-off temperature can be determined to $\approx 77^{o}$ C which is independent of T_{hs}. Temperature dependent L-I characteristics of the device with $D_{\mathrm{BTJ}} = 9\,\mu m$ is shown in inset. The maximum CW operating heatsink temperature of the device is approximately 59^{o}C. b) Internal rollover temperature (T_{ro}) and laser turn off temperatures (T_{off}) as a function a T_{hs}.*

The turn off temperature T_{off} has been found to be 77°C, showing a good agreement with the value determined by the method mentioned earlier. As expected, the laser turn off temperature T_{off} is independent of heatsink temperature while the thermal rollover temperature T_{ro} increases linearly with heatsink temperature. This is not surprising since the thermal rollover point is determined by not only the heatsink temperature and the amount of self-heating caused by the applied electrical power but also with the applied driving current. Evidently, the device operated at lower heatsink temperature will be driven by more current to reach the thermal rollover than it would be for higher heatsink temperature. Then the slope (equivalent to the differential quantum efficiency) of the *L-I* characteristics measured indirectly at constant internal temperature is plotted as a function of device internal temperature. As shown in Fig. 6.19, the slope decreases with increasing T_{in}. This is not surprising either since several unknown effects, for instance, QW leakage current, QW Auger recombination and leakage current through the region outside of BTJ can take place in the QW region with increasing temperature which has not been taken into account so far. The latter can be excluded from this discussion since the current confinement efficiency does not degrade in our devices with increasing temperature as demonstrated in Fig. 6.4. Here we measured the *I-V* characteristics of a point contact

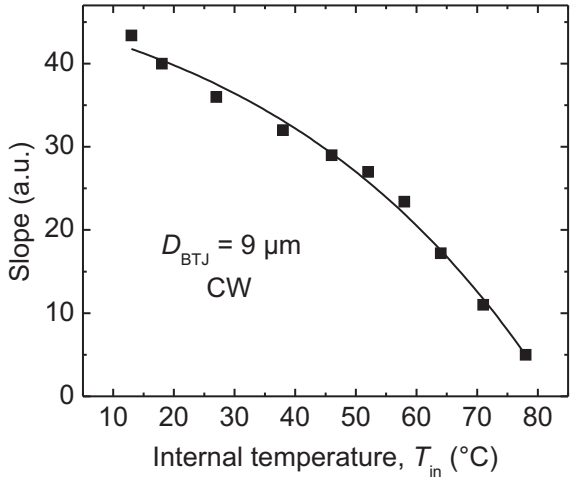

Fig. 6.19: *The slope of the L-I characteristics calculated at constant internal temperature as a function of internal temperature* T_{in}

test structure with diameter, $D_{\mathrm{pc}} = 23\,\mu\mathrm{m}$ in the region with BTJ and without BTJ. It was found that the ratio of the current in the region of BTJ to the region outside BTJ at a particular voltage of 0.8 is approximately 25,000 and this value remains almost constant with increasing temperature.

6.1.2.11 Laser Internal Parameters

Internal Quantum Effciency and Losses

The laser parameters like internal quantum efficiency and internal losses have a significant effect on the device performance. Having an accurate knowledge on these parameters are extremely important for a realistic modeling of VCSELs. These two internal laser parameters are experimentally determined by the method mentioned in [116]. In our VCSELs, the mirror reflectivity of the dielectric outcoupling DBR is decreased by depositing additional *a*-Si layer on top. This results in an increased threshold current and differential quantum efficiency with higher mirror losses, as expected. The differential quantum efficiency η_{d}, the internal loss α_{i} and the internal quantum efficiency η_{i} are related to each other by Eqn. 2.34.

With only 4 pair SiO_2/*a*-Si dielectric DBR and by depositing additional 80 nm, 104 nm, 128 nm and 141 nm *a*-Si on top of that mirror which corresponds to a power reflectivity of 99.8%, 99.7%, 99.6%, 99.5% and 99.2%, respectively, the differential quantum efficiencies are measured from *L-I* characteristics of single-mode VCSELs emitting at 2.6 µm at a heatsink temperature of 10°C and 0°C. Plotting $1/\eta_{\mathrm{d}}$ against the calculated $1/\alpha_{\mathrm{m}}$ and using a linear fit according to Eqn. 2.34, $\eta_{\mathrm{i}} = 40\%$ and $\alpha_{\mathrm{i}} = 23.2$–$26\ \mathrm{cm}^{-1}$ are obtained as illustrated in Fig. 6.20.

The reduced internal quantum efficiency in such laser could be attributed to several issues, such as hole confinement of the QWs, hole leakage by thermionic emission or inhomogeneous filling of the QWs by the carriers. The latter is rather unlikely since the conduction and valence band offsets are as low as $\Delta E_{\mathrm{c}}^{\mathrm{QW}} \approx 212\,\mathrm{meV}$ and $\Delta E_{\mathrm{hh}}^{\mathrm{QW}} \approx 48\,\mathrm{meV}$, respec-

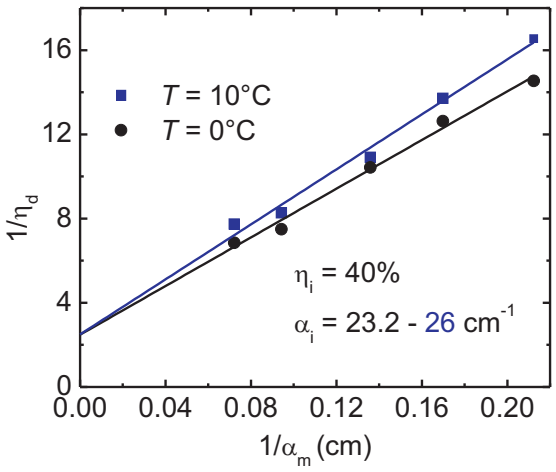

Fig. 6.20: *Inverse differential quantum efficiency (η_{d}^{-1}) against the inverse of mirror loss α_{m}^{-1} in order to extract the internal parameters η_{i} and α_{i} using a linear fit.*

tively as shown in Fig. 3.1. Electrons remain very well confined in such QWs due to its moderately large conduction band offset, whereas $E_{\mathrm{hh}}^{\mathrm{QW}}$ value is just less than twice of the thermal energy at room temperature ($k_{\mathrm{B}}T$). Therefore, hole leakage by thermionic emission could be the most probable reason of the low η_{i}. Even the separate confinement layer $\mathrm{Al}_{0.15}\mathrm{Ga}_{0.85}\mathrm{As}_{0.01}\mathrm{Sb}_{0.99}$ does not help so much in confining the carriers into the active region since the valence band offset at the separate confinement layer $E_{\mathrm{hh}}^{\mathrm{SCH}}$ is approximately twice as low as $k_{\mathrm{B}}T$. The low η_{i} could also be due to the presence of well-known strong non-radiative Auger recombination effect at the long wavelength MIR lasers.

The extracted loss parameter α_{i} contains all types of losses in the laser resonator. It includes outcoupling mirror losses, free carrier absorption in the cavity, active region and epitaxial bottom Bragg mirror and diffraction loss. It should be noted that the deviation in α_{i} value as indicated in Fig. 6.20 is resulting from the measurement carried out at two different temperatures and partly due to the different current injection magnitude. This clearly indicates the presence of temperature dependent loss mechanisms, e.g. Auger recombination, in the resonator. As expected, at 10°C the value of α_{i} is higher than at 0°C since α_{i} and η_{i} are both function of temperature.

Gain Constant and Transparency Current

Gain constant (g_{o}) for the active region material and transparency current density, J_{tr} are other two important laser parameters which can be determined experimentally. The gain and current density can be related by Eqn. 2.35. In this work, both J_{th} and g_{th} of the device was changed by changing the outcoupling mirror reflectivity, while g_{th} is related to the reflectivity of outcoupling mirror by

$$g_{\mathrm{th}} = \frac{1}{\Gamma_z}\left(\alpha_{\mathrm{i}} + \frac{1}{2L_{\mathrm{eff}}}\ln\left(\frac{1}{R_{\mathrm{oc}}R_{\mathrm{b}}}\right)\right) \tag{6.11}$$

where Γ_z is the longitudinal confinement factor which is calculated to be 0.037. Thus the calculated threshold gain are plotted as a function of measured threshold current density

at a heatsink temperature of 0°C and 10°C as shown in Fig. 6.21 a). Logarithmic fitting using Eqn. 2.35 yield values for g_0 and J_{tr}.

In fact, I_{tr} sensitively depends on the sample quality and fabrication process and g_0 value obtained here is in a range and the measurement also involves some experimental inaccuracies. So, we recalculated these two laser parameters by an alternative experimental method.

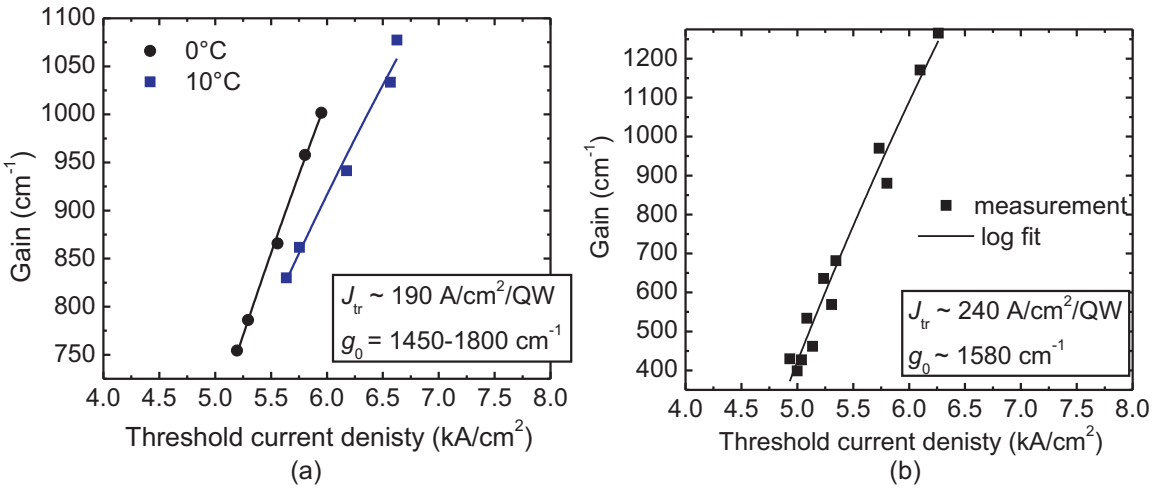

Fig. 6.21: *a) Measured quantum well threshold gain against threshold current density for 2.6 µm VCSELs at 0°C and 10°C. The measured points are fitted using Eqn. 2.35. b) Gain-current density curve for 2.6 µm VCSELs based on threshold gain variation with aperture diameter of the device.*

This time η_{d} and J_{th} are measured for a number of devices with $5\,\mu\mathrm{m} \leq D_{\mathrm{BTJ}} \leq 16\,\mu\mathrm{m}$ at a constant internal temperature. And QW gain is related to η_{d} via Eqn. 2.14, 2.33 and 6.11

$$2\Gamma_{\mathrm{r}} g_{\mathrm{th}} N_{\mathrm{QW}} L_{\mathrm{QW}} = \frac{\eta_{\mathrm{i}} T_{\mathrm{b,oc}}}{\eta_{\mathrm{d}}} \tag{6.12}$$

where $T_{\mathrm{b,oc}}$ is the transmission through both top and bottom mirror. The left and right side of Eqn. 6.12 refers to total round trip gain in the active region and the round trip loss δ in the device, respectively.

Thus we obtain a pair of numbers $(g_{\mathrm{th}}, J_{\mathrm{th}})$ where g_{th} is calculated using Eqn. 6.12. As expected, both the threshold current and threshold current density will vary with the change of devices with different aperture diameters. As shown in Fig. 6.21 b), $g_{\mathrm{o}} = 1580\ \mathrm{cm}^{-1}$ and $J_{\mathrm{tr}} = 240\,\mathrm{A/cm}^2$ per QW can be extracted by plotting these measured data and then fitting with logarithmic gain-current relation. Compared to GaAs-based material system, the higher gain coefficient value indicates that this material system exhibits excellent gain properties of the active region material [117].

Optimum Number of QWs

With the known g-J relationship we are in position to determine the optimum number of QWs for devices under study. Note that the round trip loss δ is given by

$$\delta = 2N_{\mathrm{QW}}L_{\mathrm{QW}}\Gamma_{\mathrm{r}}(N_{\mathrm{QW}})g_{\mathrm{th}}(J_{\mathrm{th}},N_{\mathrm{QW}}) \tag{6.13}$$

$$J_{\mathrm{th}} = \frac{N_{\mathrm{QW}}J_{\mathrm{tr}}}{\eta_{\mathrm{i}}}\exp\left(\frac{\delta}{2N_{\mathrm{QW}}L_{\mathrm{QW}}\Gamma_{\mathrm{r}}g_0}\right) \tag{6.14}$$

For two different round trip cavity losses, the calculated CW threshold current density is plotted as a function of number of QWs by Eqn. 6.14 as indicated in Fig. 6.22. An exemplary numerical calculation of the threshold current density J_{th} for the device with $D_{\mathrm{BTJ}} = 5\,\mu\mathrm{m}$ is mentioned here which has been marked by a red dot in Fig. 6.22. Using Eqn. 6.13 and $N_{\mathrm{QW}} = 7$, $L_{\mathrm{QW}} = 10$ nm, $\Gamma_{\mathrm{r}} = 1.8$ and $g_{\mathrm{th}} = 638\,\mathrm{cm}^{-1}$, one obtains the round trip loss δ=1.6%, where the value of g_{th} can be calculated by Eqn. 2.35 using measured values, i.e. $J_{\mathrm{th}} = 5.2\,\mathrm{kA/cm^2}$, $\eta_{\mathrm{i}} = 0.4$, $J_{\mathrm{tr}} = 0.19\,\mathrm{kA/cm^2}$ and $g_{\mathrm{o}} = 1450\ \mathrm{cm}^{-1}$. The round trip loss value δ can also be calculated by the right side of Eqn. 6.12 and using measured $\eta_{\mathrm{d}} = 8.8\%$, $\eta_{\mathrm{i}} = 0.4$ and calculated $T_{\mathrm{b,oc}} = 0.0035$. Finally one calculates CW threshold current density $J_{\mathrm{th}} \approx 5.2\ \mathrm{kA/cm^2}$ using Eqn. 6.14 and in good agreement with the measured value.

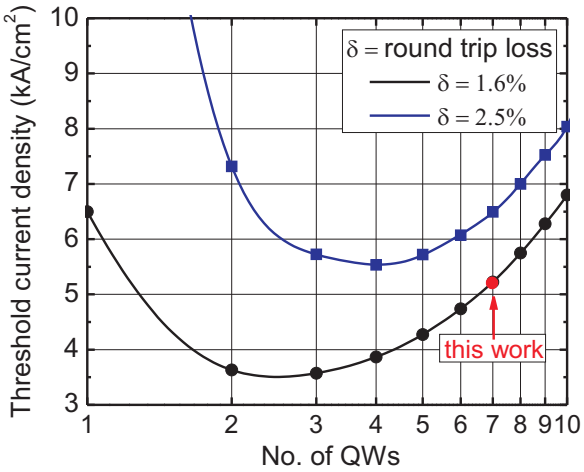

Fig. 6.22: *Calculated CW threshold current density as a function of number of QWs in 2.6 µm VCSELs.*

As can be seen in Fig. 6.22, with 1.6% round trip loss, the optimum number of well is 3, whereas 7 QW was used in presented devices. Therefore, reducing the number of QWs from 7 to 3, J_{th} will decrease and thus the device performance will be improved.

6.1.2.12 Gain-Cavity Offset

The adjustment of the gain-offset is a critical design issue for long wavelength VCSELs to minimize the temperature sensitivity of the threshold current. The gain-cavity offset $\Delta\lambda_{\mathrm{gc}}$ can be expressed as λ_{gain}-λ_{cav}, where λ_{gain} is the gain peak wavelength and λ_{cav} is the cavity

resonance. This offset depends on the temperature T since λ_{gain} shifts with the change of QW bandgap $E_{\text{g}}(T)$, while λ_{cav} shifts with changing refractive index of the cavity layers. Unlike GaAs-based VCSELs, InP-based VCSELs show the minimum threshold current far below the temperature of zero-gain offset $\Delta\lambda_{\text{gc}} = 0$ [118, 119]. As a design rule, this zero-gain offset is expected to be around room temperature to obtain minimum temperature sensitivity.

To investigate the value of gain-cavity offset value at RT as well as the value of T where zero gain offset is located in devices under study, the temperature dependence of the cavity resonance $\lambda_{\text{cav}}(T)$ was experimentally determined by observing the cavity mode position at different temperature under pulse operation. The emission wavelength shift with temperature was measured to be $\mathrm{d}\lambda_{\text{cav}}/\mathrm{d}T = 0.25\,\text{nm/K}$ corresponds to the change of lasing energy $\mathrm{d}E_{\text{cav}}/\mathrm{d}T = 0.046\,\text{meV/K}$. On the other hand, to obtain the information on the shifting rate of gain peak wavelength, broad-area (BA) edge-emitting lasers (EELs) containing the same active region of VCSEL structure were processed. The thermal dependence of the gain peak wavelength $\lambda_{\text{gain}}(T)$ was measured from the temperature-induced shift of the peak emission wavelength of EELs. The gain peak wavelength shift with temperature was measured to be $\mathrm{d}\lambda_{\text{gain}}/\mathrm{d}T = 1.5\,\text{nm/K}$, giving a thermal bandgap shrinkage $\mathrm{d}E_{\text{g}}/\mathrm{d}T = 0.28\,\text{meV/K}$. Thus, the gain maximum $\lambda_{\text{gain}}(T)$ red-shifts six times faster than the cavity mode $\lambda_{\text{cav}}(T)$, emphasizing the strong dependence of the gain-cavity offset $\Delta\lambda_{\text{gc}}$ on device temperature. The extrapolated point corresponds to the gain-cavity alignment is found to be at $0.481\,\text{eV} \equiv 2580\,\text{nm}$ and at RT, the gain-cavity offset is 8 meV as displayed in Fig. 6.23 a). To verify this measurement, the emission wavelength and the gain peak wavelength shift with the hydrostatic pressure were also measured. From hydrostatic pressure tuning, the gain-cavity alignment has been extracted also at 0.481 eV as displayed in Fig. 6.23 b).

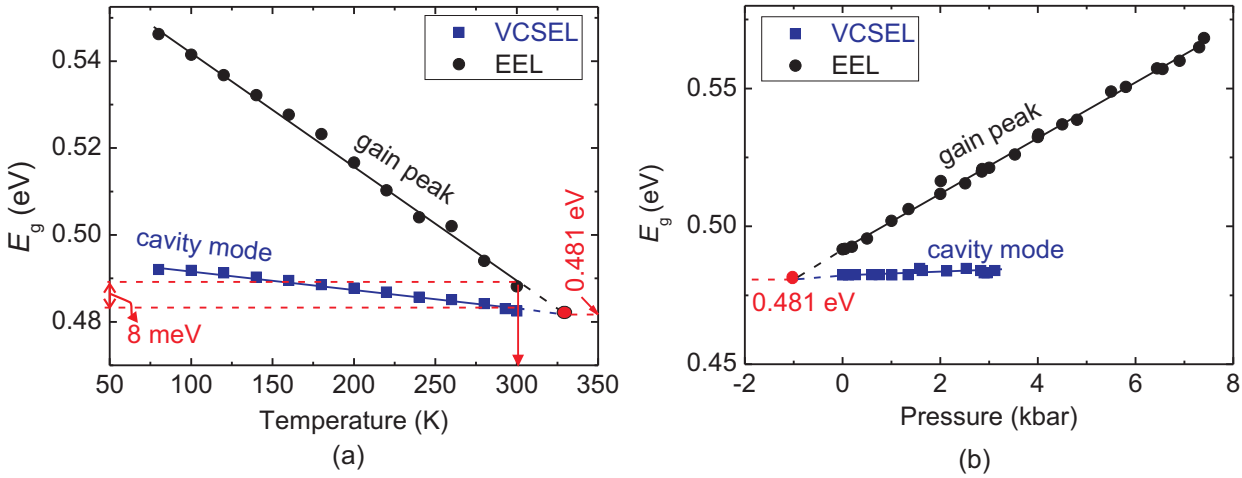

Fig. 6.23: *Change of lasing photon energy corresponds to gain peak and cavity mode in CW-operated edge-emitting laser and VCSEL, respectively as a function of a) temperature and b) pressure.*
Measurement done at the Advanced Technology Institute, University of Surrey, UK.

Now let's examine the threshold current-temperature characteristics of a ∼2.6 µm VCSEL. Such characteristics in these devices are governed by temperature dependent three effects. Firstly, the optical gain is a function of temperature, in other words, the optical gain decreases with increasing temperature [120]. The second effect is the temperature dependent relative spectral misalignment between gain maximum and cavity resonance. Apart from these two effects, also non-radiative Auger recombination plays an important role in these devices above 240 K. Fig. 6.24 shows the temperature dependent threshold current behavior in the temperature range of 80 K-330 K. As can be seen, minimum I_{th} has been found around 200 K, whereas the zero-gain offset is at 330 K. This is not surprising since similar behavior has already been observed in InP-based VCSELs [118]. In very long-wavelength GaSb-based VCSELs, the threshold minimum and zero gain offset are even far away from each other. But most VCSEL applications require low temperature sensitivity at or above RT, i.e. I_{th} minimum for presented devices should be moved to higher temperature. In order to achieve this at constant emission wavelength, the gain spectrum needs to be blueshifted or the cavity mode has to be redshifted using the same active region.

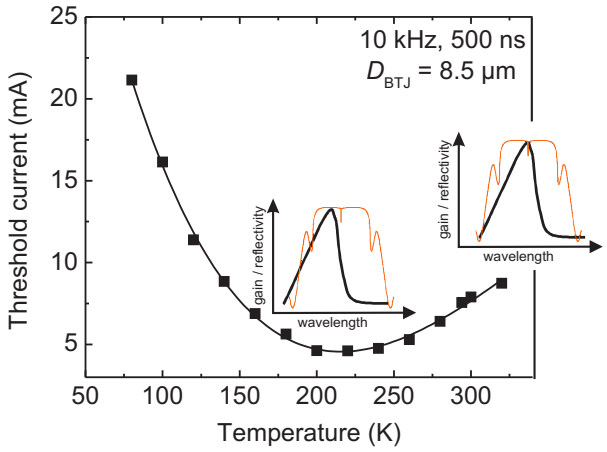

Fig. 6.24: *Pulse threshold current-temperature characteristics of GaSb-VCSELs with $D_{BTJ} = 8.5\,\mu m$. The relative spectral position of cavity mode and gain peak at different temperature is shown as inset.*
Measurement done at the Advanced Technology Institute, University of Surrey, UK

6.1.3 Noise Characteristics

The RIN measurements were performed by placing the VCSEL in front of a Peltier-cooled InAs photodector (PD) from Judson Technologies as close as possible. In practice, the distance from the VCSEL to the PD window was 2 mm. The PD signal was amplified in the transimpedance amplifier with a maximum gain of 10^5 V/A. The photodiode was kept at about -34.5°C temperature, while the TO-housed VCSEL was at 15°C. On the optical plane, the angle of the VCSEL in regard to the PD was aligned for maximum signal level which was monitored by an oscilloscope. From the amplifier the signal was directed to an RF-analyzer that was used to measure noise power density at a signal with frequency of 12 kHz. The calculation of RIN value is shown in Tab. 6.2 using the formula mentioned in

Chap. 2.

P_0	R	G	$P_{\text{noise,dBm}}$	P_{noise}	
Optical power incident on photodiode	Detector responsitivity	Amplifier gain	Measured noise power density	Measured noise power density	RIN
(W)	(A/W)	(V/A)	(dBm/Hz)	(W/Hz)	(dB/Hz)
6×10^{-5}	1.2	10^5	-75.8	2.6×10^{-11}	-106

Tab. 6.2: *Calculation of RIN value for 2.6 µm GaSb-based BTJ VCSELs. Measurement done at the Optoelectronics Research Center, Tampere Univ. Tech., Finland*

A significant uncertainty relates to the optical power that is coupled to the detector surface (P_0). With the pyrocamera it was not possible to see the beam profile and it is difficult to comment on the beam divergence. It was assumed that 50% of the maximum power is coupled to the detector (60 µW). By changing this value it is possible to see the effect on RIN. The measurements indicate a RIN value in the order of -100 dB/Hz, assuming that other noise sources are small here.

6.1.4 Water Vapor Measurement by WMS

An emission wavelength of 2.6 µm is of significant interest for gas detection by TDLAS. In fact, emission wavelengths of the presented lasers are obtained at 2.605, 2.596 and 2.594 µm where the strongest water vapor absorption lines are located. Such application-suited VCSELs open the way for gas measurements and isotopic ratio studies [121] by realizing absorption spectrometers with significant sensitivity improvements.

To prove the applicability of the VCSEL, an experiment was carried out in which the emission wavelength or intensity of the laser was modulated across the atmospheric water absorption features. This will show the suitability of such lasers in terms of modulation speed and stability of single-mode emission. The modulation was done by changing the driving current with an additional sinusoidal signal of frequency 10 kHz. This WMS method typically has a higher sensitivity for detecting the trace gases than direct absorption spectroscopy.

In order to measure the atmospheric water vapor concentration, the first and the second harmonic (2f) spectra were recorded with the help of a lock-in amplifier which receives the intensity-modulated signal from the detector. Using the model in [36], the measured spectra are then fitted analytically as illustrated in Fig. 6.25 a). An absolute water vapor concentration of 1.5% in laboratory air was determined. The excellent fit proves that the laser exhibits single-mode operation and without mode-hops over the entire operating range (shown in Fig. 6.25 b)) which is required for high resolution TDLAS.

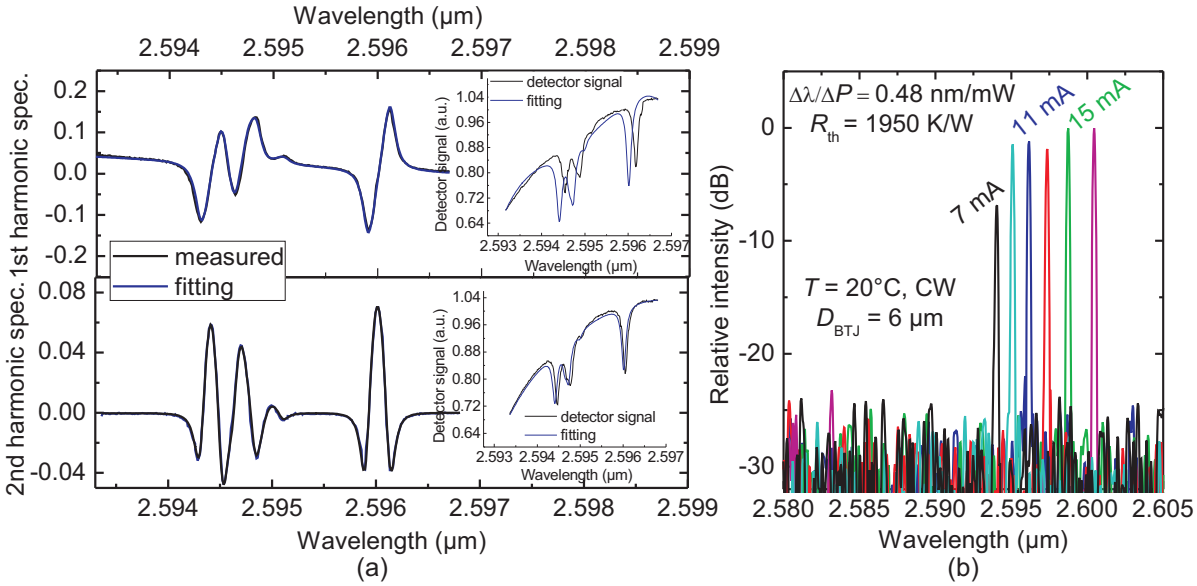

Fig. 6.25: *a) Measured WMS first and second harmonic spectra of H_2O absorption lines (black lines) and the fit using absorption line parameters from HITRAN database [10] (blue lines). The detected signal at the photodetector for VCSELs emitting at 2.6 µm and the fit extracted from corresponding first and second harmonic spectra as shown in inset. Due to the lack of the temperature stability in the measurement setup, a mismatch appears between these two signals. b) The driving current dependent emission spectra at T_{hs} = 20°C, showing the single-mode emission and the range of tunability.*
WMS signal fitting done by A. Hangauer, SIEMENS AG, Munich, Germany.

6.2 GaSb-Devices at 3.4 µm

As a part of the investigation, many attempts have been made to extend the emission wavelength of VCSELs as already mentioned. For brevity, the electrical characteristics of VCSELs with an emission wavelength of only 3.4 µm will be described here which at least can provide an understanding of the VCSEL failure reason.

6.2.1 Electrical Characteristics

The most important electrical characteristics of VCSELs at 3.4 µm will be tabulated in Tab. 6.3. For comparison, the characteristics of the working VCSELs at 2.6 µm is also presented here. As can be seen, VCSEL devices at 3.4 µm shows a higher series resistance leading to a high voltage drop and lower blocking ratio compared to working devices. The reason of this high resistance has been investigated and the outcome of such investigation will be discussed here.

The reason of this high resistance could be due to either the top *p*-side metal semiconductor contact or tunnel junction buried in the device as an intra-cavity ohmic contact. At first, top *p*-side contact resistivity has been measured by using the test structures present in our wafer utilizing TLM method and the resistivity is found as low as $6 \times 10^{-6}\ \Omega\,\mathrm{cm}^2$, indicating that the top *p*-side contact cannot be the reason. This has also been confirmed by

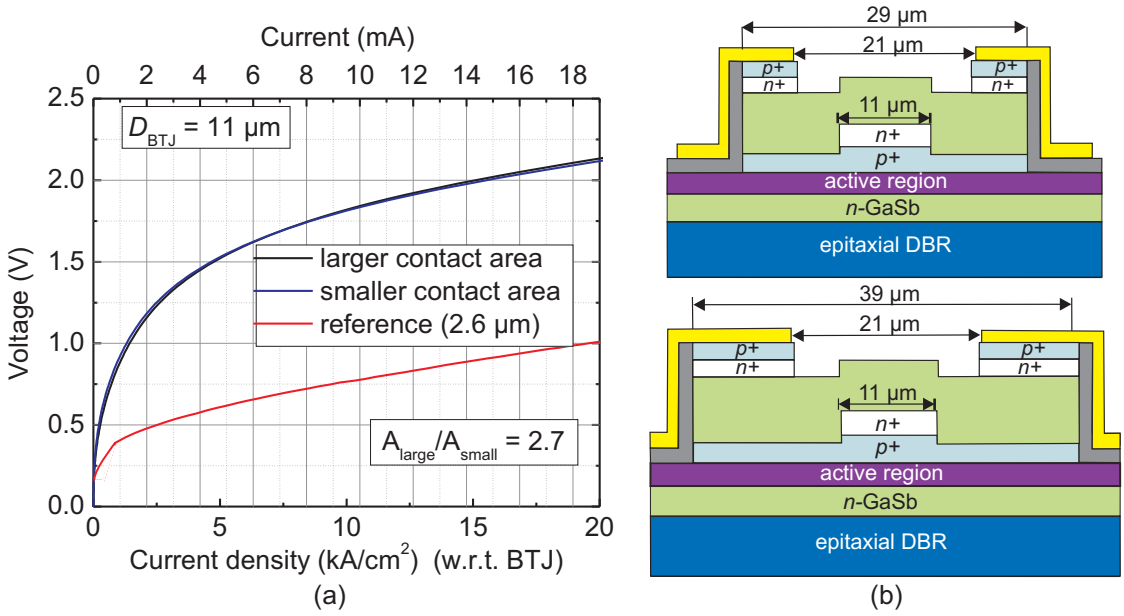

Fig. 6.26: *a) J-V characteristics of VCSEL devices with same BTJ diameter but with different contact layer area, b) schematic of devices with different contact layer area and their dimensions.*

Design wavelength	Contact resistance by TLM	Series resistance @ D_{BTJ}=11 µm	Blocking ratio @ 1 V	Voltage drop @ 20 kA/cm²
2.6 µm (working)	7-8 × 10^{-6} Ωcm²	17 Ω	> 10,000	1 V
3.4 µm	5-6 × 10^{-6} Ωcm²	128 Ω	> 80	2.13 V

Tab. 6.3: *Comparison of electrical characteristics between working and non-working VCSEL*

the measurement of *J-V* characteristics of VCSEL devices with same BTJ diameter (11 µm in this case) but with different contact layer area as shown in Fig. 6.26 a). Increasing the contact layer area does not improve *J-V* characteristics of the device with larger contact area. In order to measure the blocking ratio, several test structures present in the processed wafer were measured. The blocking ratio was determined from the current density ratio in the non-etched and etched region of the BTJ at a particular applied voltage by measuring *J-V* characteristics of these test structures. Note that these characteristics were obtained by averaging the multiple curves of several test structures in order to avoid the inconsistent behavior among test structures. The blocking ratio of this sample amounts to as low as ≈80 @ 1 V, whereas the old working VCSEL at 2.6 µm exhibits the blocking ratio over 10,000 @ 1 V. So, the resulting current confinement was very poor in the device.

Now current density-voltage characteristics of devices with different BTJ diameters along with 5 µm point contact. At a particular voltage, e.g. 1 V, the current density in the 5 µm point contact is 3 kA/cm² as shown in Fig. 6.27 a). This can be considered as the current limit in this comparison since the point contact does not have any blocking region compared to devices with different BTJ diameters. As expected, VCSEL devices with different

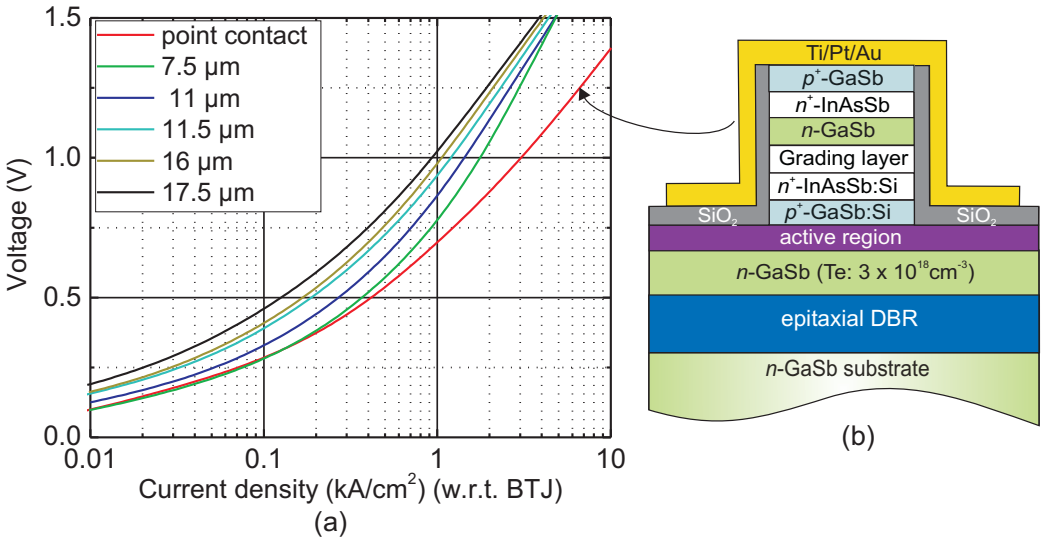

Fig. 6.27: *a)J-V characteristics of devices with different BTJ diameters, showing the current limit through the tunnel junction, b) schematic of a point contact with 5 µm diameter.*

BTJ diameters have the current density less than 3 kA/cm^2 at the same applied voltage, indicating the tunnel junction is highly resistive which does not allow the current to flow through it. This could be attributed to the tunnel junction itself or the inappropriate cleaning procedure before the overgrowth. This will be investigated in the future.

Based on the description written so far, it is clear that the tunnel junction seems to be the main problem for such high resistance. It is not still clear whether the tunnel junction itself or the inappropriate cleaning procedure carried out before the overgrowth. The high resistance of the tunnel junction seems to be a bit unlikely since the tunnel junction in our devices inherently favors carrier tunneling even with low doping.

Please note that a change has been made in such device structure by replacing the classical top p-side n-InAsSb contact with a ultra-low resistive p^+-GaSb/n^+-InAs tunnel junction as can be seen in Fig. 6.26 b). The growth details and point contact results of this ultra-low resistive tunnel junction can be found in [122]. The key advantage of using such tunnel junction-based contact is to have a topmost p^+-GaSb layer onto which a low-resistive p-side ohmic contact can be formed easily due to Fermi-level pinning near the GaSb valence band edge.

6.2.2 Optical Characteristics

After the electrical characteristics of the VCSEL structure, optical measurements were performed to characterize the device performance. Due to the high resistivity and very poor current confinement, RT CW lasing is less likely in measured devices. But still lasing under pulse operation could be expected from these devices since they can be driven by pulse-current with a low duty cycle (e.g. 0.2%) by which one can get rid of the heating effect generated by the high resistance of the device. In addition, poor current confinement confirmed by the low blocking ratio can be circumvented by applying a reasonable amount

of current. Because this time current need to be injected homogeneously over the whole mesa. Please note that the applied current should be approximately 5-6 times higher than the case when the device would have good current confinement defined by the BTJ aperture diameter. Unfortunately, no lasing effect could be achieved so far as can be understood in Fig. 6.28, showing the pulsed *L-I* characteristics of a device with an mesa diameter of 31 µm.

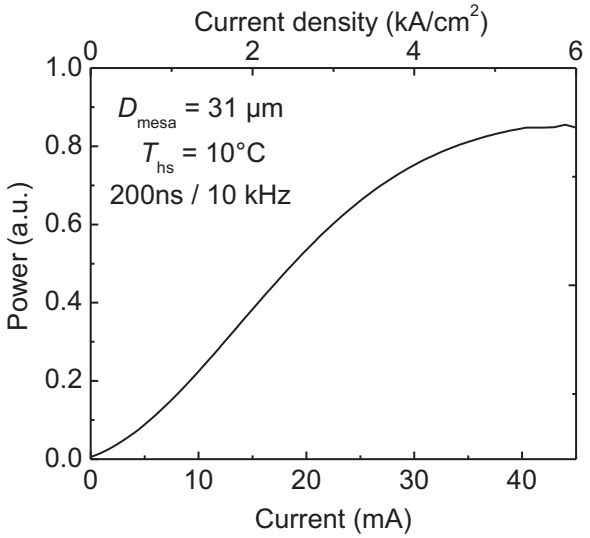

Fig. 6.28: *L-I characteristics of a device with 31 µm device diameter under pulse operation*

The device exhibits only spontaneous emission and it has already reached in the saturation region at a current density of 6 kA/cm^2. The reason of this non-lasing behavior is not yet understood. At first glance, one could think of the mismatch of the cavity resonance (i.e. misaligned cavity) which can be confirmed by the measurement of a electroluminescence spectra. But measuring the electroluminescence spectra at this very long wavelength regime is a bit challenging which could not be successfully performed during this thesis. This can be investigated in the future. Though the cavity misalignment seems to be a bit unlikely in this case since the cavity resonance was measured on the processed wafer just before the top dielectric mirror evaporation and the cavity was adjusted accordingly. Apart from the misaligned cavity, very strong Auger and FCA loss at this very long wavelength could prevent the lasing.

In summary, this chapter discusses several performance-related aspects of GaSb-based BTJ VCSELs based on theoretical and experimental results. These results allow a deeper insight into the internal device physics, such as radial diffusion of carriers, maximum continuous-wave operating temperature, diffraction loss, internal temperature, gain and loss parameters, internal quantum efficiency of the active region etc. These parameters can be taken into account while designing mid-infrared lasers which leads to an improved device performance. In addition, an application-based results utilizing these lasers for the measurement of absolute water vapor concentration by wavelength modulation spectroscopy (WMS) method are also described, hinting that devices are well-suited for the targeted applications.

7 Conclusion and Outlook

Conclusion

The work presented in this dissertation describes the development of electrically-pumped GaSb-based BTJ VCSELs for emission wavelengths of above 2 µm preferably operating continuously at and above room temperature. Devices should exhibit single-mode operation over their entire operating range with a high (electro)thermal wavelength tunability to be suitable for TDLAS-based photonic sensors.

In the previous chapters, various aspects of the design, fabrication and characterization of long wavelength GaSb-based VCSELs have been described in details. Much emphasis has been laid on the device characterization based on the theoretical and experimental investigations which allows to improve both the device design and performance. Despite of the fact that the GaSb-based material system (AlGaIn)(AsSb) is the material of choice for achieving highly reliable devices in the mid-infrared wavelength regime, the research on EP GaSb-based VCSELs is still at a preliminary stage. This work is directed toward addressing aspects of VCSEL design and performance that may be an input to the ongoing research and development efforts.

The outcome of this work is the establishment of the technology for high-performance single-mode and tunable GaSb-VCSELs and development of appropriate device design. As a part of the device design, the relevant material properties and parameters of materials utilized in VCSELs have been explored. During the thesis, several VCSEL structures have been developed in terms of the design and fabrication to generate light emission at 2.6 µm, 2.8 µm, 3.2 µm and 3.4 µm for sensing applications. Only VCSELs at 2.6 µm show lasing with all the desired properties. The rest of the structures did not get into working devices due to lack of high quality epitaxial growth, inappropriate overgrowth cleaning procedure followed by overgrowth resulting a bad surface morphology and severe electrical problems. Finally, the suitability of the working lasers has been proved through water vapor measurement.

As already mentioned, GaSb-BTJ VCSELs comprises several crucial components, e.g. top p-side contact and tunnel junction which influences the electrical performance of the device to a great extent. The device workability highly depends upon the successful integration upon these individual components. But with the advent of a better understanding on the growth of reproducible high quality epitaxial layers with superior surface morphology before and after the overgrowth, optimization of the atomic hydrogen cleaning parameters, a controllable and repeatable device processing and a sufficient knowledge on the material properties and parameters, the future structures could get into working devices.

It is believed that the results presented in this thesis point to a bright future for GaSb-VCSELs for use in sensing systems and the contributions of this work lead to continued

improvement in this research area. It is hoped that upon optimizing the structure design, the improvement of material quality and heat management, a room temperature CW operation is likely to be achieved in the near future.

Outlook

In the following the discussion for the improvements to present devices will be introduced.

- **GaSb-VCSEL on GaAs Substrate**
  The epitaxial growth of GaSb-based materials on alternative substrates such as GaAs is highly desirable and has drawn a lot of attention recently. The existing large lattice mismatch between these two semiconductors is the main obstacle of fulfilling such desires. The consequence of this mismatch generally leads to the formation of a high density of threading dislocations which is incompatible with the fabrication of high performance devices. However, this problem can be overcome by an optimum growth procedure and introducing an interfacial misfit (IMF) array at the interface between GaAs and GaSb layer [123]. Lasers operating at room temperature in pulsed regime emitting at 1.65 µm [124], at 1.82 µm [125] and in CW regime at 2.2 µm [126] have already been demonstrated using this novel technique. But these devices operate at a very high threshold current density and a high threshold voltage.

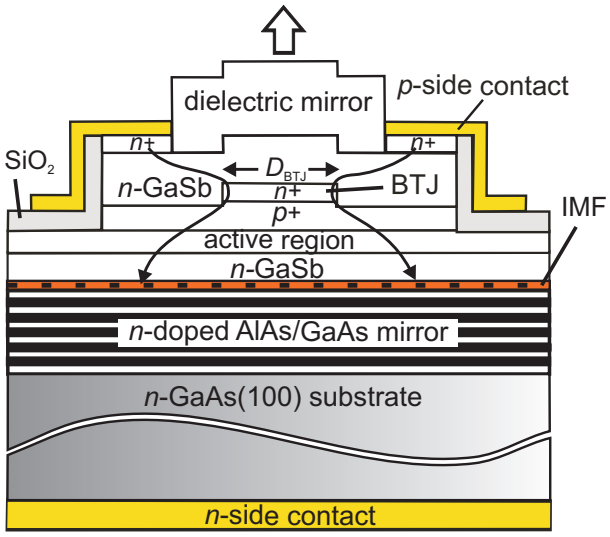

Fig. 7.1: *Schematic cross-sectional view of a proposed top-emitting GaSb-based VCSEL with current aperture grown on GaAs substrate, having twofold epitaxial growth*

An investigation can be made for the first time on the realization of electrically-pumped single-mode MIR VCSELs using an AlAs/GaAs Bragg mirror on GaAs substrates. A successful technological realization of such devices would certainly lead to a great breakthrough in the photonics society. As a matter of fact, compared to GaSb substrates, GaAs substrates are cheaper, more reproducible in terms of epitaxial growth onto it and it has a more mature production technology.

- **VCSEL with Upside-down**
  The first step towards increasing the thermal conductance of GaSb-based BTJ VCSELs is to mount the lasers upside-down on to integrated Au-heatsinks as discussed in Chap. 4. In such a way, the heat generated in the active region is removed via the current spreading layer towards Au-substrate which lead to a better performance compared to the presented devices. However, increased device performance in terms of the thermal conductance often involves sacrificing the device current tuning rate.

- **Reduction of Diffraction Loss**
  As mentioned in Chap. 3, the selective etching of tunnel junction layers forms a pillar-shaped profile in the device whose height plays an important role in reducing the diffraction loss. The lower the pillar height, the lower the diffraction loss. The pillar height can be reduced to a great extent by reducing the thickness of the topmost cap layer which is placed on top of the grading layer. But note that the importance of the 25 nm thick cap layer in the presented devices needs to verified at first. Based on this investigation, the necessary action can be taken. This height can also be reduced during the device processing. This can be done by selective etching of ≈ 40 nm material in the pillar. Thanks to the reduced BTJ step height which brings an additional benefit at the same time by obtaining a weaker index-guiding. This will lead to a large-size device with a high single-mode output power.

- **MEMS Tunable VCSEL**
  Another advanced area where future work could be focused on is the realization a novel two-chip concept for electrically-pumped and micro-electromechanical system (MEMS) tunable VCSELs with a tuning range of several tens of nanometer. The active part of the device is just like the one with upside-down configuration without top dielectric mirror as illustrated in Fig. 7.2. The top dielectric mirror can be replaced

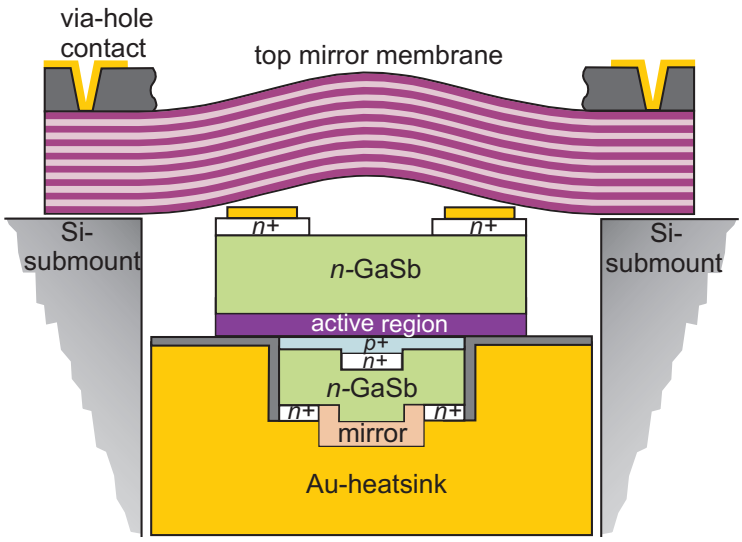

Fig. 7.2: *Schematic cross-sectional view of the MEMS tunable VCSEL, figure modified from [127].*

by the movable top mirror membrane which can be made of GaAs/AlGaAs layers

giving rise to a very high reflectivity, including the effect of the airgap that serves as an additional mirror layer. Via-hole contacts through the substrate can be used to inject a tuning current into the doped membrane layers. This results in a membrane deflection by ohmic heating. Details of the device concept can be found in [127]. Recently, a micro-electro mechanically tunable VCSEL consisting of an InP half-VCSEL and a surface micro-machined mirror membrane with a single-mode tuning range of 102 nm has been demonstrated [128].

List of Symbols

Symbols

B	normalized effective refractive index	21
D_{BTJ}	aperture diameter defined by BTJ	20
D_{ISR}	diameter of the surface relief	43
d_{QW}	total thickness of the active region	16
$d_{\mathrm{TEM,00}}$	TEM_{00} mode diameter	93
$\lvert E(z)\rvert$	amplitude of the longitudinal standing wave field	16
$\Delta E_{\mathrm{hh}}^{\mathrm{QW}}$	valence band offset in QW	27
$\Delta E_{\mathrm{hh}}^{\mathrm{SCH}}$	valence band offset at the separate confinement layer	28
G	transimpedance gain of the preamplifier	25
G'	total round-trip gain	23
g_{a}	active region gain	14
g_{m}	mode-gain	14
g_{net}	net mode gain	14
g_{th}	threshold gain	23
I'	measured light intensity at the photodetector	10
I_0	emitted light intensity	10
I_{th}	threshold current	81
J_{th}	threshold current density of a laser diode	23
J_{tr}	transparency current density	22
k_{B}	Boltzmann constant	28
k_{l}	thermal conductivity	53
L	length	10
L	resonator length	14
L'	total round-trip loss excluding mirror transmission loss	23
L_{eff}	effective cavity length	15
$L_{\mathrm{eff,b}}$	penetration depth into the bottom epitaxial mirror	15
$L_{\mathrm{eff,oc}}$	penetration depth into the outcoupling mirror	15
L_{QW}	thickness of each QW	16
Δn	refractive index contrast	15
n_{C}	average refractive index of the cavity with BTJ	14
Δn_{eff}	effective refractive index induced by BTJ	37
n_{h}	high refractive index of Bragg mirror material	15
n_{l}	low refractive index of Bragg mirror material	15
N_{QW}	number of QWs	16
P_0	average optical output power	24
$\langle \Delta P \rangle$	time average of laser optical power fluctuation	24
P_{noise}	noise power at the RF-analyzer	25
P_{off}	applied electrical power at turn off	96

P_{opt}	the total optical power of a VCSEL	22
P_{ro}	applied electrical power at thermal rollover	96
P_{th}	applied electrical power at threshold	91
R	power reflectivity	15
r	amplitude reflection coefficients	14
R_{b}	reflectivity of the bottom mirror	14
R_{c}	top contact resistance	49
r_{diff}	lateral carrier diffusion length	90
R_{oc}	reflectivity of the top/outcoupling mirror	14
R_{s}	series resistance	54
R_{sub}	substrate spreading resistance	49
R_{th}	thermal resistance	91
R_{tj}	tunnel junction resistance	49
$T_{\mathrm{b,oc}}$	transmission through both top and bottom mirror	99
ΔT	temperature rise in active region w.r.t. heatsink temperature	91
T_{b}	transmissivity of the bottom epitaxial mirror	23
T_{hs}	heatsink temperature	82
T_{in}	internal temperature	95
T_{max}	maximum CW operating temperature	92
T_{oc}	transmissivity of the top outcoupling mirror	23
T_{off}	laser turn off temperature	96
T_{ro}	thermal rollover temperature	96
V	normalized frequency parameter	21
V_{th}	threshold voltage	78
w_0	spot radius	19
α	absorption coefficient	72
α_{a}	internal loss in the active region	23
α_{cl}	absorption loss in the cladding layer	23
α_{i}	internal loss	14
α_{H}	absorption coefficient in high and low index material	95
$\bar{\alpha}_{\mathrm{m}}^{\mathrm{FCA}}$	average absorption coefficient in the epitaxial mirror	95
α_{m}	mirror loss	14
β	complex propagation constant	14
η	ideality factor	78
η_{d}	differential quantum efficiency	22
η_{i}	internal quantum efficiency	28
Γ	confinement factor	14
Γ_{f}	filling factor	16
$\Gamma_{\mathrm{lateral}}$	lateral confinement factor	16
Γ_{r}	relative confinement factor	16
$\Gamma_{\mathrm{r}}^{n,p}$	relative confinement factor for tunnel junction layers	36
$\Gamma_{\mathrm{r}}^{\mathrm{act}}$	relative confinement factor for the active region	28
κ	extinction coefficient	73
λ	laser wavelength in vacuum	14
$\Delta\lambda$	wavelength tuning range	82
$\Delta\lambda_{\mathrm{l}}$	longitudinal-mode spacing	18

$\Delta\lambda_{\mathrm{bf}}$	shift of resonance wavelength by bandfilling	84
λ_{cav}	cavity resonance wavelength	101
λ_{gain}	gain-peak wavelength	101
$\Delta\lambda_{\mathrm{gc}}$	gain-cavity offset	100
$\Delta\lambda_{\mathrm{t}}$	transverse mode spacing	19
Θ_{1/e^2}	angle in rad. subtended by $1/e^2$ diameter pts. in far field	93
ρ_{c}	top p-side contact resistivity	44
ρ_{sub}	substrate resistivity	50
ρ_{tj}	tunnel junction resistivity	50

Abbreviations

BPM	beam propagation method	41
BTJ	buried tunnel junction	2
CW	continuous-wave	2
DBR	distributed Bragg reflector	9
DFB	distributed feedback	1
EEL	edge-emitting laser	18
EP	electrically-pumped	2
FCA	free-carrier absorption	6
FWHM	full-width half-maximum	28
g-J	gain-current density	100
HCG	high contrast grating	29
HRXRD	high-resolution X-ray diffraction	58
ISR	inverted surface relief	42
J-V	current density-voltage	105
L-I-T	light-current relationships vs. temperature	2
L-I-V	light output-current-voltage	2
MBE	molecular beam epitaxy	2
MIR	mid-infrared	1
MQW	multi-quantum well	22
N-MP	N-Methylpyrrolidone	65
PDS	photothermal deflection spectroscopy	32
OP	optically-pumped	7
PL	photoluminescence	28
RN	relative intensity noise	24
RT	room temperature	2
RWG	ridge waveguide	67
SMSR	side-mode suppression ratio	22
TDLAS	tunable diode laser absorption spectroscopy	1
TMM	transfer matrix method	33
VCSEL	vertical-cavity surface-emitting laser	1
WMS	wavelength modulation spectroscopy	10

Bibliography

[1] Homeland Security Newswire, "Lasers will protect helicopters from heat-seeking missiles," Sep. 2010.

[2] R. W. Waynant, I. K. Ilev, and I. Gannot, "Mid-infrared laser applications in medicine and biology," *Phil. Trans. R. Soc. Lond. A,* vol. 359, pp. 635-644, Mar. 2001.

[3] P. Werle, "A review of recent advances in semiconductor laser-based gas monitors," *Spectrochim. Acta,* vol. 54, no. 2, pp. 197–236, Feb. 1998.

[4] D. J. Bamford, D. J. Cook, S. J. Sharpe, and A. Van Pelt, "High-resolution rapidly-swept widely-tunable mid-IR spectrometer for industrial process control," in Proc. *Conference on Lasers and Electro-Optics/Quantum Electronics and Laser Science, CLEO/QELS 2006*, paper CFL3, pp. 1-2, Long Beach, USA, May 2006.

[5] H. M. Heise, "Infrared spectroscopy in medical diagnostics - advances in instrumentation for glycemic control and applications," *Polish J. of Environ. Stud.,* vol. 15, no. 4A, pp. 37-40, 2006.

[6] M. Yin, A. Krier, S. Krier, R. Jones, and P. Carrington, "Mid-infrared diode lasers for free-space optical communications," in *Advanced Free-Space Optical Communication Techniques/Applications II and Photonic Components/Architectures for Microwave Systems and Displays*, L. J. Sjöqvist, R. A. Wilson, and T. J. Merlet, (Eds.) Proc. SPIE 6399, pp. 63990C(1-6), 2006.

[7] C. B. Lens, "Applications growing for mid-IR lasers," *Photonics Spectra*, Dec. 2010.

[8] V. Ebert, "*In situ* absorption spectrometers using near-IR diode lasers and rugged multi-path-optics for environmental field measurements," in Proc. *Laser Applications to Chemical, Security and Environmental Analysis, LACSEA 2006*, paper WB1, Incline Village, USA, Feb. 2006.

[9] J. Wagner, C. Mann, M. Rattunde, and G. Weimann, "Infrared semiconductor lasers for sensing and diagnostics," *Appl. Phys. A,* vol. 78, no. 4, pp. 505-512, Feb. 2004.

[10] L. S. Rothman *et al.* "The HITRAN 2004 molecular spectroscopic database," *J. Quant. Spectrosc. Radiat. Transfer,* vol. 96, no. 2, pp. 139-204, Apr. 2005.

[11] A. Hangauer, J. Chen, R. Strzoda, M. Ortsiefer, and M.-C. Amann, "Wavelength modulation spectroscopy with a widely tunable InP-based 2.3 µm vertical-cavity surface-emitting laser," *Opt. Lett.*, vol. 33, no. 14, pp. 1566-1568, July 2008.

[12] J. Chen, A. Hangauer, R. Strzoda, and M.-C. Amann, "CO and CH_4 sensing with single mode 2.3 µm GaSb-based VCSEL," in Proc. *Conference on Lasers and Electro-Optics/International Quantum Electronics Conference, CLEO/IQEC 2009*, paper CThI, pp. 1-2, Baltimore, USA, May 2009.

[13] C. J. Vineis, C. A. Wang, and K. F. Jensen, "*In situ* reflectance monitoring of GaSb substrate oxide desorption," *J. Cryst. Growth*, vol. 225, no. 2-4, pp. 420-425, May 2001.

[14] B. R. Bennett, and B. V. Shanabrook, "Molecular beam epitaxy of Sb-based semiconductors," A. W. K. Liu, and M. B. Santos (Eds.), *Thin films : heteroepitaxial systems*, Singapore: World Scientific, 1999, pp. 401-452.

[15] V. S. Sorokin, S. V. Sorokin, A. N. Semenov, B. Ya. Meltser, and S. V. Ivanov, "Novel approach to the calculation of instability regions in GaInAsSb alloys," *J. Cryst. Growth*, vol. 216, no. 1-4, pp. 97-103, June 2000.

[16] A. Rakovska, V. Berger, X. Marcadet, B. Vinter, K. Bouzehouane, and D. Kaplan, "Optical characterization and room temperature lifetime measurements of high quality MBE-grown InAsSb on GaSb," *Semicond. Sci. Technol.,* vol. 15, no. 34, pp. 34-39, Jan. 2000.

[17] A. Garnache, A. Ouvrard, L. Cerutti, D. Barat, A. Vicet, F. Genty, Y. Rouillard, D. Romanini, and E. A. Cerda-Mendez, "2-2.7 µm single frequency tunable Sb–based lasers operating in CW at RT: Microcavity and external-cavity VCSELs, DFB," (invited), in *Semiconductor Lasers and Laser Dynamics II,* D. Lenstra, M. Pessa, and I. H. White (Eds.), Proc. SPIE 6184, pp. 61840N(1-15), 2006.

[18] H. Q. Le, C. H. Lin, S. J. Murray, R. Q. Yang, and S. S. Pei, "Effects of internal loss on power efficiency of mid-infrared InAs-GaInSb-AlSb quantum-well lasers and comparison with InAsSb lasers," *IEEE J. Quantum Electron.*, vol. 34, no. 6, pp. 1016-1030, Jun. 1998

[19] Y. Mizokawa, O. Komoda, and S. Miyase, "Long-time air oxidation and oxide-substrate reactions on GaSb, GaAs and GaP at room temperature studied by X-ray photoelectron spectroscopy," *Thin Solid Films,* vol. 156, no. 1, pp. 127-143, Jan. 1988.

[20] C. Lin, M. Grau, O. Dier, and M.-C. Amann, "Low threshold room-temperature continuous-wave operation of 2.24–3.04 µm GaInAsSb/AlGaAsSb quantum-well lasers," *Appl. Phys. Lett.,* vol. 84, no. 25, pp. 5088-5090, Jun. 2004.

[21] K. Vizbaras, and M.-C. Amann, "3.6 µm GaSb-based type-I lasers with quinternary barriers, operating at room temperature," *Electron. Lett.,* vol. 47, no. 17, pp. 980–981, Aug. 2011.

[22] D. Barat, J. Angellier, A. Vicet, Y. Rouillard, L. Le Gratiet, S. Guilet, A. Martinez, and A. Ramdane, "Antimonide-based lasers and DFB laser diodes in the 2–2.7 µm wavelength range for absorption spectroscopy," *Appl. Phys. B: Lasers and Optics,* vol. 90, no. 2, pp. 201-204, Dec. 2007.

[23] K. Rossner, M. Hummer, A. Forchel, R. Werner, and J. Koeth, "GaInAsSb/GaSb type-II distributed feedback lasers emitting in the 2.8 µm range," in Proc. *Conference on Lasers and Electro-Optics/Quantum Electronics and Laser Science, CLEO/QELS 2006*, paper CMD1, pp. 1-2, Long Beach, USA, May 2006.

[24] M. O. Fischer, M. von Edlinger, L. Nähle, J. Koeth, A. Bauer, M. Dallner, S. Höfling, L. Worschech, A. W. B. Forchel, S. Belahsene, and Y. Rouillard, "DFB lasers for sensing applications in the 3.0-3.5 µm wavelength range," in *Quantum Sensing and Nanophotonic Devices VIII*, M. Razeghi, R. Sudharsanan, and G. J. Brown (Eds.), Proc. SPIE 7945, pp. 79450E(1-13), 2011.

[25] B. Rösener, M. Rattunde, R. Moser, S. Kaspar, C. Manz, K. Köhler, and J. Wagner, "GaSb-based optically pumped semiconductor disk lasers emitting in the 2.0-2.8 µm wavelength range," in *Solid State Lasers XIX: Technology and Devices,* W. A. Clarkson, N. Hodgson, and R. K. Shori, (Eds.), Proc. SPIE 7578, pp. 75780X, Feb. 2010.

[26] A. Härkönen, A. Bachmann, S. Arafin, K. Haring, J. Viheriälä, M. D. Guina, and M.-C. Amann, "2.34 µm electrically-pumped VECSEL with buried tunnel junction," in *Semiconductor Lasers and Laser Dynamics IV*, K.P. Panayotov, M. Sciamanna, A. A. Valle, R. Michalzik (Eds.), Proc. SPIE 7720, pp. 772015(1-7), 2010.

[27] A. Ducanchez, L. Cerutti, P. Grech, and F. Genty, "Room-temperature continuous-wave operation of 2.3 µm Sb-based electrically-pumped monolithic vertical-cavity lasers," *IEEE Photon. Technol. Lett.,* vol. 20, no. 20, pp. 1745-1747, Oct. 2008.

[28] A. Ducanchez, L. Cerutti, P. Grech, F. Genty, and E. Tournie, "Mid-infrared GaSb-based EP-VCSEL emitting at 2.63 µm," *Electron. Lett.*, vol. 45, no. 5, pp. 265-267, Feb. 2009.

[29] J. Chen, "Compact laser spectroscopic gas sensors using Vertical-Cavity Surface-Emitting Lasers," *Selected Topics of Semiconductor Physics and Technology*, vol. 130, Walter Schottky Institut, Garching, Germany, 2011.

[30] C. L. Felix, W. W. Bewley, I. Vurgaftman, J. R. Meyer, L. Goldberg, D. H. Chow, and E. Selvig, "Midinfrared vertical-cavity surface-emitting laser," *Appl. Phys. Lett.*, vol. 71, no. 24, pp. 3483-3485, Dec. 1977.

[31] W. W. Bewley, C. L. Felix, I. Vurgaftman, E. H. Aifer, J. R. Meyer, L. Goldberg, J. R. Lindle, D. H. Chow, and E. Selvig, "Continuous-wave mid-infrared VCSELs," *IEEE Photon. Technol. Lett.,* vol. 10, no. 5, pp. 660-662, May 1998.

[32] A. Bachmann, K. Kashani-Shirazi, and M.-C. Amann, "GaSb-based electrically pumped VCSEL with buried tunnel junction operating continuous wave up to 50°C," in Proc. *International Semiconductor Laser Conference, ISLC 2008*, paper TuA1, pp. 39-40, Sorrento, Italy, Sep. 2008,

[33] S. Arafin, A. Bachmann, K. Kashani-Shirazi, and M.-C. Amann, "Electrically-pumped continuous-wave vertical-cavity surface-emitting lasers at 2.6 µm," *Appl. Phys. Lett.*, vol. 95, no. 13, pp. 131120(1-3), Sep. 2009.

[34] P. F. Bernath, *"Spectra of atoms and molecules",* pp. 21-41, 2nd edition, Oxford University Press, New York, 2005.

[35] J. T. C. Liu, J. B. Jeffries, and R. K. Hanson, "Wavelength modulation absorption spectroscopy with 2f detection using multiplexed diode lasers for rapid temperature measurements in gaseous flows," *Appl. Phys. B*, vol. 78, no. 3-4, pp. 503-511, Feb. 2004.

[36] R. Arndt, "Analytical line shapes for Lorentzian signals broadened by modulation," *J. Appl. Phys.*, vol. 36, no. 8, pp. 2522-2524, Aug. 1965.

[37] G. C. Bjorklund, "Frequency-modulation spectroscopy: a new method for measuring weak absorptions and dispersions," *Opt. Lett.,* vol. 5, no. 1, pp. 15-17, 1980.

[38] S. W. Corzine, R. H. Yan, and L. A. Coldren, "A tanh substitution technique for the analysis of abrupt and graded interface multilayer dielectric stacks," *IEEE J. Quantum Electron.,* vol. 27, no. 9, pp. 2086-2090, Sep. 1991.

[39] R. Michalzik, and K. J. Ebeling, in *"Vertical-cavity surface-emitting laser devices,"* H. Li and K. Iga (Eds.), Chap. 3, "Operating principles of VCSELs," Springer-Verlag, Berlin, 2003.

[40] L. A. Coldren, and E. R. Hegblom, in *Vertical-cavity surface-emitting laser design, fabrication, characterization, and applications,* C. W. Wilmsen, H. Temkin, and L. A. Coldren (Eds.), Chap. 2,"Fundamental issues in VCSEL design," Cambridge University Press, Cambridge, 1999,

[41] S. W. Corzine, R. S. Geels, J. W. Scott, R.-H. Yan, and L. A. Coldren, "Design of Fabry-Perot surface-emitting lasers with a periodic gain structure," *IEEE J. Quantum Electron.,* vol. 25, no. 6, pp. 1513-1524, June 1989.

[42] M. J. Noble, J.-H. Shin, K. D. Choquette, J. A. Lott, and L. Y.-Hee, "Calculation and measurement of resonant-mode blueshifts in oxide-apertured VCSELs," *IEEE Photon. Technol. Lett.,* vol. 10, no. 4, pp. 475-477, Apr. 1998.

[43] T. Okoshi, *"Optical fibers,"* 1st edition, Academic Press, New York, 1982.

[44] D. Gloge, "Weakly guiding fibers," *Appl. Opt.,* vol. 10, pp. 2252-2258, 1971.

[45] H. J. Unold, M. C. Riedl, S. W. Z. Mahmoud, R. Jager, and K. L. Ebeling, "Long monolithic cavity VCSELs for high singlemode output power," *Electron. Lett.,* vol. 37, no. 3, pp. 178-179, Feb. 2001

[46] E. W. Young, K. D. Choquette, J.-F. P. Seurin, S. L. Chuang, K. M. Geib, and A. A. Allerma, "Comparison of wavelength splitting for selectively oxidized, ion Implanted, and hybrid vertical-cavity surface-emitting lasers," *IEEE J. Quantum Electron.,* vol. 39, no. 5, pp. 634-639, May 2003.

[47] K. J. Ebeling, "Analysis of vertical cavity surface emitting laser diodes" in *Semiconductor Quantum Electronics*, A. Miller, M. Ebrahimzadeh, and D. M. Finlayson (Eds.), The Scottish Universities Summer School in Physics, pp. 295-338, Edinburgh, Scotland, 1998.

[48] S. W. Z. Mahmoud, "Static and Dynamic Transverse Mode Characteristics of Vertical-Cavity Surface-Emitting Semiconductor Lasers," *PhD Thesis,* Faculty of Engineering Science, University of Ulm, 2002.

[49] B. E. A. Saleh, and M. C. Teich, *"Fundamentals of photonics,"* Chap. 3, 2nd edition, Wiley, New York, 2007.

[50] L. A. Coldren, and S. W. Corzine, *Diode lasers and photonic integrated circuits,* Kai Chang (Ed.), Wiley-Interscience, New York, 1995.

[51] G. Almuneau, F. Genty, A. Wilk, P. Grech, A. Joulli, and L. Chusseau, "GaInSb/AlGaAsSb strained quantum well semiconductor lasers for 1.55 µm operation," *Semicond. Sci. Technol.,* vol. 14, no. 1, pp. 89-92, Jan. 1999.

[52] M. Grau, C. Lin, O. Dier, C. Lauer, and M.-C. Amann, "Room-temperature operation of 3.26 µm GaSb-based type-I lasers with quinternary AlGaInAsSb barriers," *Appl. Phys. Lett.,* vol. 87, no. 24, pp. 241104(1-3), Dec. 2005.

[53] M. Ortsiefer, "Langwellige Vertikalresonator-Laserdioden im Materialsystem InGaAlAs/InP," *Selected Topics of Semiconductor Physics and Technology*, vol. 35, Walter Schottky Institut, Garching, Germany, 2000.

[54] W. Hofmann, C. Chase, M. Müller, Y. Rao, C. Grasse, G. Böhm, M.-C. Amann, and C. J. Chang-Hasnain, "Long-wavelength high-contrast grating vertical-cavity surface-emitting laser," *IEEE Photon. J.,* vol. 2, no. 3, pp. 415-422, June 2010.

[55] O. Dier, "Das Materialsystem (AlGaIn)(AsSb): Eigenschaften und Eignung für GaSb-basierte Vertikalresonator-Laserdioden," *Selected Topics of Semiconductor Physics and Technology*, vol. 93, Walter Schottky Institut, Garching, Germany, 2008.

[56] O. Dier, C. Reindl, A. Bachmann, C. Lauer, T. Lim, K. Kashani-Shirazi, and M.-C. Amann, "Reduction of hetero-interface resistivity in *n*-type AlAsSb/GaSb distributed Bragg reflectors," *Semicond. Sci. Technol.,* vol. 23, no. 2, pp. 1-4, Jan. 2008.

[57] M. Born, and E. Wolf, *Principles of optics,* 6th edition, Pergamon Press, Oxford, 1989.

[58] C. Lauer, "Antimonid-basierte Vertikalresonator-Laserdioden für Wellenlängen oberhalb 2 µm," *Selected Topics of Semiconductor Physics and Technology*, vol. 116, Walter Schottky Institut, Garching, Germany, 2008.

[59] A. Bachmann, "Antimonide-Based Vertical-Cavity Surface-Emitting Lasers," *Selected Topics of Semiconductor Physics and Technology*, vol. 133, Walter Schottky Institut, Garching, Germany, 2011.

[60] Nextnano++: http://www.nextnano.de (2009).

[61] O. Dier, S. Dachs, M. Grau, C. Lin, C. Lauer, and M.-C. Amann, "Effects of thermal annealing on the band gap of GaInAsSb," *Appl. Phys. Lett.,* vol. 86, no. 15, pp. 15112(1-3), Apr. 2005.

[62] W. W. Chow, M. H. Crawford, and R. P. Schneider, Jr., "Minimization of threshold current in short wavelength AlGaInP vertical-cavity surface-emitting lasers," *IEEE J. Sel. Top. Quantum Electron.,* vol. 1, no. 2, pp. 649-653, June 1995.

[63] D. Feezell, D. A. Buell, D. Lofgreen, M. Mehta, and L. A. Coldren, "Optical design of InAlGaAs low-loss tunnel-junction apertures for long-wavelength vertical-cavity lasers," *IEEE J. Quantum Electron.,* vol. 42, no. 5, pp. 494-499, May 2006.

[64] B. Weigl, M. Grabherr, C. Jung, R. Jager, G. Reiner, R. Michalzik, D. Sowada, and K. J. Ebeling, "High-performance oxide-confined GaAs VCSELs," *IEEE J. Sel. Top. Quantum Electron.,* vol. 3, no. 2, pp. 409-415, Apr. 1997.

[65] G. R. Hadley, "Effective index model for vertical-cavity surface-emitting lasers," *Opt. Lett.,* vol. 20, no. 13, pp. 1483-1485, Mar. 1995.

[66] M. Brunner, K. Gulden, R. Hövel, M. Moser, and M. Ilegems, "Thermal lensing effects in small oxide confined vertical-cavity surface-emitting lasers," *Appl. Phys. Lett.,* vol. 76, no. 1, pp. 7-9, Jan. 2000.

[67] J. Y. Law, "Static, dynamic, and noise characteristics of vertical-cavity surface-emitting lasers," *Ph.D. dissertation,* School of Eng. and Appl. Sci., Univ. Rochester, Rochester, NY, 1997.

[68] SimWindows: Version 1.5.0, University of Colorado Boulder 1999
http://www.simwindows.com

[69] I. Vurgaftman, J. R. Meyer, and L. R. Ram-Mohan, "Band parameters for III-V compound semiconductors and their alloys," *J. Appl. Phys.,* vol. 89, no. 1, pp. 5815-5875, Feb. 2001.

[70] J. Bengtsson, J. Gustavsson, Å. Haglund, A. Larsson, A. Bachmann, K. Kashani-Shirazi, and M.-C. Amann, "Diffraction loss in long-wavelength buried tunnel junction VCSELs analyzed with a hybrid coupled-cavity transfer-matrix mode," *Opt. Express,* vol. 16, no. 25, pp. 20789-20802, Dec. 2008.

[71] D. I. Babic, Y. Chung, N. Dagli, and J. E. Bowers, "Modal reflection of quarter-wave mirrors in vertical-cavity lasers," *IEEE J. Quantum Electron.*, vol. 29, no. 6, pp. 1950-1962, June 1993.

[72] J. W. Goodman, *Introduction to fourier optics,* 2nd edition, McGraw-Hill, New York, 1996.

[73] Å. Haglund, J. S. Gustavsson, J. Vukusic, P. Modh, and A. Larsson, "Single fundamental-mode output power exceeding 6 mW from VCSELs with a shallow surface relief," *IEEE Photon. Technol. Lett.,* vol. 16, no. 2, pp. 368-370, Feb. 2004.

[74] S. Arafin, A. Bachmann, K. Vizbaras, J. Gustavsson, A. Larsson, and M.-C. Amann, "Large-area single-mode GaSb-based VCSELs using an inverted surface relief," in Proc. *23rd Annual Meeting of the IEEE Photonics Society*, paper MI3, pp. 61-62, Denver, USA, Nov. 2010.

[75] J. A. Robinson, and S. E. Mohney, "Characterization of sulfur passivated n-GaSb using transmission electron microscopy and the influence of passivation on ohmic contact resistance," *J. Appl. Phys.,* vol. 96, no. 5, pp. 2684-2688, June 2004.

[76] T. D. Veal, M. J. Lowe, and C. F. McConville, "HREELS and photoemission study of GaSb(100)-(1×3) surfaces prepared by optimal atomic hydrogen cleaning," *Surf. Sci.,* vol. 499, no. 2-3, pp. 251-260, Mar. 2002.

[77] T. H. Chiu, J. A. Ditzenberger, H. S. Luftman, W. T. Tsang, and N. T. Ha, "Te doping study in molecular beam epitaxial growth of GaSb using Sb_2Te_3," *Appl. Phys. Lett.,* vol. 56, no. 17, pp. 1688-1690, Feb. 1990.

[78] A. Vogt, A. Simon, H. L. Hartnagel, J. Schikora, V. Buschmann, M. Rodewald, H. Fuess, S. Fascko, C. Koerdt, and H. Kurz, "Ohmic contact formation mechanism of the PdGeAu system on n-type GaSb grown by molecular beam epitaxy," *J. Appl. Phys.,* vol. 83, no. 12, pp. 7715-7719, Mar. 1998.

[79] Z. C. Yang, P. H. Hao, and L. C. Wang, "Au/In/Pd/Te/Pd ohmic contact to n-GaSb," *Electron. Lett.,* vol. 32, no. 25, pp. 2348-2349, Dec. 1996.

[80] J. A. Robinson, and S. E. Mohney, "A low-resistance, thermally stable ohmic contact to n-GaSb," *J. Appl. Phys.,* vol. 98, no. 3, pp. 033703(1-6), Aug. 2005.

[81] O. Dier, M. Grau, C. Lauer, C. Lin, and M.-C. Amann, "Diffusion of dopants in highly ($\sim 10^{20}$ cm^{-3}) n- and p-doped GaSb-based materials," *J. Vac. Sci. Technol. B,* vol. 23, no. 2, pp. 349-353, Mar. 2005.

[82] D. Y. Petrovykh, M. J. Yang, and L. J. Whitman, "Chemical and electronic properties of sulfur-passivated InAs surfaces," *Surf. Sci.,* vol. 523, no. 3, pp. 231-240, Jan. 2003.

[83] A. Subekti, V. W. L. Chin, and T. L. Tansley, "Ohmic contacts to n-type and p-type GaSb," *Solid-State Electron.,* vol. 39, no. 3, pp. 329-332, Mar. 1996.

[84] C. Lauer, O. Dier, and M.-C. Amann,"Low-resistive metal/n^+-InAsSb/n-GaSb contacts," *Semicond. Sci. Technol.,* vol. 21, no. 9, pp. 1274-1277, July 2006.

[85] J. G. Champlain, R. Magno, and J. B. Boos,"Low resistance unannealed ohmic contacts to n-type $InAs_{0.66}Sb_{0.34}$," *Electron. Lett.,* vol. 43, no. 23, pp. 1315-1317, July 2007.

[86] G. Franz, and M.-C. Amann, "Extremely low contact resistivity of Ti/Pt/Au contacts on p^+-InGaAs as determined by a new evaluation method," *J. Electrochem. Soc.,* vol. 140, no. 3, pp. 847-850, Mar. 1993.

[87] X. Y. Gong, T. Yamaguchi, H. Kan, T. Makino, K. Ohshimo, M. Aoyama, M. Kumagawa, N. L. Rowell, and R. Rinfret, "Sulphur passivation of InAs(Sb)," *Appl. Surf. Sci.,* vol. 113/114, pp. 388-392, Apr. 1997.

[88] D. B. Suyatin, C. Thelander, M. T. Björk, I. Maximov, and L. Samuelson, "Sulfur passivation for ohmic contact formation to InAs nanowires," *Nanotech.,* vol. 18, no. 10, pp. 105307(1-5), Feb. 2007.

[89] E. Papis, A. Piotrowska, E. Kaminska, K. Golaszewska, W. Jung, J. Katcki, A. Kudla, M. Piskorski, and T. T. Piotrowski, "Sulfide treatment of GaSb surface: influence on the LPE growth of InGaAsSb/AlGaAsSb heterostructures," *Vacuum,* vol. 57, no. 2, pp. 171-178, May 2000.

[90] C. Lauer, M. Ortsiefer, R. Shau, J. Rosskopf, G. Böhm, R. Meyer, and M.-C. Amann, "InP-based longwavelength vertical-cavity surface-emitting lasers with buried tunnel junction," *Phys. Stat. Sol.* (C) vol. 1, no. 8, pp. 2183-2209, June, 2004.

[91] http://www.comsol.com/

[92] S. Adachi, "Lattice thermal conductivity of group-IV and III-V semiconductor alloys," *J. Appl. Phys.*, vol. 102, no. 6, pp. 063502(1-7), Sep. 2007.

[93] T. Borca-Tasciuca, D. W. Song, J. R. Meyer, I. Vurgaftman, M.-J. Yang, B. Z. Noshob, L. J. Whitman, and G. Chen, "Thermal conductivity of $AlAs_{0.07}Sb_{0.93}$ and $Al_{0.9}Ga_{0.1}As_{0.07}Sb_{0.93}$ alloys and $(AlAs)_1/(AlSb)_{11}$ digital-alloy superlattices," *J. Appl. Phys.*, vol. 92, no. 9, pp. 4994-4998, Nov. 2002.

[94] M. Osinski, and W. Nakwaski, "Effective thermal conductivity analysis of 1.55 µm InGaAsP/InP vertical-cavity top-surface emitting microlasers," *Electron. Lett.*, vol. 29, no. 11, pp. 1015-1016, May 1993.

[95] M. Müller, W. Hofmann, G. Böhm, and M.-C. Amann, "Short-cavity long-wavelength VCSELs with modulation bandwidths in excess of 15 GHz," *IEEE Photon. Technol. Lett.,* vol. 21, no. 21 pp. 1615-1617, Nov. 2009.

[96] I. Hallakoun, T. Boterashvili, G. Bunin, and Y. Shapira, "Electrochemical etching impact on GaAs process, mask design and device performance," *2000 GaAs Mantech Conference, Digest of Papers,* pp. 25-27, May 2000.

[97] M. Hagio, "Electrode reaction of GaAs metal semiconductor field-effect transistors in deionized water," *J. Electrochem. Soc.,* vol. 140, no. 8, pp. 2402-2405, Aug. 1993.

[98] K. Kashani-Shirazi, K. Vizbaras, A. Bachmann, S. Arafin, and M.-C. Amann, "Low-threshold strained quantum-well GaSb-based lasers emitting in the 2.5 to 2.7 µm wavelength range," *IEEE Photon. Technol. Lett.,* vol. 21, no. 16, pp. 1106-1108, Aug. 2009.

[99] M. J. Mondry, D. I. Babic, J. E. Bowers, and L. A. Coldren, "Refractive indexes of (Al, Ga, In)As epilayers on InP for optoelectronic applications," *IEEE Photon. Technol. Lett.*, vol. 4, no. 6, pp. 627-630, June 1992.

[100] W. B. Jackson, N. M. Amer, A. C. Boccara, and D. Fournier, "Photothermal deflection spectroscopy and detection," *Appl. Opt.,* vol. 20, no. 8, pp. 1333-1344, 1981.

[101] E. C. Freeman, and W. Paul, "Optical constants of rf sputtered hydrogenated amorphous Si," *Phys. Rev. B*, vol. 20, no. 2, pp. 716–728, July, 1979.

[102] P. Barnes, and T. Paoli, "Derivative measurements of the current-voltage characteristics of double-heterostructure injection lasers," *IEEE J. Quantum Electron.,* vol. 12, no. 10, pp. 633-639, Oct. 1976.

[103] M. J. Adams, and P. T. Landsberg, in *"Gallium arsenide lasers,"* C. H. Gooch (Ed.), "The theroy of the injection lasers," Willey-Interscience, New York, 1969.

[104] R. Michalzik, M. Grabherr, R. Jaeger, M. Miller, and K. J. Ebeling,"Progress in high-power VCSELs and arrays," (invited), in *Optoelectronic Materials and Devices*, M. Osinski, and Y.-K. Su, (Eds.) Proc. SPIE 3419, pp. 187-195, 1998.

[105] G. K. Reeves, and H. B. Harrison, "Obtaining the specific contact resistance from transmission line model measurements," *IEEE Electron Dev. Lett.,* vol. 3, no. 5, pp. 111-113, May 1982.

[106] D. F. Siriani, P. O. Leisher, and K. D. Choquette, "Loss-induced confinement in photonic crystal vertical-cavity surface-emitting lasers," *IEEE J. Quantum Electron.,* vol. 45, no. 7, pp. 762-768, July 2009.

[107] R. Michalzik, and K. J. Ebeling, "Generalized BV diagrams for higher order transverse modes in planar vertical-cavity laser diodes," *IEEE J. Quantum Electron.*, vol. 31, no. 8, pp. 1371-1379, Aug. 1995.

[108] D. G. Deppe, and Q. Deng, "Self-consistent eigenmode analysis of the dielectrically-apertured Fabry-Perot microcavity," *Appl. Phys. Lett.*, vol. 71, no. 2, pp. 160-162, July 1997.

[109] M. Mochizuki, T. Nishida, S. Kakinuma, and T. Kaneko, "FDTD calculations of the divergence angle of multi-mode VCSELs," in *Physics and Simulation of Optoelectronic Devices XII*, M. Osinski, F. Henneberger, and H. Amano, (Eds.), Proc. SPIE 5722, pp. 201-210, 2005.

[110] K. L. Lear, R. P. Schneider, Jr., K. D. Choquette, and S. P. Kilcoyne, "Index guiding dependent effects in implant and oxide confined vertical-cavity lasers," *IEEE Photon. Technol. Lett.*, vol. 8, no. 6, pp. 740-742, June 1996.

[111] S. Arafin, A. Bachmann, and M.-C. Amann, "Transverse-mode characteristics of GaSb-based VCSEL with buried tunnel junctions," *IEEE J. Sel. Top. Quantum Electron.*, pp. 1-9, 2011, in press. Online doi:10.1109/JSTQE.2011.2107571

[112] A. N. A.-Omari, and K. L. Lear, "VCSELs with a self-aligned contact and copper-plated heatsink," *IEEE Photon. Technol. Lett.*, vol. 17, no. 9, pp. 1767-17697, Sep. 2005.

[113] R. F. Fischer, and B. Tadic, *"Optical system design,"* 1st edition, Chap. 11, McGraw-Hill, New York, 2000.

[114] A. Perona, A. Garnache, L. Cerutti, A. Ducanchez, S. Mihindou, P. Grech, G. Boissier, and F. Genty, "AlAsSb/GaSb doped distributed Bragg reflectors for electrically pumped VCSELs emitting around 2.3 µm," *Semicond. Sci. Technol.,* vol. 22, no. 10, pp. 1140-1144, Sept. 2007.

[115] A. Hangauer, J. Chen, and M.-C. Amann, "Vertical-cavity surface-emitting laser light–current characteristic at constant internal temperature," *IEEE Photon. Technol. Lett.*, vol. 23, no. 18, pp. 1295-1297, Sept. 2011.

[116] G. M. Yang, M. H. MacDougal, V. Pudikov, and P. D. Dapkus, "Influence of mirror reflectivity on laser performance of very-low-threshold vertical-cavity surface-emitting lasers," *IEEE Photon. Technol. Lett.*, vol. 7, no. 11, pp. 1228-1230, Nov. 1995.

[117] C. Bückers, A. Thränhardt, S. W. Koch, M. Rattunde, N. Schulz, J. Wagner, J. Hader, and J. V. Moloney, "Microscopic calculation and measurement of the

laser gain in a (GaIn)Sb quantum well structure," *Appl. Phys. Lett.,* vol. 92, no. 7, pp. 071107(1-3), Feb. 2008.

[118] J. Piprek, Y. A. Akulova, D. I. Babic, L. A. Coldren, and J. E. Bowers, "Minimum temperature sensitivity of 1.55 µm vertical-cavity lasers at -30 nm gain offset," *Appl. Phys. Lett.*, vol. 72, no. 15, pp. 1814-1816, Feb. 1998.

[119] S. Mogg, N. Chitica, U. Christiansson, R. Schatz, P. Sundgren, C. Asplund, and M. Hammar, "Temperature sensitivity of the threshold current of long-wavelength InGaAs-GaAs VCSELs with large gain-cavity detuning," *IEEE J. Quantum Electron.,* vol. 40, no. 5, pp. 453-462, May 2004.

[120] J. D. Evans, J. G. Simmons, D. A. Thompson, N. Puetz, T. Makino, and G. Chik, "An investigation into the temperature sensitivity of strained and unstrained multiple quantum-well, long wavelength lasers: new insight and methods of characterization," *IEEE J. Sel. Top. Quantum Electron.,* vol. 1, no. 2, pp. 275-284, June 1995.

[121] E. R. T. Kerstel, R. Q. Iannone, M. Chenevier, S. Kassi, H.-J. Jost, and D. Romanini, "A water isotope (^{2}H, ^{17}O, and ^{18}O) spectrometer based on optical feedback cavity-enhanced absorption for in situ airborne applications," *Appl. Phys. B, Lasers Opt.*, vol. 85, no. 2–3, pp. 397-406, July 2006.

[122] K. Vizbaras, M. Törpe, S. Arafin, and M.-C. Amann, "Ultra-low resistive GaSb/InAs tunnel junctions," *Semicond. Sci. Technol.,* vol. 26, no. 7, pp. 075021(1-4), Apr. 2011

[123] J. M. Yarborough, Yi-Ying Lai, Y. Kaneda, J. Hader, J. V. Moloney, T. J. Rotter, G. Balakrishnan, C. Hains, D. Huffaker, S. W. Koch, and R. Bedford, "Record pulsed power demonstration of a 2 µm GaSb-based optically pumped semiconductor laser grown lattice-mismatched on an AlAs/GaAs Bragg mirror and substrate," *Appl. Phys. Lett.*, vol. 95, no. 8, pp. 081112(1-3), Aug. 2009.

[124] M. Mehta, A. Jallipalli, J. Tatebayashi, M. N. Kutty, A. Albrecht, G. Balakrishnan, L. R. Dawson, and D. L. Huffaker, "Room-temperature operation of buffer-free GaSb–AlGaSb quantum-well diode lasers grown on a GaAs platform emitting at 1.65 µm," *IEEE Photon. Technol. Lett.*, vol. 19, no. 20, pp. 1628-1630, Oct. 2007.

[125] J. Tatebayashi, A. Jallipalli, M. N. Kutty, S. H. Huang, G. Balakrishnan, L. R. Dawson, and D. L. Huffaker, "Room-temperature lasing at 1.82 µm of GaInSb/AlGaSb quantum wells grown on GaAs substrates using an interfacial misfit array," *Appl. Phys. Lett.*, vol. 91, no. 14, pp. 141102(1-3), Oct. 2007.

[126] J. B. Rodriguez, L. Cerutti, and E. Tournie, "GaSb-based, 2.2 µm type-I laser fabricated on GaAs substrate operating continuous wave at room temperature," *Appl. Phys. Lett.*, vol. 94, no. 2, pp. 023506(1-2), Jan. 2009.

[127] M. Maute, "Mikromechanisch abstimmbare Laser-Dioden mit Vertikalresonator," *Selected Topics of Semiconductor Physics and Technology*, vol. 81, Walter Schottky Institut, Garching, Germany, 2006.

[128] C. Gierl, T. Gruendl, P. Debernardi, K. Zogal, C. Grasse, H. A. Davani, G. Boehm, S. Jatta, F. Kuppers, P. Meißner, and M.-C. Amann, "Surface micromachined tunable 1.55 µm-VCSEL with 102 nm continuous single-mode tuning," *Opt. Express,* vol. 19, no. 18, pp. 17336-17343, Aug. 2011.

Awards and Publications

Awards

- Recipient of the IEEE Photonics Society Graduate Student Fellowship 2011 for a strong record of research accomplishments and excellent academic records.
- Best Student Paper Award (Second Place) in the 23rd Annual Meeting of the IEEE Photonics Society 2010 in Denver, CO, USA.

List of Publications

(The all mentioned papers in this list have evolved from this work)

First-authored

Journal/Magazine

- **S. Arafin**, A. Bachmann, K. Vizbaras, A. Hangauer, J. Gustavsson, J. Bengtsson, A. Larsson, and M.-C. Amann, "Comprehensive analysis of electrically-pumped GaSb-based VCSELs," *Opt. Express*, vol. 19, no. 18, pp. 17267-17282, Aug. 2011.
- **S. Arafin**, A. Bachmann, and M.-C. Amann, "Transverse-mode characteristics of GaSb-based VCSEL with buried tunnel junctions," *IEEE J. Sel. Top. Quantum Electron.*, vol. 17, no. 6, pp. 1576-1583, Mar. 2011.
- **S. Arafin**, and M.-C. Amann, "Antimony-based tunable diode lasers for trace-gas sensing," *Fire & Safety Group Magazine,* FS-World Newsletter, Aug. 2010.
- **S. Arafin**, A. Bachmann, K. Kashani-Shirazi, and M.-C. Amann, "Electrically-pumped continuous-wave vertical-cavity surface-emitting lasers at ∼2.6 µm," *Appl. Phys. Lett.*, vol. 95, no. 13, pp. 131120(1-3), Oct. 2009.
- **S. Arafin**, A. Bachmann, K. Kashani-Shirazi, S. Priyabadini, and M.-C. Amann, "Low-resistive sulphur-treated ohmic contacts to *n*-type InAsSb," *IET Optoelectron.*, vol. 3, no. 6, pp. 259-263, Dec. 2009.

Conference Contributions

- **S. Arafin**, K. Klein, K. Vizbaras, and M.-C. Amann, "*a*-Ge and *a*-Si as dielectric mirror materials for long wavelength optoelectronics devices: a comparative study," *25th Semiconductor Integrated Optoelectronics Conference, SIOE 2011*, Cardiff, UK, Apr. 2011.
- **S. Arafin**, A. Bachmann, K. Vizbaras, J. Gustavsson, A. Larsson, and M.-C. Amann, "Large-area single-mode GaSb-based VCSELs using an inverted surface relief," *23rd Annual Meeting of the IEEE Photonics Society 2010*, Denver, CO, USA, Nov. 2010. (Best Student Paper Award, 2nd place)

- **S. Arafin**, M. Mueller, and M.-C. Amann, "InP-based high-speed VCSELs for optical interconnects," (invited), Workshop on *Progress in light source for optical interconnection* within *22nd IEEE International Semiconductor Laser Conference, ISLC 2010*, Kyoto, Japan, Sep. 2010.

- **S. Arafin**, A. Bachmann, K. Vizbaras, and M.-C. Amann, "Large-aperture single-mode GaSb-based BTJ-VCSELs at 2.62 µm," *22nd IEEE International Semiconductor Laser Conference, ISLC 2010*, Kyoto, Japan, Sep. 2010.

- **S. Arafin**, A. Bachmann, K. Kashani-Shirazi, and M.-C. Amann, "Continuous-wave electrically-pumped GaSb-based VCSELs at ∼2.6 µm operating up to 50°C," *22nd Annual Meeting of the IEEE Photonics Society 2009*, Belek-Antalya, Turkey, Oct. 2009.

- **S. Arafin**, A. Bachmann, K. Kashani-Shirazi, and M.-C. Amann, "Continuous-wave single-mode electrically-pumped GaSb-based VCSELs at 2.5 µm," *8th Pacific Rim Conference on Lasers and Electro-Optics, CLEO/Pacific Rim 2009*, Shanghai, China, Sept. 2009.

- **S. Arafin**, A. Bachmann, K. Kashani-Shirazi, S. Priyabadini, and M.-C. Amann, "Low-resistive ohmic contacts to n-$InAs_{0.91}Sb_{0.09}$ for GaSb-based VCSELs in the mid-infrared range," *23rd Semiconductor Integrated Optoelectronics Conference, SIOE 2009*, Cardiff, UK, Apr. 2009.

Conference Proceedings

- **S. Arafin**, A. Bachmann, K. Vizbaras, J. Gustavsson, A. Larsson, and M.-C. Amann, "Large-area single-mode GaSb-based VCSELs using an inverted surface relief," in Proc. *23rd Annual Meeting of the IEEE Photonics Society 2010*, paper MI3, pp. 61-62, Denver, USA, Nov. 2010.

- **S. Arafin**, A. Bachmann, K. Vizbaras, and M.-C. Amann, "Large-aperture single-mode GaSb-based BTJ-VCSELs at 2.62 µm," in Proc. *22nd IEEE International Semiconductor Laser Conference, ISLC 2009*, paper TuB4, pp. 47-48, Kyoto, Japan, Sep. 2010.

- **S. Arafin**, A. Bachmann, K. Kashani-Shirazi, and M.-C. Amann, "Continuous-wave electrically-pumped GaSb-based VCSELs at ∼2.6 µm operating up to 50°C," in Proc. *22nd Annual Meeting of the IEEE Photonics Society 2009*, paper ThBB2, pp. 837-838, Belek-Antalya, Turkey, Oct. 2009.

- **S. Arafin**, A. Bachmann, K. Kashani-Shirazi, and M.-C. Amann, "Continuous-wave single-mode electrically-pumped GaSb-based VCSELs at 2.5 µm," in Proc. *8th Pacific Rim Conference on Lasers and Electro-Optics, CLEO/Pacific Rim 2009*, paper WG4-2, pp. 1-2, Shanghai, China, Sept. 2009.

Co-authored

Journal/Magazine

- K. Vizbaras, M. Toerpe, **S. Arafin**, and M.-C. Amann, "Ultra-low resisitve GaSb/InAs tunnel junctions," *Semicond. Sci. Technol.,* vol. 26, no. 7, pp. 07502(1-4), Apr. 2011.
- K. Vizbaras, A. Bachmann, **S. Arafin**, K. Saller, S. Sprengel, G. Boehm, R. Meyer, and M.-C. Amann, "MBE growth of low threshold GaSb-based lasers with emission wavelengths in the range of 2.5 to 2.7 µm," *J. Cryst. Growth*, vol. 323, no. 1, pp. 446-449, Dec. 2010.
- A. Bachmann, **S. Arafin**, and K. Kashani-Shirazi, "Single-mode electrically-pumped GaSb-based VCSELs emitting continuous-wave at 2.4 and 2.6 µm," (invited), *New J. Phys.*, vol. 11, no. 12, pp. 125014-(1-17), Dec. 2009.
- K. Kashani-Shirazi, K. Vizbaras, A. Bachmann, **S. Arafin**, and M.-C. Amann, "Low-threshold strained quantum-well GaSb-based lasers emitting in the 2.5- to 2.7 µm wavelength range," *IEEE Photon. Technol. Lett.,* vol. 21, no. 16, pp. 1106-1108, June 2009.
- A. Bachmann, K. Kashani-Shirazi, **S. Arafin**, and M.-C. Amann, "GaSb-based VCSEL with buried tunnel junction for emission around 2.3 µm," *IEEE J. Sel. Top. Quantum Electron.*, vol. 15, no. 3, pp. 933-940, June 2009.

Talks/Presentations

- M.-C. Amann, A. Bachmann, **S. Arafin**, and K. Vizbaras, "Recent progress on GaSb-based single-mode VCSELs," *VCSEL Day 2010*, Torino, Italy, May 2010.

Conference Contributions

- A. B. Ikyo, I. P. Marko, K. Hild, A. R. Adams, S. J. Sweeney, **S. Arafin**, and M.-C. Amann, "Temperature dependence of 2.3 µm and 2.6 µm GaInAsSb based BTJ-VCSELs and edge emitting lasers," in *SPIE Photonics West 2012,* Conf. on *Novel In-Plane Semiconductor Lasers XI*, San Francisco, USA, Jan. 2012.
- A. B. Ikyo, I. P. Marko, K. Hild, A. R. Adams, S. J. Sweeney, **S. Arafin**, and M.-C. Amann, "Gain-cavity tuning and non-radiative recombination in 2.6 µm GaInAsSb VCSEL," *UK Semiconductors 2011*, Sheffield, UK, July 2011.
- A. B. Ikyo, I. P. Marko, A. R. Adams, S. J. Sweeney, **S. Arafin**, and M.-C. Amann, "Wavelength dependence of the performance of GaInAsSb/GaSb mid-infrared lasers," *UK Semiconductors 2011*, Sheffield, UK, July 2011, Poster.
- K. Vizbaras, A. Andrejew, A. Vizbaras, C. Grasse, **S. Arafin**, and M.-C. Amann, "Low-Threshold 3 µm GaInAsSb/AlGaInAsSb quantum-well lasers operating in continuous wave up to 64°C," *Indium Phosphide and Related Materials, IPRM 2011*, Berlin, Germany, May 2011.

- M. Ortsiefer, C. Neumeyr, J. Rosskopf, **S. Arafin**, G. Boehm, A. Hangauer, J. Chen, R. Strzoda, and M.-C. Amann, "GaSb and InP-based VCSELs at 2.3 µm emission wavelength for tunable diode laser spectroscopy of carbon monoxide," (invited), in *SPIE Photonics West 2011,* Conf. on *Quantum Cascade Lasers and Applications II*, San Francisco, USA, Jan. 2011.

- M.-C. Amann, **S. Arafin**, and K. Vizbaras, "Single-mode and tunable GaSb-based VCSELs for wavelengths above 2 µm," (invited), in *SPIE Photonics West 2011,* Conf. on *VCSEL Sensors and Applications*, San Francisco, USA, Jan. 2011.

- M.-C. Amann, and **S. Arafin**, "GaSb-based wavelength-tunable single-mode VCSELs for the 2-3 µm wavelength range," (invited), *10th International Conference on Mid-Infrared Optoelectronics, IC-MIOMD-X 2010*, Shanghai, China, Sep. 2010.

- K. Vizbaras, A. Bachmann, **S. Arafin**, K. Saller, S. Sprengel, G. Boehm, R. Meyer, and M.-C. Amann, "MBE growth of low threshold GaSb-based lasers with emission wavelengths in the range of 2.5 to 2.7 µm," *16th International Conference on Molecular Beam Epitaxy, MBE 2010*, Berlin, Germany, Aug. 2010.

- K. Vizbaras, A. Bachmann, **S. Arafin**, and M.-C. Amann, "Recent progress on electrically pumped single-mode GaSb-based VCSELs emitting around 2.3 µm and 2.6 µm," *International workshop on opportunities and challenges in mid-infrared laser-based gas sensing, MIRSENS 2010*, Wroclaw, Poland, May 2010.

- A. Härkönen, A. Bachmann, **S. Arafin**, K. Haring, J. Viheriälä, M. D. Guina, and M.-C. Amann, "2.34 µm electrically-pumped VECSEL with buried tunnel junction," in *SPIE Photonics Europe,* Conf. on *Nanolasers and VECSELs*, Brussels, Belgium, Apr. 2010.

- A. Bachmann, **S. Arafin**, K. Kashani-Shirazi, and M.-C. Amann, "Long wavelength electrically-pumped GaSb-based buried tunnel junction VCSELs," *14th International Conference on Narrow Gap Semiconductors and Systems, NGSS 2009*, Sendai, Japan, July 2009.

- S. Priyabadini, **S. Arafin**, A. Bachmann, K. Kashani-Shirazi, and M.-C. Amann, "Low-resistive thermally-stable metal-semiconductor contacts on n-GaSb using n-InAsSb contact layer," *International Conference on Frontiers of Physics, IFCP 2009*, Kathmandu, Nepal, June 2009.

- K. Kashani-Shirazi, A. Bachmann, **S. Arafin**, K. Vizbaras, and M.-C. Amann, "Ultra-low threshold GaSb-based laser diodes at 2.65 µm," *Conference on Lasers and Electro-Optics/International Quantum Electronics Conference, CLEO/IQEC 2009*, Baltimore, USA, May 2009.

- K. Kashani-Shirazi, A. Bachmann, **S. Arafin**, K. Vizbaras, S. Ziegler, and M.-C. Amann, "Optimized MBE growth technique for GaSb-based edge emitters at 2.7 µm," *Euro MBE 2009*, Zacopane, Poland, Mar. 2009.

- K. Kashani-Shirazi, G. Boehm, A. Bachmann, **S. Arafin**, S. Ziegler, and M.-C. Amann, "MBE growth of active regions for electrically-pumped, cw-operating GaSb-based

VCSELs," *The 15th International Conference on molecular beam epitaxy, MBE 2008*, Vancouver, Canada, Aug. 2008.

- K. Kashani-Shirazi, A. Bachmann, **S. Arafin**, S. Ziegler, and M.-C. Amann, "Simulation of active regions for GaSb-based VCSELs," *International Nano-Optoelectronics Workshop, i-NOW 2008*, Tokyo, Japan, Aug. 2008.

Conference Proceedings

- M. Ortsiefer, C. Neumeyr, J. Rosskopf, **S. Arafin**, G. Boehm, A. Hangauer, J. Chen, R. Strzoda, and M.-C. Amann, "GaSb and InP-based VCSELs at 2.3 µm emission wavelength for tunable diode laser spectroscopy of carbon monoxide," (invited), in *Quantum Sensing and Nanophotonic Devices VIII*, M. Razeghi, R. Sudharsanan, and G. J. Brown, (Eds.) Proc. SPIE 7945, pp. 794509(1-7), 2011.

- K. Vizbaras, **S. Arafin**, and M.-C. Amann, "Single mode and tunable GaSb-based VCSELs for wavelengths above 2 µm," in *Vertical-Cavity Surface-Emitting Lasers XV*, J. K. Guenter, and C. Lei, (Eds.), Proc. SPIE 7952, pp. 79520D(1-7), 2011.

- A. Härkönen, A. Bachmann, **S. Arafin**, K. Haring, J. Viheriälä, M. D. Guina, and M.-C. Amann, "2.34 µm electrically-pumped VECSEL with buried tunnel junction," in *Semiconductor Lasers and Laser Dynamics IV*, K.P. Panayotov, M. Sciamanna, A.A. Valle, and R. Michalzik, (Eds.), Proc. SPIE 7720, pp. 772015(1-7), 2010.

- A. Bachmann, **S. Arafin**, K. Kashani-Shirazi, and M.-C. Amann, "Long wavelength electrically-pumped GaSb-based buried tunnel junction VCSELs," in Proc. *14th International Conference on Narrow Gap Semiconductors and Systems NGSS 2009,* published in *Physics Procedia*, vol. 3, no. 2, pp. 1155-1159, Sendai, Japan, July 2009.

- K. Kashani-Shirazi, A. Bachmann, **S. Arafin**, K. Vizbaras, and M.-C. Amann, "Ultra-low threshold GaSb-based laser diodes at 2.65 µm," in Proc. *Conference on Lasers and Electro-Optics/International Quantum Electronics Conference, CLEO/IQEC 2009*, paper CTuGG5, pp. 1-2, Baltimore, USA, May 2009.

Acknowledgments

At first, all praise to **GOD**, the most Gracious and the most Merciful, whose help and guidance is ever dominating throughout my life.

I would like to express the sincere gratitude to my adviser **Prof. M. -C. Amann** for giving me the opportunity to work in an excellently suited environment at the Walter Schottky Institute. Throughout this work, I got the invaluable support, perfect guidance, useful suggestions, magnificent cooperation, continuous support and effective advice from him. I am very much indebted to him for his great assistance during my thesis.

I especially thank to him whose contribution in this work was unforgettable and whose helping and friendly attitude was admirable. I am very grateful to him for making me familiarized with all the technological steps required for the VCSEL processing. He is none but my predecessor **Dr. Alexander Bachmann**.

I would like to thank to our beloved colleague **Late Kaveh-Kashani Shirazi** (who passed away from us after a tragic death, may his soul rest in perfect peace) as well as **Kristijonas Vizbaras** not only for providing me good quality samples but also for their nice and friendly behavior.

I would like to convey my heartfelt thanks to **Dr. Ralf Meyer** for his sincere cooperation, friendly behavior, useful suggestions and above all, in all administrative issues, especially for keeping everything running in the cleanroom.

Many thanks to all my colleagues at our chair **Augustinas Vizbaras, Christian Grasse, Hua Li, Michael Müller, Jia Chen, and, Tobias Gründl** for their help on many occasions. Each of them have provided invaluable support and offered their technical knowledge towards the success of the project.

I would also like to express my sincere gratitude to all members of our institute from whom I have been benefited in various ways.

Special thanks to **Andreas Hangauer** from SIEMENS for the TDLAS measurements using WMS.

Special thanks to **Konrad Klein** for the PDS measurements.

I was fortunate to be supported by **PD Dr. Rainer Michalzik**, Ulm University, with his recommendation letters about me in supporting my fellowship application to different organizations during my PhD. I would also like to thank him for his sincere comments on my publication lists.

I would like to convey my heartfelt thanks to all diploma/masters students, **Stefan Ziegler**, **Swarnakamal Priyabadina**, **Marcel Törpe** and **Stefan Sprengel** for their valuable contributions towards this project work.

I am also grateful to **Linda Mora**, **Edith Sckopke**, **Elke Thiel**, **Gabi Riedl** and **Sepp Grotenthaler** for helping me out in different cleanroom activities and also for having some funny discussions with them throughout my PhD work.

Our secretary, **Daniela Huber,** for being extremely cooperative with me in different organizational stuffs.

Many thanks go to **Jürgen Rosskopf** and **Enno Rönneberg** from Vertilas for the sincere support in the device measurement and packaging.

The collaboration partners from the Tampere University of Technology, Finland, University of Surrrey, UK, and Vertilas, Germany deserves a huge acknowledgment for their helping hands and exchange of ideas towards this project. Special thanks to **Antii Härkönen** with whom a significant amount of time of my thesis was spent to develope electrically-pumped MIR VECSELs. Thanks also to **Barnabas Ikyo** from Univ. Surrey for his valuable measurement on GaSb-based VCSELs.

Finally, I appreciate the continuous support and love of my **Mom, Dad** and **sisters** during the thesis period. This truly would not have been possible without them.

Last but by no means least, special thanks to my wife **Nadira** for her invaluable help, encouragement and presence in my life. Also thanks to my baby angel, **Ayaan** for giving me immense pleasure during my thesis writing.